INFORMATION TO USERS

This manuscript has been reproduced from the microfilm master. UMI films the text directly from the original or copy submitted. Thus, some thesis and dissertation copies are in typewriter face, while others may be from any type of computer printer.

The quality of this reproduction is dependent upon the quality of the copy submitted. Broken or indistinct print, colored or poor quality illustrations and photographs, print bleedthrough, substandard margins, and improper alignment can adversely affect reproduction.

In the unlikely event that the author did not send UMI a complete manuscript and there are missing pages, these will be noted. Also, if unauthorized copyright material had to be removed, a note will indicate the deletion.

Oversize materials (e.g., maps, drawings, charts) are reproduced by sectioning the original, beginning at the upper left-hand corner and continuing from left to right in equal sections with small overlaps. Each original is also photographed in one exposure and is included in reduced form at the back of the book.

Photographs included in the original manuscript have been reproduced xerographically in this copy. Higher quality 6" x 9" black and white photographic prints are available for any photographs or illustrations appearing in this copy for an additional charge. Contact UMI directly to order.

UMI

A Bell & Howell Information Company
300 North Zeeb Road, Ann Arbor MI 48106-1346 USA
313/761-4700 800/521-0600

PREDICTABILITY OF ENSO:

Optimal Error Growth and Forecast Skill

by

Ying-Quei Chen

A dissertation submitted in partial fulfillment
of the requirements for the degree of

Doctor of Philosophy

University of Washington

1996

Approved by _____
(Co-Chairperson of Supervisory Committee)

_____
(Co-Chairperson of Supervisory Committee)

Program Authorized
to Offer Degree Atmospheric Sciences

Date November 25, 1996

Doctoral Dissertation

In presenting this dissertation in partial fulfillment of the requirements for the Doctoral Degree at the University of Washington, I agree that the Library shall make its copies freely available for inspection. I further agree that extensive coping of this dissertation is allowable only for scholarly purposes, consistent with "fair use" as prescribed in the U.S. Copyright Law. Requests for copying or reproduction of this dissertation may be referred to University Microfilms, 1490 Eisenhower Place, P.O. Box 975, Ann Arbor, MI 48106, to whom the author has granted "the right to reproduce and sell (a) copies of the manuscript in microform and/or (b) printed copies of the manuscript made from microform."

Signature Ying-Quei Chen

Date 12/18/96

University of Washington

Abstract

Predictability of ENSO: Optimal Error Growth and Forecast Skill

by Ying-Quei Chen

Chairpersons of the Supervisory Committee: Professors E. S. Sarachik and D. S. Battisti
Department of Atmospheric Sciences

The goal of this study is to explore the short-term climate predictability of tropical Pacific sea surface temperature anomalies on the seasonal, interannual, and decadal time scales. The simple coupled atmosphere-ocean model developed by Battisti (1988) is used to evaluate the predictability of ENSO. A powerful technique called singular vector analysis is employed to obtain the structure and the maximum possible growth over a finite period of time of a perturbation applied to the coupled system at the initial time of an integration. To identify the roles of the annual cycle and the interannual ENSO cycle in determining the model predictive skill and error growth, we examine the optimal perturbation growth about several reference trajectories: with or without the annual cycle in the basic state, with or without the freely evolving model ENSO cycle, or about a perpetual climatology. The optimal perturbations evolved over periods of three, six and nine months are found. We systematically investigate the relationship between the model forecast skill and optimal error growth for 6-month integrations about the actual model forecast trajectory for the period of record 1967-90.

In most of the cases investigated, there is only one structure that grows. The optimal perturbation growth is highly dependent on the phase of both the seasonal cycle and the ENSO cycle, and it is strongly dependent on the duration over which the perturbations are evolved. The maximum perturbation growth is achieved for integrations that pass through Northern summer, and the minimum growth takes place for integrations spanning Northern winter-early spring. The optimal perturbation growth for a 6-month integration starting in the peak phase or the cold phase of the ENSO cycle is generally small. The physical processes responsible for the phase dependence of the optimal perturbation growth are identified. The initial and the final state patterns of the optimal perturbation, however, are both insensitive to the phase of the annual cycle, to the phase of the freely evolving ENSO cycle, and to the particular regions of phase space visited by the system during the period 1967-90. The structure of the optimal perturbation consists of an east-west dipole spanning the entire tropical Pacific basin, superimposed on a north-south dipole in the eastern tropical Pacific, and this structure has a simple physical interpretation.

There is a strong negative correlation between this model's forecast skill and the optimal error growth about the actual forecast trajectories, implying that the optimal error growth is in practice a useful indicator of the skill of the forecasts. Importantly, a large portion of the forecast error may be accounted for by the growth of the optimal errors in the sea surface temperature in the initial conditions alone. This suggests a need for a

higher accuracy in observations of equatorial sea surface temperature if indeed the real world is as sensitive to SST perturbations as in this model. On the other hand, in about 4% of the forecasts, the optimal error growth in SST alone is insufficient to explain the poor forecast skill, suggesting that for these extreme cases, there are possible serious flaws in the model physics. The remaining forecasts (~28%) show a weaker relation between the forecast skill and the optimal error growth.

Finally, the seasonality of the model forecast skill and the optimal error growth exhibits a phase shift of 2-3 months from the pre-1976 to the post-1976 epochs. This decadal change is largely determined by the change in the actual forecast trajectories about which the errors are allowed to develop and not by a decadal change in the average annual cycle.

TABLE OF CONTENTS

Page

LIST OF FIGURES

Figure *Page*

CHAPTER 2

CHAPTER 3

CHAPTER 4

CHAPTER 5

CHAPTER 6

APPENDIX B

LIST OF TABLES

Table *Page*

LIST OF TERMINOLOGY

ENSO . . . El Niño/Southern Oscillation

SST . . . . . sea surface temperature

SSTA . . . . sea surface temperature anomalies

B88 . . . . . the Battisti coupled atmosphere-ocean model, 1988

ZC . . . . . the Zebiak and Cane coupled atmosphere-ocean model, 1987

NINO1+2 the SST anomalies over the Niño 1+2 region [10°S to the equator and 6° offshore (to the equivalent of 87°W)], representing the equatorial coastal eastern Pacific

NINO3. . . the SST anomalies over the Niño 3 region [5°S-5°N, 90°W-150°W], representing the eastern equatorial Pacific

NINO4. . . the SST anomalies over the Niño 4 region [5°S-5°N, 150°W-160°E], representing the central equatorial Pacific

AF . . . . . Amplification Factor

FSI. . . . . model forecast skill index

SV1 . . . . . the leading singular values, i.e., λ_1 in Chapter 3 and Chapter 4.

SV2 . . . . . the second singular values

ISV1. . . . . interannual *SV1*, i.e., the leading singular values on the composite ENSO

ASV1 . . . . annual cycle *SV1*, i.e., the leading singular values on the annual cycle composite

cc . . . . . correlation coefficient

rms. . . . . root-mean-square error

re . . . . . relative rms error

ci . . . . . Contour interval

GR. . . . . the Global Residual time series

CAC . . . . Climate Analysis Center

COADS . . Comprehensive Ocean-Atmosphere Data Set

FSU . . . . . Florida State University

CLIM_I . . The climate deviation averaged from model-generated anomalies over 1967-75, representing the deviation of a cold climate state from the standard climatology.

CLIM_II . The climate deviation averaged from model-generated anomalies over 1977-87, representing the deviation of a warm climate state from the standard climatology

ECMWF . European Centre for Medium-Range Weather Forecasts

NCEP . . . National Centers for Environmental Prediction

GCM . . . . General circulation model

nowcast . . model simulation, (i.e., forecast at zero lead)

ACKNOWLEDGEMENTS

In the fall of 1990, I left my family for the first time in my life and came to Seattle for advanced study. My six years of study and research at the department of Atmospheric Sciences, University of Washington have been indeed pleasant and rewarding. For the first time in my life, I experienced the big snow storm in December 1990 and I learned to ski. I met many international friends. I read the fun Feynman books, the Chinese Kung-Fu fictions, the naive pooh-bear books and many others. I now play the piano better than before. I learned to solve puzzles and to make puzzles. I explored the informative internet resources. Of course, I enjoyed doing research and computer programming. Finally, I accomplished my dissertation, and I found my way.

The completion of my dissertation was facilitated by input from a great number of people. First of all, I would like to express my deepest gratitude toward my advisors, professor Ed Sarachik and professor David Battisti. I am thankful for Ed for providing a great atmosphere to do research and authorizing me to run the model calculations on the fastest machine in JISAO, which saved me a tremendous amount of time. I am amazed by Ed's outstanding physical intuition and his ability to grasp the essence of a new idea very quickly. Ed has a profound understanding in Buddhism, e.g., the Four Noble Truth and the Noble Eightfold Path. Once he said: "Buddha never told you to believe in anything; he wanted you to do it and see *it* yourself." "You never call Buddhism a religion; it is a *path*". I am much appreciative of David, who is enthusiastic in a broad spectrum of science and other fields. David gave me construction suggestions and comments during the course of my research, and encouraged me throughout the whole process. The incredible amount of time David spent in discussions with me and his thorough proof-reading of my manuscripts has helped me greatly.

Many thanks to professors Dennis Hartmann, Mitsuhiro Kawase, Conway Leovy, Mike Wallace, and Chidong Zhang for serving on my committee (in alphabetic order). A special thank is due to Dennis who agreed to serve as a third member on my reading committee in the last minute and helped out in the scheduling of my Final Exam. Informal discussions with some of the committee members were a great help.

This work began as a *superproblem* for the 1993 Friday Harbor summer school, organized by Professor Peter Rhines. Thanks, therefore, to Professor Rhines for facilitating the early stages of this work. Special thanks are also due to Dr. Tim Palmer, who initiated and provided many constructive comments on this work.

I am thankful for Nate Mantua who provided critical comments on this work. I am thankful for Todd Mitchell and Christian Bantzer who offered helpful advise at my practice talk and for Paul Goodman who proof-read my chapters. I appreciate the friendship from every one in JISAO. Our lovely lunch-room friend, Margaret-the-Black-Lab, makes the atmosphere in our Climate Palace very different from most official working buildings. Many thanks to everyone who had direct or indirect input in making this dissertation possible.

I would like to express my special gratitude to Ven. Jendy at the Chi-Yuan Temple in Kirkland, who helped me in many different aspects during the last two years. Sister Jendy's teaching has made me sure of the importance of learning Buddhism in my life.

I am deeply obliged to my father, Chen, Chaw-Ming, my mother Wang, Ing-Hua, and my sister, Chen, Ing-Ru, for their unconditional love and concern, and their constant encouragement and spiritual support from Taiwan and Singapore. I hope they will understand my decision for the future.

This work was supported by grants from the NOAA Office of Global Programs and the (NOAA supported) Hayes Center at the University of Washington

Dedication

I dedicate this dissertation

to my parents

Mr. Chen, Chaw-Ming, Mrs. Chen, Wang, Ying-Hua

and to master

Ven. Miao-King

孔雀雖有色嚴身　不如鴻雁能遠飛　白衣雖有富貴利　不如出家功德勝

大智度論

CHAPTER 1 INTRODUCTION

The El Niño/Southern Oscillation (ENSO) phenomenon is an interannual climate anomaly of large-scale that is rooted in the tropical Pacific. ENSO is inherently due to interactions between the atmosphere and the ocean, and it is widely thought that the crucial physics associated with ENSO is contained within the tropical Pacific basin (Battisti and Sarachik 1995). The tropical aspects of the ENSO phenomenon are summarized in numerous papers, e.g., the seminal paper of Rasmusson and Carpenter (1982), and a review paper of the observations by Trenberth (1991). Since ENSO causes profound global climate anomalies that affect millions of people and the economies of many nations, one important issue, therefore, is to understand what determines the limits of the predictive skill of the interannual variability in the tropical Pacific atmosphere-ocean system.

Zebiak and Cane (1985) presented the first coupled atmosphere-ocean model that demonstrated interannual variability similar to the observed ENSO phenomenon. The first forecast of short-term (i.e. months to years) climate anomalies was made with this model; one year in advance, the model predicted a development of positive sea surface temperature (SST) anomalies in the tropical Pacific during 1986-1987 (Cane *et al.* 1986). Since then, a variety of statistical and dynamical coupled models have been developed which possess skill (relative to a persistence forecast) in the prediction of central and eastern Pacific SST one year or more in advance (see Barnston *et al.* 1994, Latif *et al.* 1994 and Latif *et al.* 1996, for up-to-date reviews of ENSO prediction). The forecast skill of an individual model depends on the model physics and the initialization scheme, among other factors. Dynamical models that are initialized solely by forcing the ocean component of the coupled model with observed winds up until the forecast initialization time, and then diagnostically determining the model atmosphere generally have nowcast (i.e., zero-lead time) correlation skills of above ~0.7 for the Niño3 index[1] and maintain useful correlation skills out to at least one year (e.g., Cane et al. 1986). More sophisticated ini-

tialization procedures significantly increases the time span over which the model can make skillful forecasts (D. Chen *et al.* 1995; Rosati *et al.* 1995). Statistical models have also demonstrated useful forecast skill out to about twelve months (e.g., Penland and Sardeshmukh 1995, and Graham *et al.* 1987).

ENSO forecasts are presently being used in many tropical countries with great social and economic benefits (see, e.g., Moura 1994 and the review by Battisti and Sarachik 1995). In order to make rational decisions based on an ENSO forecast, it is important to understand the intrinsic limitations to the forecast accuracy, to identify the sources of possible forecast error, and to identify times when the system is extraordinarily sensitive to errors in the state of the system (the initial conditions) from which the forecast is made. Important and practical questions arise concerning the nature of the observing system that is required to achieve the most skillful forecasts. The questions include:

- Which variables must be monitored?
- What spatial and temporal resolution is required for each variable in order to optimize the forecast skill?
- Is the predictability of the tropical atmosphere-ocean system inherently seasonally dependent?
- Does the forecast skill of a given model depend on the season from which the forecast is made from?
- How do we discriminate forecast errors that are due to model imperfections from those that are due to initialization errors?

An important step in understanding the predictability of the tropical Pacific atmosphere-ocean system is to study error growth in a linearized version of an actual prediction

---

1. The Niño 3 index refers to the SST anomaly averaged from 5°S to 5°N and 150°W to 90°W.

model. A traditional starting point is the identification of the most unstable eigenmode of the physical system. This, however, is not the appropriate approach for understanding the predictability of this dynamical system because the linear approximation of the tropical atmosphere-ocean system is a non-normal dynamical system in which the linear transient growth can be much greater than the growth of the gravest eigen-mode for a time scale of interest, e.g., six–months or 1-2 years. A sufficient condition to ensure non-normality is the asymmetric way in which the atmosphere and ocean are coupled (see chapter 2). A non-normal system is also ensured by the annual cycle of the spatially inhomogeneous mean states of both the ocean and the atmosphere. Hence in order to describe more completely the linear error growth of this system, we need to find a suitable orthogonal basis which describes the finite time linear growth of perturbations to the initial conditions of the system. This basis is provided by the *singular vectors* of the integral propagator associated with the linearized model (Lorenz 1965, Buizza and Palmer, 1995). The propagator is the linear operator which takes perturbations at a given time and *propagates* them to some time into the future; it has also been referred to as *the resolvent*[1] or *Green function* (e.g. Penland and Sardeshmukh, 1995). The fastest growing singular vector has also been called an *optimal perturbation* (e.g. Farrell 1989). The most unstable eigenmode that is ubiquitous to numerous tropical Pacific atmosphere-ocean models is a quasi-stationary eigenmode, which is similar in structure to the observed ENSO and has an e-folding time of about one year. In this study we will examine the growth of the optimal initial perturbations, which will be seen to be much greater than that associated with the gravest eigenmode of the system.

1. More on the theory of the non-self-adjoint systems and their predictability can be found in Farrell (1990).

Analysis of the optimal perturbation growth can be used to identify the cause for errors in a forecast, and thus to help answer the five questions noted above (Buizza *et al.* 1995). In this study, we focus on the growth of perturbations that are prescribed at the initial time of the model integrations. We also use this model to perform retrospective ENSO forecasts and use the singular vector analysis to determine whether the forecast errors can be attributed to errors in the initial conditions, or must they be due to errors in the model physics. Because the low-frequency (e.g., seasonal to interannual) atmospheric circulation anomalies of global proportions are strongly related to tropical Pacific SST anomalies, we choose to focus our efforts on evaluating the sensitivity of the final state SST field to small perturbations in the initial state of the SST in the model.

The outline of this dissertation is as follows. Chapter 2 describes the model used in this study, which is the Battisti's (1988) version of the Zebiak and Cane (1987) coupled atmosphere-ocean model. Both the atmosphere and the ocean components of the coupled model are tested in their respective hindcast simulations. Chapter 3 introduces the method of singular vector analysis and briefly reviews the theory of the linear optimal perturbation growth. We illustrates using a simple example that the linear optimal perturbation can be much greater than the exponential growth of the eigenmode of the system within a finite growth time. Chapter 4 reports the optimal growth of the perturbations and their spatial patterns along several idealized reference trajectories: e.g., the annual cycle climatological trajectory, the annual mean climatological trajectory, the freely evolving model ENSO with or without the annual cycle in the background basic state. The dependence of the growth of the optimal perturbation on the seasonal cycle and the ENSO cycle is discussed. Physical interpretation for the structure of the optimal perturbation is also provided. We use the model in a forecast mode in Chapter 5 and explore the relationship between the ENSO forecast skill and the optimal error growth during the period 1967-1990. We

present the relationship between the forecast skill and the optimal error growth as a function of the seasonal cycle and the ENSO cycle. The optimal error growth is demonstrated to be a crucial factor in determining the model predictability; about two-thirds of the forecast error at a six-month lead time can be accounted for by the optimal error growth in SST anomalies. Several studies have pointed out the shift in the climate of tropical Pacific climate that occurred in 1976-1977. This shift represents a transition from a decade or more of anomalously cold conditions to anomalously warm conditions in the tropical Pacific that lasted from 1977 to the late 1980's. Concomitant with the SST anomalies are changes in the trade winds, the centers of convection, and anomalies in the mid-latitude North Pacific atmosphere and ocean. In Chapter 6, we analyze the time series of the optimal error growth and the forecast skill obtained from Chapter 5 and investigate the decadal change in their seasonality for the two periods 1967-75 and 1977-87. Hypotheses for the differences in the mean and the annual cycle of the optimal error growth and the forecast skill for these two periods are posed and tested. Finally, we present some concluding remarks in Chapter 7.

CHAPTER 2 THE MODEL

2.1 The Coupled Atmosphere-Ocean Model: An Overview

The coupled atmosphere-ocean model used in this study is described in Battisti (1988, hereafter B88), which follows very closely the coupled model of Zebiak and Cane (1987, hereafter ZC)[1]. This coupled model consists of an ocean whose evolution is treated prognostically, coupled to an atmosphere whose state is determined diagnostically at each time step (Δt = 10 days; Zebiak 1986). Both the ocean and the atmosphere are anomaly models constructed about a annually varying background state (Fig. 2.1). The ocean is forced by the anomalous surface wind stress and the atmosphere is forced by a parameterized anomalous latent heat release. The latent heat release is a function of the climatological convergence of the wind field and the total SST. Both of these forcing terms are nonlinear. The ocean model domain is a rectangular basin spanning 30°S to 30°N and 124°E to 80°W. The horizontal resolution of the ocean model is 0.5° latitude and 2° longitude (2° latitude and 6° longitude) for the ocean dynamics (thermodynamics). The atmosphere and ocean dynamics are modeled on an equatorial β-plane. A more detailed description of this model follows.

2.1.1 Ocean model

The ocean model consists of an upper layer overlying a deep motionless layer. The upper layer contains within it a fixed depth surface mixed layer (H_s = 50 meters) used for thermodynamic calculations.

The anomalous upper layer depth (h) and currents (u, v) are governed by linear shallow-water wave dynamics:

---

1. The known differences between the ZC and B88 models are subtle and are documented in Mantua and Battisti, 1994.

$$\frac{\partial u}{\partial t} - \beta y v = -g' \frac{\partial h}{\partial x} + \frac{\tau^x}{\rho_0 H_0} - \gamma u \qquad \text{(EQ 2.1)}$$

$$\beta y u = -g' \frac{\partial h}{\partial y} + \frac{\tau^y}{\rho_0 H_0} - \gamma v \qquad \text{(EQ 2.2)}$$

$$\frac{\partial h}{\partial t} + H_0 \nabla \cdot \vec{u} = -\gamma h \qquad \text{(EQ 2.3)}$$

where γ is a Rayleigh damping coefficient (γ^{-1} = 2.5 years), g' (= 0.056 m s^{-2}) is the reduced gravity, ρ_0 (= 1026 kg m^{-3}) is the water density, and H_0 (= 150 meters) is the mean upper layer depth. The pressure perturbation is calculated hydrostatically. We also assume that all of the surface wind stress (τ_x, τ_y) is deposited uniformly in the first layer as a body force. The surface wind stress is calculated using the standard bulk formula parameterization:

$$\vec{\tau} = \rho_a C_D |\vec{u}_a| \vec{u}_a \qquad \text{(EQ 2.4)}$$

where ρ_a is the air density, C_D is the drag coefficient and $\vec{u}_a$ is the atmospheric surface wind.

An accurate simulation of SST requires the correct surface flow, entrainment and thermal structure within a layer near the surface. We have assumed that both layers in the ocean are homogeneous and that the surface wind stress is a body force acting on the upper layer. Surface wind stress, however, is actually deposited only within the surface mixed layer (Schopf and Cane 1983). Thus, following ZC (1987), we introduce a frictional component of the flow (u_s, v_s) in a homogeneous mixed layer in which the surface wind stress is balanced by a surface Rayleigh damping and rotation.

$$\gamma_s \vec{u}_s + \beta y \hat{k} \times \vec{u}_s = -\frac{1}{\rho_0} \nabla P_1 + \frac{\vec{\tau}}{\rho_0 H_s} - \gamma \vec{u}_s \qquad \text{(EQ 2.5)}$$

where γ_s is the mixed layer damping time (γ_s^{-1} = 2 days).

The surface currents (u_{sfc}, v_{sfc}) are then modified by redistributing the momentum transport in the upper layer so that the wind-driven frictional transport is confined to the mixed layer:

$$\hat{u}_{sfc}H_s = \left(\hat{u}H_s - \hat{u}_s H_s \cdot \frac{H_s}{H_0}\right) + \hat{u}_s H_s \qquad \text{(EQ 2.6)}$$

$$\hat{u}_{sfc} = \hat{u} + \hat{u}_s\left(1 - \frac{H_s}{H_0}\right). \qquad \text{(EQ 2.7)}$$

Eqs. 2.6-2.7 yield a more reasonable estimation of the surface currents. The upwelling (or entrainment rate) is calculated as the divergence of surface currents:

$$w = H_s \cdot \left(\frac{\partial u_{sfc}}{\partial x} + \frac{\partial v_{sfc}}{\partial y}\right). \qquad \text{(EQ 2.8)}$$

The model thermodynamics are only active in the surface mixed layer. SST is calculated separately and does not directly affect the ocean dynamics. The nonlinear equation for the sea surface temperature anomalies (hereafter SSTA) is (see ZC, 1987):

$$\frac{\partial T}{\partial t} = \underbrace{-\left[\overbrace{u_{sfc}\cdot\frac{\partial}{\partial x}(\bar{T}+T)}^{(v)} + \overbrace{v_{sfc}\cdot\frac{\partial}{\partial y}(\bar{T}+T)}^{(vi)}\right] - \left[\overbrace{\bar{u}_{sfc}\cdot\frac{\partial T}{\partial x}}^{(vii)} + \overbrace{\bar{v}_{sfc}\cdot\frac{\partial T}{\partial y}}^{(viii)}\right]}_{(i)}$$

$$\underbrace{-[\Delta(\bar{w}+w) - \Delta(\bar{w})]\cdot\frac{T+T_{sub}}{H_s}}_{(ii)} \quad \underbrace{-\Delta(\bar{w}+w)\cdot\frac{T+T_{sub}}{H_s}}_{(iii)} \quad \underbrace{-\alpha_s T}_{(iv)} \qquad \text{(EQ 2.9)}$$

where the variables with an overbar represent the annual cycle of the specified monthly mean climatological values; the ones without represent the anomalies. The variables in Eq. 2.9 are:

T the SST (equivalently, the temperature in the surface mixed layer),

u_{sfc}, v_{sfc} the eastward and northward surface currents in the surface mixed layer,

w the entrainment rate, or upwelling at the base of the surface mixed layer,

$\Delta(x)$ the Heavyside function defined as: $\Delta(x) = \begin{cases} x, & (x > 0) \\ 0, & (x \le 0) \end{cases}$,

T_{sub} the subsurface temperature at the base of the mixed layer (50 m depth), and

α_s the thermal damping coefficient.

Eq. 2.9 states that local changes in SSTA are determined by the temperature advection (term *i*), which is due to the advection of the total temperature by the anomalous horizontal flow (terms *v-vi*), advection of temperature anomalies by the mean horizontal flow (terms *vii-viii*), anomalous entrainment in the presence of a mean temperature discontinuity at the base of the surface mixed layer (term *ii*), total entrainment in the presence of an anomalous temperature difference at the base of the mixed layer (term *iii*), and Newtonian damping (term *iv*, α_s^{-1} = 125 days), which is a simple parameterization of net surface heat flux anomalies. A Heavyside function $\Delta(x)$ appears in the entrainment term because an upwelling ($w > 0$) cools SST by bringing up colder subsurface water, while a downward motion ($w < 0$) does not affect SST.

The mean state of the ocean surface-layer temperature (i.e. SST) about which the anomaly model is constructed is that given by Rasmusson and Carpenter (1982; hereafter RC). The mean surface-layer currents are calculated by forcing the model with the RC annual cycle winds until a cyclic steady state is reached. The subsurface temperature anomalies (T_{sub}) are parameterized in terms of thermocline displacements (see Appendix A and B88):

$$T_{sub} = \Theta(h) \cdot [\tanh(\lambda(\bar{h} + 1.5|h|)) - \tanh(\lambda h)] . \qquad \text{(EQ 2.10)}$$

2.1.2 Atmosphere model

The atmosphere model is the linear two-layer Gill (1980) model of a thermally forced tropical atmosphere. The forcing of the atmosphere depends on the total atmospheric convergence and the SST and is calculated iteratively (Zebiak 1986) -- the so-called *convergence feedback* effect. The atmosphere is treated diagnostically and only changes on time-scales associated with the SST changes. The equations that comprise the coupled model are found in Appendix A of Battisti (1988).

2.2 Model Performance

2.2.1 Uncoupled ocean model hindcast

One-way forcing experiments using the atmosphere and ocean models separately indicate that each component of the coupled model produces a reasonable simulation of the observed interannual variability in the region of the oceanic equatorial waveguide. When forced by observed (FSU) wind stress anomalies, the ocean model has been shown to provide a qualitatively good simulation of the observed SST. Fig. 2.2 plots the correlation and rms error of the time series of the observed (data from Climate Analysis Center) and the model hindcast SSTA in three Niño regions from 1961-1993 (see also Mantua and Battisti 1994). Following Rasmusson and Carpenter (1982), we adopt three traditional indices: Niño 1+2 [10°S to the equator and 6° offshore (to the equivalent of 87°W)], Niño 3 [5°S-5°N, 90°W-150°W] and Niño 4 [5°S-5°N, 150°W-160°E], which represent the equatorial coastal eastern Pacific, the eastern equatorial Pacific and the central equatorial Pacific, respectively. For example, the correlation coefficient of the observed and the model hindcast SSTA in the Niño 3 region for the period of 1970-1985 is ~0.7; it is 0.6 for the period of 1967-90. The model hindcast reveals a warm bias in the central and eastern equatorial Pacific.

2.2.2 Uncoupled atmosphere model hindcast

When the atmospheric model is forced by either the RC composite ENSO SST anomalies or the 1982-83 Pacific SST anomalies, the surface wind anomalies near the equator are similar to the observed anomalies (Zebiak 1986). There are, however, significant differences between the simulated and observed anomalies in the wind field away from the equator at all longitudes (for example, compare Gill 1980 with Gill and Rasmusson 1984). We force the atmospheric model with the observed COADS SSTA and examine the model generated wind stress anomalies. Fig. 2.3 shows (a) the forcing field SSTA, (b) the Gill model response, and (c) the observed FSU wind stress anomalies, for a composite warm phase. Comparing Fig. 2.3 (b) with (c) and with Fig. 2.3 (d), the regression map of SST and surface wind, it is clear that the Gill model simulates well the large-scale, low-frequency patterns along the equator. However, it also illustrates that the simple Gill model generated equatorial westerly anomalies that are somewhat more to the east, and the easterly anomalies off the equator are deviant from the observational data.

2.2.3 Coupled model

When the atmosphere and ocean models are coupled, the model supports interannual variability that has much in common with observed ENSO events (Fig. 2.4 a). Specifically, the spatial structure of the model ENSO is of basin-scale, with the greatest SST anomalies in the eastern and central Pacific (Fig. 2.4b); the model events are locked to the annual cycle, with simulated and observed warm events generally peaking in December-January; the variance in SST is predominantly at the interannual time-scale, with the model supporting substantially less variability than in the observations at subannual time-scales (Mantua and Battisti 1995). The simulated ENSO events recur every three or four years - much more regularly than the observed ENSO events. The physics of the interannual variability displayed by this coupled atmosphere-ocean model is described by the *delayed oscillator* mechanism (Battisti and Hirst 1989).

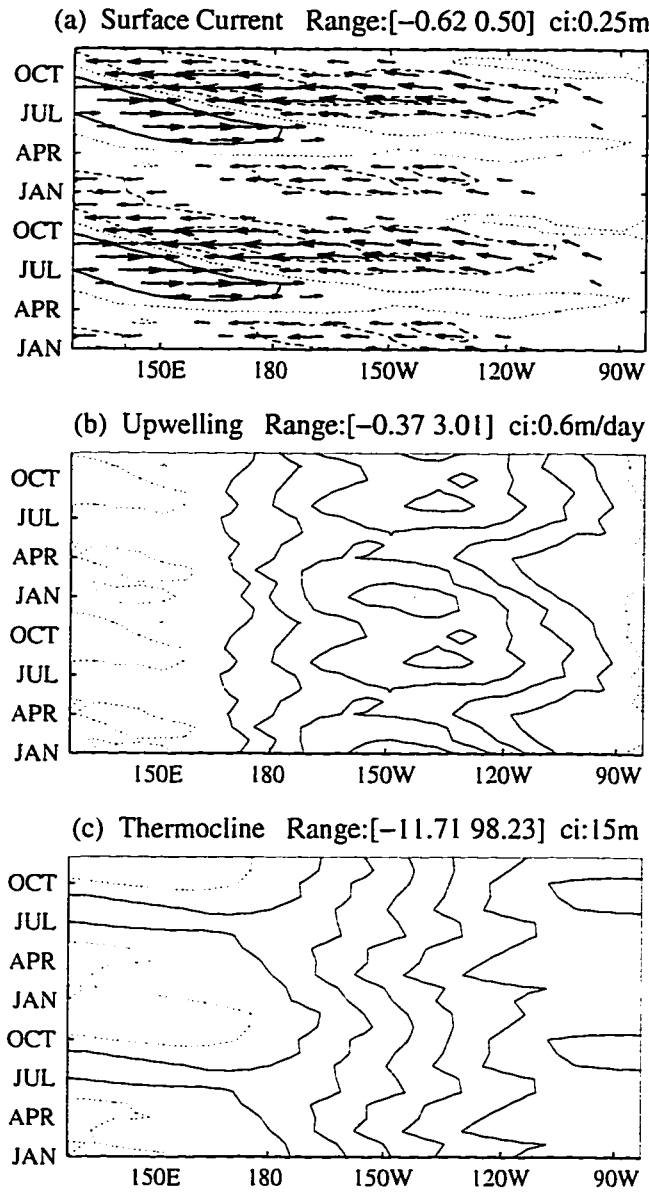

Figure 2.1 Time-longitude contours of the model generated annual cycle of various mean fields averaged over 2° latitude about the equator: (a) surface zonal currents ($\bar{u}_{sfc}$, contour interval (hereafter c.i.) = 0.2 m s^{-1}), (b) upwelling ($\bar{w}$, c.i.= 0.5 m day^{-1}) and (c) the thermocline displacements ($\bar{h}_T$, c.i. = 10 m) about the resting depth of 150m. Positive contours in thermocline plot denote upward displacements. The minimum and maximum values of the field plotted are written at the top. The shading is in the sense of warming: positive contours in $\bar{u}_{sfc}$, and negative contours of $\bar{w}$ and $\bar{h}_T$ are shaded.

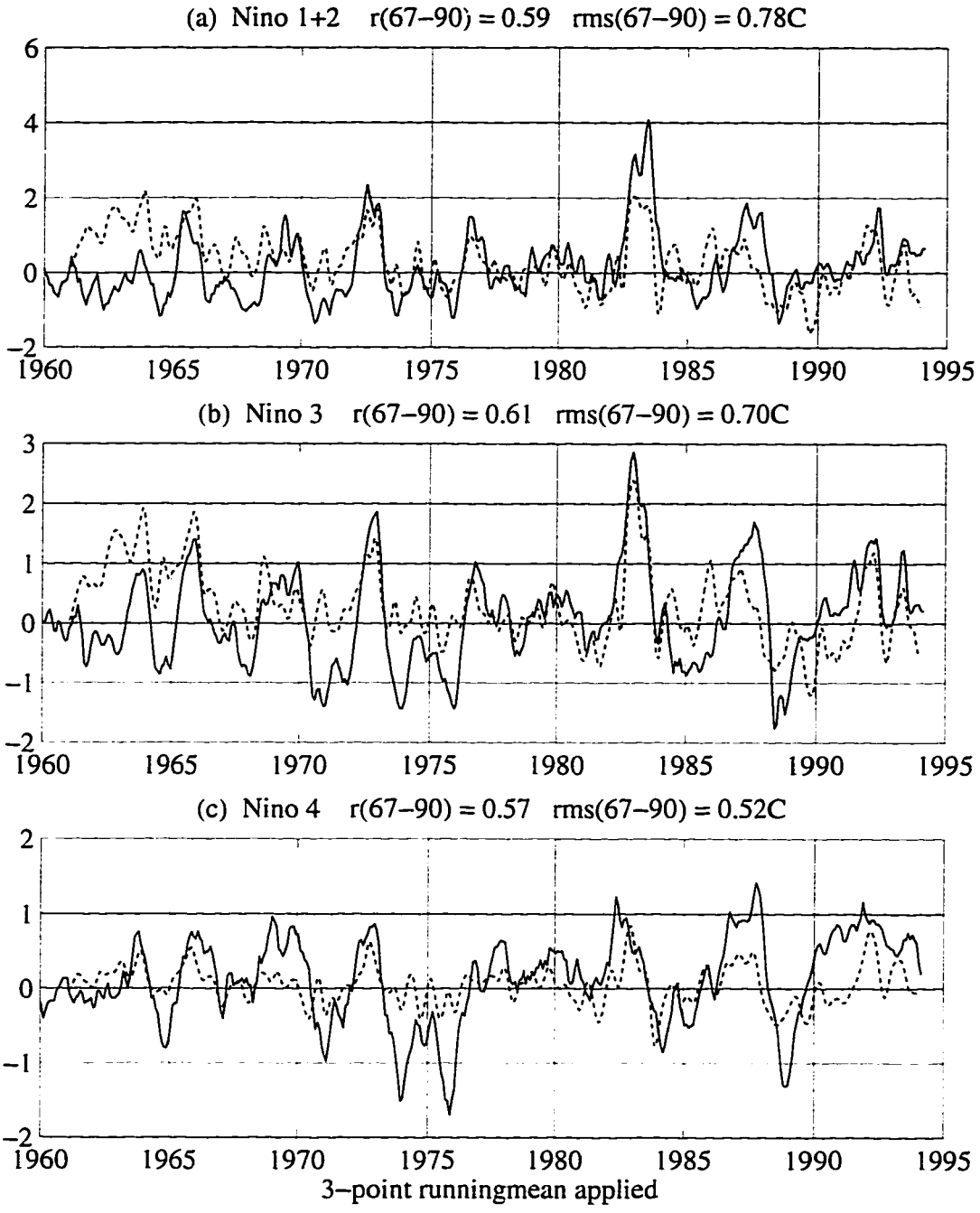

Figure 2.2 The observed (data from CAC, solid line) and the ocean model (dashed line) simulated Niño indices for the period January 1961 - December 1990: the SST anomalies in the (a) Niño 1+2, (b) Niño 3 and (c) Niño 4 regions. The ocean model is forced by the observed wind stress (data from FSU). A three-point running-mean is applied to all curves. The correlation coefficient and the rms error between the observed and the model simulated time series over the 1967-1990 period are noted on the top of each panel.

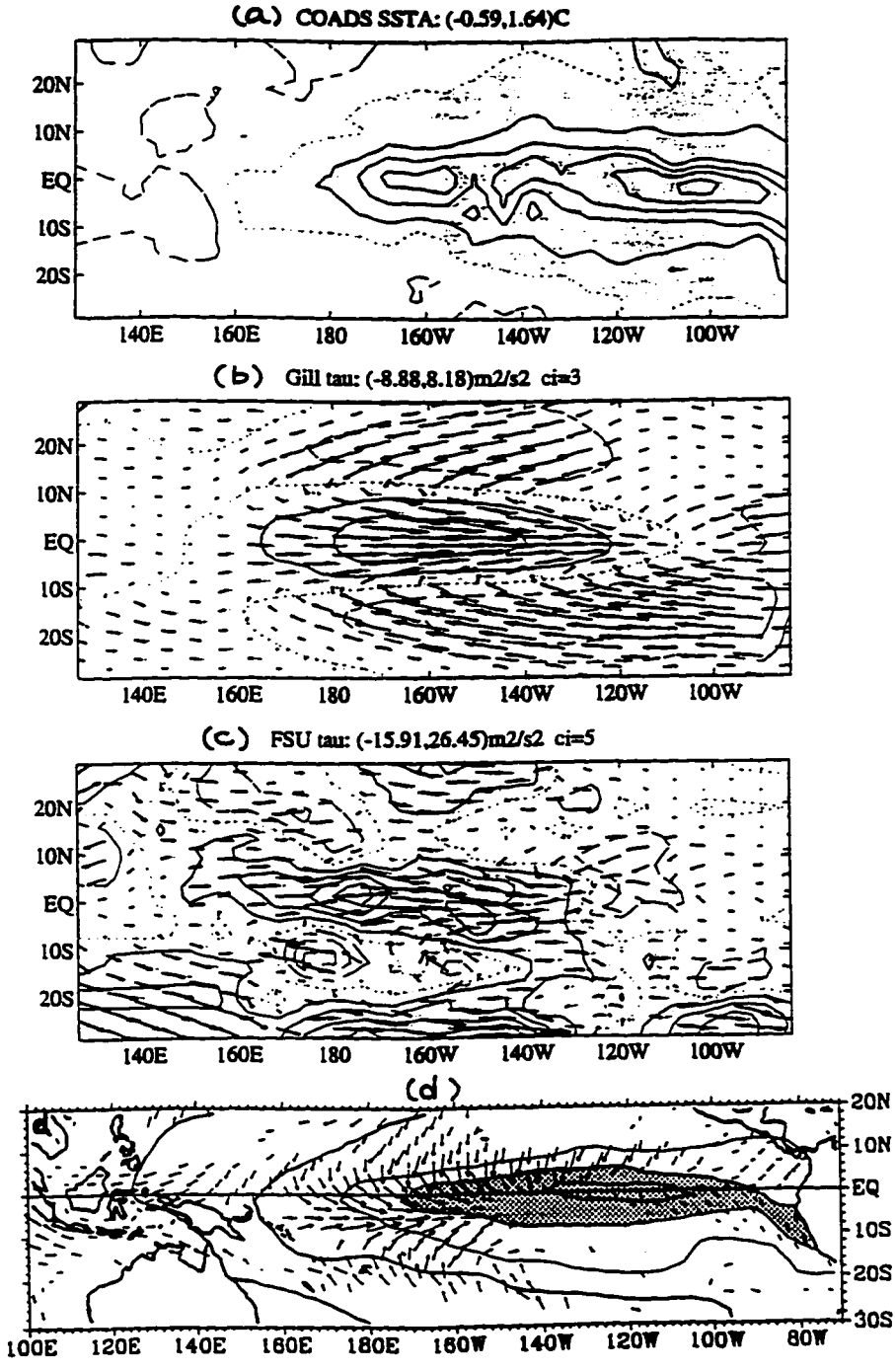

Figure 2.3 Simulation experiment for the composite warm phase: (a) the forcing field SSTA, (b) the Gill model generated wind stress anomalies. The observed FSU wind stress anomalies are shown in panel (c). Panel (d) is the regression map of SST and surface wind for the period December-February (Deser and Wallace 1990).

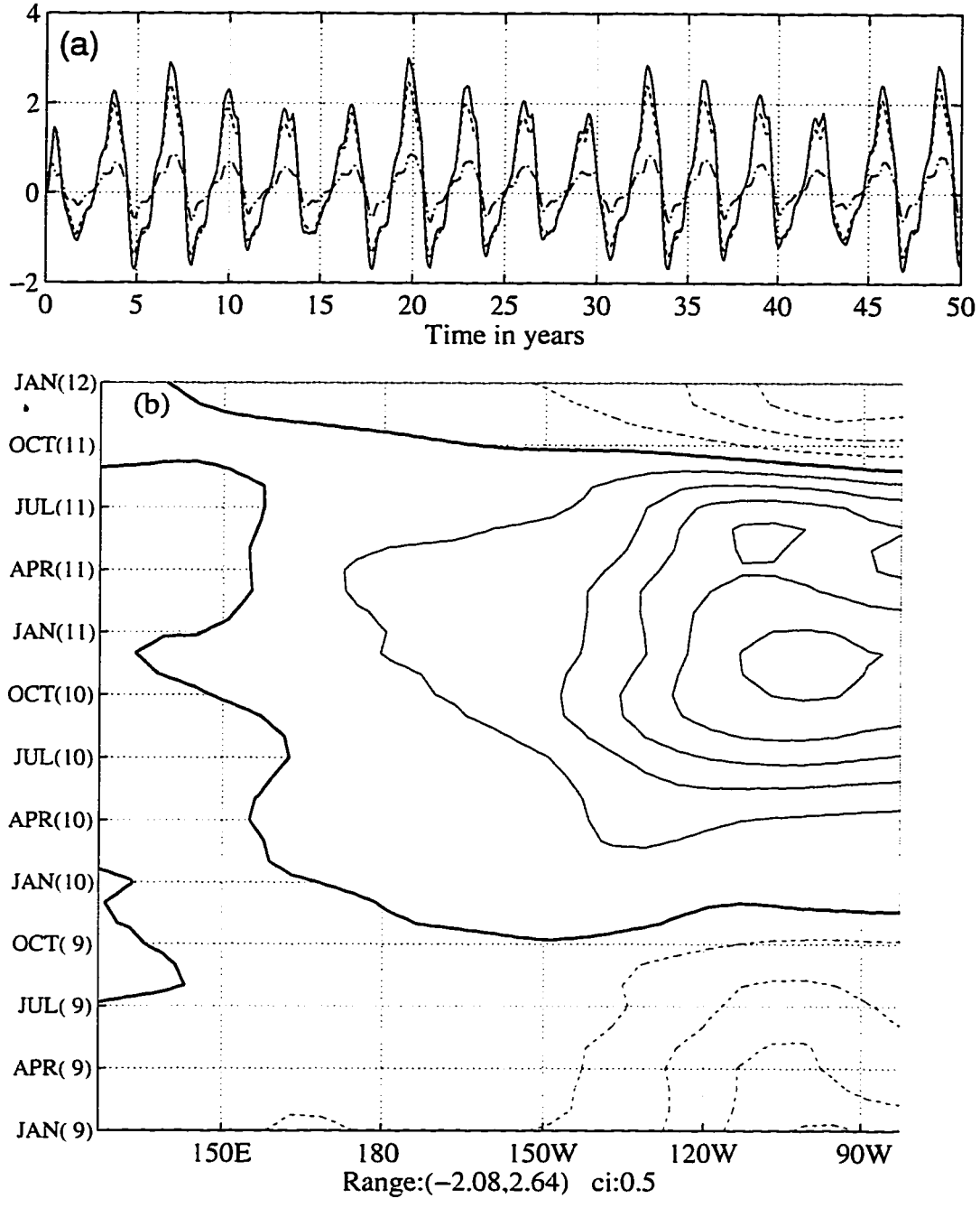

Figure 2.4 (a) 20-year time series of the Niño indices from the control integration of the Battisti coupled atmosphere-ocean model: Niño 1+2 (solid) Niño 3 (dashed) and Niño 4 (dash-dot). (b) Time-longitude section of SST from the (arbitrarily chosen) fourth model ENSO cycle (SST is averaged from 2°S to 2°N; contour interval is 0.5°C). Positive (negative) contours are in solid (dashed) lines. Zero contours are in heavy lines.

CHAPTER 3 SINGULAR VECTOR ANALYSIS

3.1 Theory of the Singular Vector Analysis — The Maximum Possible Amplification of Initial Perturbations

Suppose the perturbation state vector $\vec{X}$ (in our study, $\vec{X}$ may include surface currents, thermocline displacements, SST perturbations and surface winds) satisfies a linear prognostic equation, we can write the following matrix equation

$$\frac{\partial \vec{X}}{\partial t} = L\vec{X} \qquad \text{(EQ 3.1)}$$

for the time tendency of the state vector.

If L is a non-normal operator (i.e., $L^*L \neq LL^*$, where the superscript '*' indicates the complex-conjugate transpose), the eigenvalues of L do not bound the maximum transient growth of perturbations, as they would for a normal operator. The solution to Eq. 3.1 for the perturbation state vector $\vec{X}$ at time $t+\tau$ is given by:

$$\vec{X}(t+\tau) = R(t,\tau)\vec{X}(t) . \qquad \text{(EQ 3.2)}$$

Here R is the propagator (see Fig. 3.1),

$$R(t,\tau) = \exp\left(\int_t^{t+\tau} L dt\right). \qquad \text{(EQ 3.3)}$$

If the basic state trajectory is time-independent,

$$R(t,\tau) = \exp(L\tau) . \qquad \text{(EQ 3.4)}$$

We choose as our measure of the perturbation vector the norm based on the standard inner product applied to the state vector, $\left\|\vec{X}\right\|^2 \equiv \langle \vec{X}(t), \vec{X}(t) \rangle = \vec{X}^* W \vec{X}$, where W

is a diagonal weighting matrix. In principle, W can be any positive definite matrix, and can be used to implement norms based on perturbation energy or other physically based quantities.

The *Amplification Factor* of a perturbation vector over time τ is therefore the ratio of the norm of the state vector at the final time to that at the initial time:

$$AF = \frac{\left\|\vec{X}(t+\tau)\right\|}{\left\|\vec{X}(t)\right\|} = \frac{\langle \vec{X}(t+\tau), \vec{X}(t+\tau)\rangle^{1/2}}{\langle \vec{X}(t), \vec{X}(t)\rangle^{1/2}} \quad . \qquad \text{(EQ 3.5)}$$

$$= \frac{\langle \boldsymbol{R}\vec{X}(t), \boldsymbol{R}\vec{X}(t)\rangle^{1/2}}{\langle \vec{X}(t), \vec{X}(t)\rangle^{1/2}} = \frac{\langle \vec{X}(t), \boldsymbol{R}^*\boldsymbol{R}\vec{X}(t)\rangle^{1/2}}{\langle \vec{X}(t), \vec{X}(t)\rangle^{1/2}}$$

Because the operator $\boldsymbol{R}^*\boldsymbol{R}$ is symmetric (even though $\boldsymbol{R}$ is not normal), the eigenvalues are positive real numbers, and the set of eigenvectors of $\boldsymbol{R}^*\boldsymbol{R}$ form an orthonormal basis which can be used to describe any arbitrary perturbations to the model state vector.

$\boldsymbol{R}$ can be factored using singular value decomposition (e.g., Strang 1988):

$$\boldsymbol{R} = \boldsymbol{F}\Lambda\boldsymbol{E}^*, \qquad \text{(EQ 3.6)}$$

where Λ is a real, positive, diagonal matrix, and $\boldsymbol{E}$, $\boldsymbol{F}$ are orthonormal (unitary) matrices. The diagonal entries of Λ are referred to as singular values, and the respective columns of $\boldsymbol{E}$ and $\boldsymbol{F}$ are referred to as right and left singular vectors, respectively. From Eq. 3.6, we see that the singular values of $\boldsymbol{R}$ are the square roots of the eigenvalues of $\boldsymbol{R}^*\boldsymbol{R}$:

$$\boldsymbol{R}^*\boldsymbol{R} = \boldsymbol{E}\Lambda^2\boldsymbol{E}^*. \qquad \text{(EQ 3.7)}$$

and, from Eq. 3.5, the maximum value of AF is given by:

$$AF \leq \frac{\langle \vec{E_1}(t), \lambda_1^2\vec{E_1}(t)\rangle^{1/2}}{\langle \vec{E_1}(t), \vec{E_1}(t)\rangle^{1/2}} = \lambda_1. \qquad \text{(EQ 3.8)}$$

Hence, the largest singular value of $\boldsymbol{R}$, λ_1, bounds the growth of a perturbation to the system. The corresponding right singular vector, $\vec{E}_1$, is the pattern of the initial perturbation that leads to the greatest perturbation growth. When we refer to *singular vector* without qualification we will mean the right singular vector, or equivalently, the initial pattern of the optimal perturbation. Examination of Eq. 3.6 shows that $\boldsymbol{R}(t,\tau)\vec{E}_1 = \lambda_1\vec{F}_1$. Hence, $\lambda_1\vec{F}_1$, derived by applying the propagator to the initial pattern, is the corresponding final pattern of amplitude λ_1. The above discussion also holds when $\boldsymbol{R}$ is restricted to act on a subset of the complete state vector.

As stated above, if we interpret the initial perturbation as the error or uncertainty at the initial time, *the maximum possible error growth over time τ is the first (largest) singular value of the propagator, $\boldsymbol{R}$. The initial and final patterns that accomplish this error growth are the right and left singular vectors of $\boldsymbol{R}$.*

3.2 An Example Illustrating that the Linear Transient Growth Can Be Greater than the Modal Growth For A Finite Time

We now take one example illustrating that during a finite amount of time, the linear growth may be much greater than the normal mode exponential growth. Consider Eq. 3.1 where $\boldsymbol{L}$ is the simple time-independent, 2 by 2 matrix $\boldsymbol{L}$:

$$\boldsymbol{L} = \begin{bmatrix} 1 & 10 \\ 0 & 2 \end{bmatrix}. \qquad \text{(EQ 3.9)}$$

Solving the standard eigenvalue problem, we obtain $\Lambda = \begin{bmatrix} \sigma_1 & 0 \\ 0 & \sigma_2 \end{bmatrix} = \begin{bmatrix} 2 & 0 \\ 0 & 1 \end{bmatrix}$ as the eigenvalues, and $V = \begin{bmatrix} \vec{v}_1 & \vec{v}_2 \end{bmatrix} = \begin{bmatrix} 0.9950 & 1 \\ 0.0995 & 0 \end{bmatrix}$ as the corresponding eigenvectors of L, such that they satisfy the following relation:

$$L = V\Lambda V^{-1}. \qquad \text{(EQ 3.10)}$$

Since the matrix L has two distinct eigenvalues, any vector can then be described in terms of a linear combination of $\vec{v}_1$ and $\vec{v}_2$ (see Fig. 3.2).

The linear propagator R, from Eq. 3.4, is thus:

$$R(\tau) = \exp(L\tau) = \exp\left(V\Lambda V^{-1}\tau\right) = V\exp(\Lambda\tau)V^{-1} \qquad \text{(EQ 3.11)}$$

$$= \begin{bmatrix} e^{\tau} & 10\cdot\left(e^{2\tau} - e^{\tau}\right) \\ 0 & e^{2\tau} \end{bmatrix}.$$

The two eigenvectors of L are the normal modes of the system. The exponential growth, $\left\|R\vec{v}_1\right\|$ (the solid line) and $\left\|R\vec{v}_2\right\|$ (the dashed line), are plotted in Fig. 3.3a as a function of integration time, τ.

Next, we start with an arbitrary unit vector: $\vec{q} = \begin{bmatrix} \frac{1}{\sqrt{2}} \\ \frac{1}{\sqrt{2}} \end{bmatrix}$ and watch its evolution governed by Eq. 3.1 and Eq. 3.9. The linear propagator brings this unit vector $\vec{q}$ to $R\vec{q}$

over time τ with an amplification factor of $\frac{\|\boldsymbol{R}\vec{q}\|}{\|\vec{q}\|}$. Fig. 3.3b plots this amplification factor as a function of τ. Note that the vector $\vec{q}$ achieves larger amplitudes (the dotted line) than does the dominant normal mode (the solid line). This arbitrarily chosen example shows the case that, in general, the normal mode is not the fastest growing vector over some finite time.

Finally, we apply singular value decomposition on matrix $\boldsymbol{R}$ (Eq. 3.4 and Eq. 3.9), in the form of Eq. 3.6. The left field $\boldsymbol{F}$, the singular values Λ, and the right field $\boldsymbol{E}$ are as follows:

$$\boldsymbol{F} = \begin{bmatrix} 0.9878 & -0.1558 \\ 0.1558 & 0.9878 \end{bmatrix}; \quad \Lambda = \begin{bmatrix} 47.3648 & 0 \\ 0 & 0.4241 \end{bmatrix}; \quad \boldsymbol{E} = \begin{bmatrix} 0.0567 & -0.9984 \\ 0.9984 & 0.0567 \end{bmatrix}.$$

We take the first singular vector as an example:

$$\vec{E}_1 = \begin{bmatrix} 0.0567 \\ 0.9984 \end{bmatrix}. \qquad \text{(EQ 3.12)}$$

Fig. 3.3b shows that $\vec{E}_1$ (the dash-dot line) grows much faster than does the dominant normal mode $\vec{v}_1$ (the solid line). Fig. 3.3c plots the growth rate for the two eigenvectors, $\vec{v}_1$ (the solid line with a constant value of 2, i.e., its corresponding eigenvalue) and $\vec{v}_2$ (the dashed line with a constant value of 1, i.e., its corresponding eigenvalue), and the growth rate of the first singular vector, $\vec{E}_1$. Here, the growth is defined as:

$$\frac{1}{\|\vec{X}\|} \cdot \left\| \frac{d\vec{X}}{dt} \right\| = \frac{1}{\|\vec{X}\|} \cdot \|L\vec{X}\|. \qquad \text{(EQ 3.13)}$$

The growth rate of the first singular vector approaches the growth rate of the dominant eigenvector as time approaches infinity. As illustrated in Eq. 3.8, the growth of the first singular vector bounds the maximum linear transient growth, and the growth rate is the largest singular value.

For a normal system, in which the eigenvectors are orthonormal to each other, the projection of any unit vector in the space onto any eigenvector is always less than 1. Hence, the gravest normal mode growth dominates the growth of any other vectors for any integration time considered. However, the climate system is generally *not* normal. Eq. 3.9 gives an example in which the angle between its two eigenvectors is very small (see e.g., Fig. 3.2). Expressing the first singular vector $\vec{E}_1$ of $\boldsymbol{R}$ in terms of the two eigenvectors of $\boldsymbol{L}$ as

$$\vec{r}_1 = \begin{bmatrix} \vec{v}_1 & \vec{v}_2 \end{bmatrix} \begin{bmatrix} c_1 \\ c_2 \end{bmatrix}. \qquad \text{(EQ 3.14)}$$

yields the linear coefficients:

$$\begin{bmatrix} c_1 \\ c_2 \end{bmatrix} = \begin{bmatrix} 10.0337 \\ -9.9272 \end{bmatrix}. \qquad \text{(EQ 3.15)}$$

The projection coefficients of $\vec{E}_1$ onto the eigenvectors of $\boldsymbol{L}$ are greater than 1. Thus, the transient growth can dominate over the modal growth.

The non-orthonormality of the eigenvectors of the system is the key to the fact that the linear transient growth can be much greater than the exponential normal mode growth in a non-normal system. The coupled atmosphere-ocean is an example of a system in which the eigenvectors are not orthonormal to each other. The relevance of the transient growth to ENSO will be discussed in the following chapters. We will also examine the

relation between the fastest growing perturbation and the model forecast skill, and their dependence on the annual cycle and the ENSO cycle.

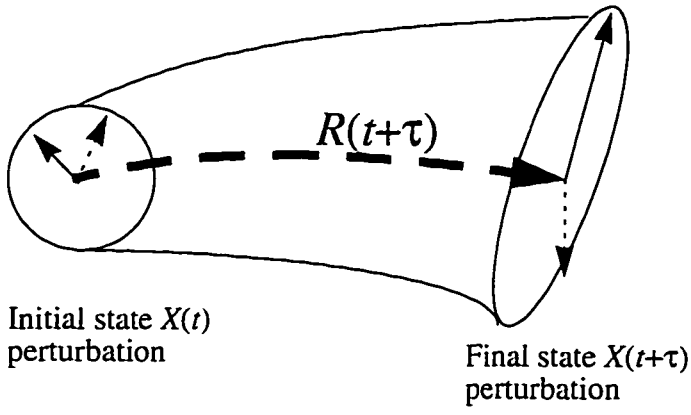

Figure 3.1 Schematic diagram for the propagator that brings a initial n-ball to a final ellipsoid.

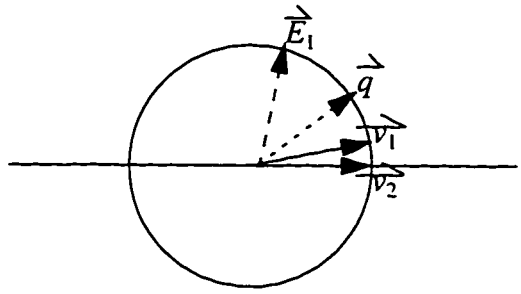

Figure 3.2 Display the eigenvectors, $\vec{v}_1$ and $\vec{v}_2$, of the system operator $\boldsymbol{L}$ on a unit circle. Also plotted is a vector $\vec{q}$, and the first singular vector $\vec{E}_1$ of the propagator $\boldsymbol{R}$.

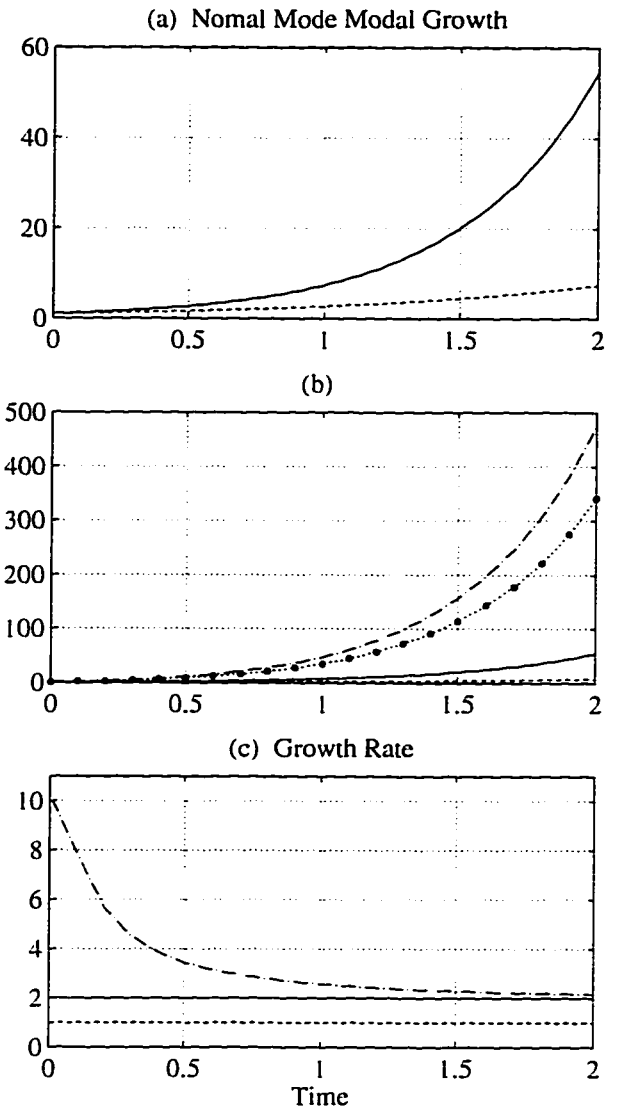

Figure 3.3 (a) The exponential growth of the normal modes of the system given in Eq. 3.1 and Eq. 3.9, i.e., the growth of the two eigenvectors, $\vec{v}_1$ (solid) and $\vec{v}_2$ (dashed), of the operator L. (b) The curves of panel (a) are repeated. The two additional curves are the growth associated with an arbitrarily chosen vector $\vec{q} = \begin{bmatrix} \frac{1}{\sqrt{2}} \\ \frac{1}{\sqrt{2}} \end{bmatrix}$ (the dotted line) and the growth associated with the first singular vector ($\vec{E}_1$, the dash-dot line) of the propagator matrix R. (c) the growth *rate* of $\vec{v}_1$ (solid), $\vec{v}_2$ (dashed) and $\vec{E}_1$ (dash-dot).

CHAPTER 4 GROWTH OF PERTURBATIONS IN THE TROPICAL PACIFIC SST: THE ROLE OF THE ANNUAL CYCLE AND THE ENSO CYCLE

4.1 Introduction

In this Chapter, we focus on the perturbation growth that results from perturbations that are prescribed at the initial time of the model integrations. These perturbations are assumed to be associated with the observational (measurement) uncertainties or initialization errors. In particular, we focus our efforts here on evaluating the sensitivity of the final state SST field to small perturbations in the initial state of the SST in the B88 model of the tropical Pacific climate system. An accurate prediction of the final state SST field has been the Holy Grail of short-term climate forecasts in the tropics because the low-frequency (e.g., seasonal to interannual) atmospheric circulation anomalies of global proportion are strongly related to tropical Pacific SST anomalies. The fact that we consider initial perturbations only to the model SST (and the associated wind field; see model description below) is justified not only by its intrinsic interest, but by our desire to answer whether errors in SST alone could be responsible for the errors in the actual forecasts of ENSO, even if the initial state of the thermocline were known exactly. This is not to deny the potential importance of thermocline perturbations to a full understanding of ENSO predictability[1].

The coupled atmosphere-ocean model used in this study is Battisti's (1988) version of the Zebiak and Cane (1987) model. The model is described in chapter 2. A brief description of the method used to obtain an approximate linear version of the full model is

1. Preliminary results from studies that determine the initial perturbations in both SST and thermocline depth that generate the maximum error growth in SST over an integration time of 2-months can be found in Chen (1993).

presented in section 4.2. We present in section 4.3 the optimal growth of perturbations as a function of the phase of the seasonal cycle and the ENSO cycle from which the integration is initiated. We discuss and interpret the results in the context of the model physics in section 4.4. Finally, section 4.5 contains our conclusions based on the major findings of this work. Preliminary results of singular vector calculations using this model were reported in Palmer *et al.* (1994).

4.2 Method

4.2.1 Calculation of the linear propagator *R*

Before we proceed with the singular vector analysis, we must first obtain the propagator for the linearized system. The propagator describes the evolution of perturbations about a reference trajectory. Rather than code a linearized version of the numerical model, we choose a simpler, approximate method of obtaining the propagator directly from the full coupled model. We follow the procedure outlined below:

(*i*) The full model is first integrated from the initial time t to some later time, $t+\tau$. This control integration represents a reference trajectory. In this study, we take τ to be 3, 6, or 9 months.

(*ii*) The integration is then repeated, placing a small positive perturbation of amplitude ε in one element of the state vector (i.e., one unit in one variable at one grid point and zero otherwise) at the initial time t. The perturbation at the final time ($t+\tau$) that is due to the initial perturbation applied at time (t) is given by the difference between the perturbed and the reference states at time $t+\tau$. The initial and final perturbation vectors are recorded as one column vector in the initial and final perturbation matrices X_i and X_f, respectively (see Eq. 4.1).

(*iii*) Step two is repeated, placing perturbations at each grid point of the state vector. Record the initial and final perturbation state vectors in matrices X_i and X_f accordingly.

This procedure (*i-iii*) generates the relation

$$\boldsymbol{R}(t, \tau)\, X_i = X_f, \qquad \text{(EQ 4.1)}$$

and was proposed in the meteorological literature as early as Lorenz (1965). Hence, the approximation to the linear propagator for the numerical model is $\boldsymbol{R}(t, \tau) = X_f X_i^{-1}$. As stated above, if we interpret the initial perturbation as the error or uncertainty at the initial time, *the maximum possible error growth over time* τ *is the first (largest) singular value of the propagator,* $\boldsymbol{R}$. *The initial and final patterns that accomplish this error growth are the right and left singular vectors of* $\boldsymbol{R}$.

4.2.2 The choice of the norm

We examine in this study the maximum growth of perturbations in the SST field of the coupled atmosphere/ocean model described in chapter 2 that results from uncertainties in the initial conditions in the SST field. We focus on identifying the spatial structure of the fastest growing perturbations in tropical SST (12°S-12°N) because the low-frequency tropical Pacific atmospheric circulation (thus the tropical climate) is intimately tied to the SST distribution in the equatorial Pacific. Furthermore, climate variability over the north Pacific sector has been shown to be statistically related to the SST distribution in the tropical Pacific (e.g., Ropelewski and Halpert 1987).

The choice of the norm must be consistent with the probability distribution of errors in the initial state (Molteni *et al.* 1995). In general this distribution is poorly

known. Previous studies of the stability of geophysical flows have focused on maximizing either the final state enstrophy (e.g., Farrell 1990) or total perturbation energy (e.g., Buizza and Palmer 1995; Moore and Kleeman 1995). Virtually all models used to forecast the state of the tropical Pacific climate system require at initialization time both the SST and the upper ocean density structure (or pycnocline position). Numerous models also impose the state of the global atmosphere in their initialization. We will limit this study to focus on how perturbations in SST at the initialization time evolve to produce the optimal amplification in SST at the end state. Hence, the state vector (see section 3.1) contains only the SST component, though $\boldsymbol{R}$ contains the full model physics for propagating the initial SST anomalies to the final state.

We apply two tests to determine whether the propagator generated by the method outlined above is a good approximation to the actual linear propagator. First, we follow steps (*i*)-(*iii*) using various values for ε, ranging from 0.01°C to 2°C, positive or negative. For all cases investigated, the largest singular value determined by using positive perturbations and negative perturbations agree to within 5%. The associated singular vector determined by these two approaches are also in excellent quantitative agreement. All results presented in this paper use $\varepsilon = 0.5$°C.

In the second test, the full numerical coupled model was initialized with the optimal perturbation (i.e., the first singular vector) obtained from the singular vector analysis, and the coupled model was integrated to obtain the final perturbation pattern. Both the final state pattern and the perturbation growth (amplification factor) obtained by integrating the full model were in good agreement with that obtained using the propagator $\boldsymbol{R}$. For the 6-month integrations that we have performed, the typical pattern correlation between the final state resulting from the nonlinear numerical model integration and that resulting

from the linear propagator is ~0.99; the amplification factor estimated by the linear propagator and by the nonlinear model is different by 1%-30%. Moreover, the growth in the numerical model shows a sensitivity to the sign of the initial perturbation, which is consistent with the effects of the "kink" in the model's parametrization of subsurface ocean temperature (see Appendix) (because that the shut-down of warm events occurs more rapidly than the set-up of the warm events and that the warm events grew more than cold events, the optimal perturbation favors one polarity of the perturbation).

4.3 Idealized Singular Vector Growth Experiments

4.3.1 Climatological annual cycle reference trajectory

We examine how the initial perturbations, applied in different months of the annual cycle, evolve over a chosen duration of τ = 3, 6 and 9 months. For this set of experiments the reference trajectory is exactly the prescribed climatological annual cycle. The initial and final state perturbations are deviations about the annual cycle. For the parameters used in this study, the coupled model annual cycle is unstable to infinitesimal perturbations (Battisti and Hirst 1989), and in the presence of any initial noise, a model ENSO cycle is eventually set up. However, the spatial structure of singular vectors for the time scales investigated here tends to be insensitive to whether or not the normal modes of the system are unstable, and the analysis presented here should carry over to the case in which the model is in a stable regime[1].

The growth of the first singular vector (i.e., the value of λ_1) is strongly dependent on the calendar month in which the perturbation is applied and on the duration of the inte-

1. We have carried out the experiments using δ=0.4 (the efficiency coefficient, see Eq. A11 in B88), a stable version of the B88 model. Qualitatively, the answer remains the same.

gration. The first singular values for three, six and nine month integrations are plotted in Fig. 4.1 as a function of the month in which the perturbed integration is started. The maximum growth for the 3-month integrations ranges from a factor of 2.7 for the integration that starts in June, to 1.1 for the integration that starts in January. In most cases λ_1 increases as the duration of integration increases. For the 6-month integration, λ_1 ranges from 5.9 for the April start, decreasing to 2.4 for the November start; for the 9-month integration, λ_1 ranges from 7.8 for the March start to 3.5 for the September start. The results point to a period of greater sensitivity during the boreal summer because the periods of maximum growth over 3, 6, and 9 months are all centered on this season.

The reader will note the circles plotted in Fig. 4.1, which indicate the first singular values associated with the propagator that is obtained in exactly the same manner as is outlined in section 3.1, but with negative initial perturbations (ε = -0.5°C) applied to the model in step (*ii*). The growth (λ_1), initial, and final state patterns of the optimal perturbation that are calculated from the propagator obtained by applying positive/negative perturbations to the model are in excellent quantitative agreement, suggesting we have obtained an good approximation to the linear propagator $\boldsymbol{R}$.

In contrast to the sensitivity of the singular values, both the initial and final patterns are *not* sensitive either to the month in which the initial perturbation is applied or to the duration over which the perturbation is allowed to grow. Plotted in Fig. 4.2 are the optimal initial patterns, $\vec{E_1}$ (left hand column, recall $\|\vec{E_1}\| = 1$), and the corresponding final patterns $\lambda_1\vec{F_1}$ (which result from applying the propagator to the optimal initial pattern), for the 6-month integrations, starting from January, April, July and October, respectively. The initial pattern consists of an east-west dipole spanning the entire tropical

Pacific basin superimposed upon a north-south dipole in the eastern tropical Pacific. The final pattern resembles the *mature* model ENSO mode. The patterns for the three, nine and twelve month integrations are very similar to those for the six-month integrations and are not shown.

The second singular vectors indicate decay for all of the monthly starts and for all durations of integration that were examined (3, 6, 9 and 12 months). Note that as the integration time increases, the optimal initial pattern explains a higher proportion of the total information in of $\boldsymbol{R^*R}$. The trace of the matrix $\boldsymbol{R^*R}$ is proportional to the variance of perturbations which are initially uniformly distributed (Lorenz 1965; also our Eq. 4.1, with X_i set to the identity matrix). The first singular vector accounts for 18-60% of the total variance of $\boldsymbol{R^*R}$ for the 3-month integrations, and 88-97% and 97-99% for the 6 and 9 month integrations, respectively.

4.3.2 ENSO with annual cycle in basic state as reference trajectory

We next examine how the interannual variability in the coupled atmosphere/ocean model affects the growth of initial perturbations in the SST. The freely evolving coupled model with a seasonal cycle in its basic state (SST, ocean currents, upwelling, thermocline depth and surface winds) supports interannual variability that resembles the observed ENSO, with model ENSO events occurring 3 or 4 years apart (Battisti 1988). Fig. 4.3a shows a 20-year time series of the control-run Niño 3 index. The extrema of model SST anomalies range from 2.6°C in the warm phase to -2°C in the cold phase. We arbitrarily select the ENSO cycle occurring during model years 9, 10, and 11 for further analysis. Fig. 4.3b shows the time-longitude section of the equatorial SST anomalies, averaged from 2°S to 2°N, for this typical model ENSO cycle.

To determine the optimal perturbations for selected phases of the control integration, restart files were written every month during the control integration. These restart files contain the initial conditions to which we add small perturbations and calculate the singular vectors, as described in section 3.1. The fundamental difference between these calculations and those presented in section 4.3.1 is summarized as follows. The reference trajectory in the experiments of section 4.3.1 is the climatological annual cycle. The reference trajectory (the control integration) for the experiments described in this section is a freely evolving model ENSO cycle with the annual cycle in its basic state (see, e.g., Fig. 4.3a).

Singular values and singular vectors are calculated for three and six month integrations starting from each month of the selected ENSO cycle. The first integration starts in January of year 9, denoted Jan(9), and the last integration starts in Jan(12). The values of the 6-month optimal perturbation growth (λ_1) for every three months are shown along the right hand side of Fig. 4.3b. The three and six month optimal growths are plotted in Fig. 4.4 along with the Niño 3 index.

The perturbation growth depends on both the phase of the annual cycle and the phase of the model ENSO cycle. For example, in the 3-month integrations, the growth is largest for Oct (9) ($\lambda_1 = 2.9$), just prior to the onset of the model ENSO event, and for May (11) ($\lambda_1 = 3.2$), just prior to the breakdown of the model ENSO event. The growth over 6-month integrations generally exceeds the growth over 3-month integrations, with a large growth ($\lambda_1 > 3$) throughout the ENSO cycle. Exceptions occur at the peak of the warm event (Aug(10)-Jan(11)) and during the demise of the warm event (Jun(11)), continuing through the first half of the model cold event (Apr(12), not shown), where the 6-month optimal perturbation actually decays ($\lambda_1 < 1$).

Examples of the patterns of the initial and final state SST that are associated with the optimal growth of SST for the 6-month integrations of the freely evolving coupled model are displayed in Fig. 4.5. While the maximum perturbation growth is sensitive to the phase of the ENSO cycle in which the perturbation is applied, and hence to the state of the coupled system, both the initial and final patterns of the optimal perturbation are insensitive to the initial conditions (compare Figs. 4.2 and 4.5).

4.3.3 Annual mean basic state reference trajectory

To isolate the effect of the ENSO cycle from that of the basic state annual cycle, we performed experiments in which the annual cycle is eliminated from the model. To accomplish this, we prescribe a basic state for the coupled model that is the *annual mean* climatological SST, ocean surface currents, upwelling, thermocline depth, and surface wind stress. In this third experiment we perturb the model about the time-invariant trajectory that is exactly the annual mean climatology. The 3-month and 6-month optimals have first singular values of 2.0 and 4.2, respectively. The spatial pattern of the optimal perturbation in SST is very similar to those shown in Figs. 4.2 and 4.5 and is not shown.

4.3.4 ENSO with annual mean basic state as reference trajectory

The model with the annual mean basic state (see section 4.3.3) supports a freely evolving ENSO cycle with a regular period of 3.45 years and with extrema in the Niño 3 index of 2.1°C and -1.4°C. The propagator and singular vectors were obtained following the same procedure as described in section 3.1, but using this freely evolving ENSO with no annual cycle as the reference state. The maximum perturbation growth as a function of the phase of the ENSO cycle in which the integration starts is displayed in Fig. 4.6. The maximum growth for both the 3-month ($\lambda_1 = 2.7$) and 6-month ($\lambda_1 = 5.4$) integrations is

achieved just prior to the transition from a cold to warm state (month 7 of year 10); a secondary peak in growth in the 6-month integration occurs just prior to the beginning of the demise of the warm event (the first month of year 12). For the 3-month integrations, growth is small just prior to the peak phase of the warm event, and growth is extraordinarily small throughout the first half of the cold phase. For the 6-month integrations, no growing singular vectors are found throughout the first half of the cold phase.

The spatial pattern of the optimal perturbation bears a strong likeness to that for the annual cycle reference trajectory (Fig. 4.2), and for the "ENSO with annual cycle" reference trajectory (Fig. 4.5). Overall, Figs. 4.1, 4.4 and 4.6 indicate that the interannual variability generally stabilizes the system to SST perturbations except for the periods immediately preceding the onset and demise of the model ENSO warm event. These results are discussed further in sections 4.4 and 4.5.

4.4 Discussion

Three general phenomena stand out in the above experiments. (*i*) The spatial patterns of the optimal initial perturbation in SST and the resulting final perturbation show almost no dependence on the phase of the annual cycle, the phase of the model ENSO cycle, or the time over which the perturbation is allowed to grow. (*ii*) The final perturbation pattern is very similar to the first empirical orthogonal function (EOF) of the SST from the freely evolving coupled model (i.e., the model ENSO mode; see Mantua and Battisti 1995). (*iii*) The perturbation growth is sensitive to both the annual cycle and the ENSO cycle. Here we present an interpretation of these phenomena based on the physics and dynamics of the model.

The robust initial SST perturbation pattern has a simple physical interpretation. The anomalous atmospheric circulation that would result from the optimal initial SST perturbations shown in Figs. 4.2 and 4.5 includes a relaxation of the southeasterly trade winds in the central-eastern basin along the oceanic equatorial wave guide (5°S-5°N). To illustrate this point, we apply the 6-month optimal perturbation for the climatological October condition (i.e., Fig. 4.2d) in the coupled model and integrate forward. The sign of the perturbation is chosen so that it evolves into an ENSO warm event. Fig. 4.7 plots the response in various fields at day 10 (left column) and month 3 (right column) of the perturbed integration (perturbations about the climatological annual cycle). Because of the spatially varying climatological winds, the initial SST perturbations (Fig. 4.2d) lead to maximal zonal and meridional wind stress anomalies in the central and eastern equatorial Pacific (see Fig. 4.7b and a close-up in Fig. 4.8). The anomalous westerly wind stress in the central Pacific leads to a warming of the ocean in the central and eastern equatorial Pacific (Fig. 4.7a) by (1) depressing the pycnocline both locally and in the eastern equatorial Pacific (Fig. 4.7e), thus reducing the entrainment rate (Fig. 4.7d), and (2) increasing anomalous zonal warm advection in the surface layer (Fig. 4.7c).

The north-south asymmetry across the equator in the eastern Pacific is a robust feature of the first singular vector. For the polarity chosen above, it immediately results in a northerly wind anomaly across the equator (Fig. 4.8). This represents a relaxation of the mean southerly wind stress in the equatorial eastern Pacific (~5°S-5°N) that acts to warm the eastern near equatorial ocean by decreasing the upwelling of cold water into the surface layer. At first this result was surprising, though in retrospect it could have been anticipated from the basin adjustment study of Philander and Pacanowski (1981) and from the sensitivity studies reported in Battisti (1988, section 4c).

The annual cycle is seen to modulate the growth of the optimal perturbation about a reference trajectory when the ENSO cycle is included (compare Figs. 4.1, 4.4 and 4.6). In general, the presence of the ENSO cycle suppresses the sensitivity of the system to initial perturbations compared to the sensitivity about the annual cycle alone. To elucidate this point, we compare the mean 6-month optimal growth in the four experiments. When the ENSO cycle is added to the annual mean (Fig. 4.6, section 4.3.4), the average of the first singular values throughout a complete cycle is 2.6 - much less than 4.2, the first singular value for the annual mean reference trajectory (section 4.3.3). The only times when the first singular value is greater than 4.2 are in months 5-9 of year 10, just prior to the onset of an ENSO warm event (Table 4.2). At this time the, system is close to its climatological mean state in SST and thermocline depth in the eastern Pacific, and is therefore most sensitive to perturbations. The same conclusion holds when the annual cycle is included. The average of the 12 first singular values of the annual cycle reference trajectory is 4.0 (Fig. 4.1, section 4.3.1). When the ENSO cycle is added to the annual cycle (Fig. 4.4, section 4.3.2), the average of the first singular values throughout a complete cycle is 2.9 - again, less than 4.0 (Tables 4.1-4.2).

The ENSO cycle alone is most sensitive to SST perturbations during the transition from cold to warm Niño 3 SST (and, to a lesser extent, to the transition from warm to cold). In Fig. 4.9, we compare the first singular values for the annual-cycle reference trajectory (also displayed in Fig. 4.1) with the first singular values for the freely evolving model ENSO trajectory (also displayed in Fig. 4.4) for 3-month (Fig. 4.9a) and 6-month (Fig. 4.9b) integrations. The only time during the ENSO cycle that the amplification of the 6-month optimal perturbation growth is enhanced compared to the amplification about the climatological reference trajectory is for perturbations that are applied just prior to the transition from a cold to warm phase of ENSO (Aug(9) to Feb(10) in Fig.

4.9b). However, for the 3-month integrations, the ENSO cycle enhances the perturbation growth prior to *both* the transition from cold to warm conditions (Aug(9) - Apr(10)) and the transition from warm to cold conditions (Apr(11) - Jun(11) in Fig. 4.9a).

The nonlinear ENSO model trajectory can be thought of as an attempt of the nonlinear dynamics to adjust by evolving into parts of phase space which are less unstable than the basic state itself. (S. Zebiak, personal communication to T. Palmer). For example, the farther the system is from climatology, the more the nonlinear terms reduce the local instability in the eastern Pacific. Hence, one might generally expect that the singular vectors of the model ENSO basic state are smaller than the climatological basic state. Indeed, the dominant reason for the general suppression of growth by inclusion of the ENSO cycle is that throughout most of the warm and cold phases of the ENSO cycle, the thermocline along the equator is far from its climatological position. Initial perturbations in the SST field will generate anomalies in the wind stress field which, in turn, will force thermocline perturbations. In the warm phase, the thermocline is positioned deeper and the upwelling is weaker than in the climatological mean fields at the same time of year. Hence, a perturbation, applied to the model while it is in a warm phase, will lead to less growth in the final state than for the same perturbation added to a climatological mean state. Similarly, perturbations applied to the model while it is in the early and middle stages of a cold phase grow less rapidly than perturbations applied to climatological mean conditions because the thermocline is sufficiently shallow. In the cold phase of ENSO, large downward excursions of the thermocline are required to change the temperature of the water that is being entrained into the mixed layer and the upward displacement is limited by the turbulent mixing at the surface (see the Appendix). The greater sensitivity shown during the ENSO transitions, compared to the sensitivity of the basic state alone is not well under-

stood, but it most likely involves an additional effect due to the inertia present in the form of oceanic Rossby and Kelvin waves during ENSO transitions.

To understand which physical processes contribute significantly to singular vector growth, we performed several experiments using modified versions of the coupled model. Here, we will report on experiments in which we remove individual terms in the SST equation and then calculate the singular values for the annual cycle reference trajectory. These singular values are compared with those from the full model (section 4.3.1).

The first set of experiments illustrate the importance of thermocline displacements (and the consequent anomalous subsurface temperatures) to perturbation growth by comparing the average of the singular values obtained for the 3-month optimals about the annual cycle, with and without the inclusion of this process in the SST equation. The results from the full model (Fig. 4.10 heavy solid line, repeated from Fig. 4.1) indicate that the average of the 12 singular values for the 3-month optimal growth (i.e., the average growth over the annual cycle) is 2.0. However, when thermocline anomalies are not allowed to affect SST[1], the annual average of the singular value for the 3-month optimal perturbation is 0.8, and there are no months that support growing perturbations ($\lambda_1 < 1$ for all months; see Fig. 4.10 dotted line).

The net horizontal temperature advection in the surface layer also affects the amplitude of the singular values, though to a lesser extent than the thermocline displacements. For example, when all horizontal advection terms are removed from the SST equation, the analysis indicates that integrations beginning in all months except January and February support growing perturbations (Fig. 4.10 solid line); the annual average of the

1. This is accomplished by setting $T_s = 0$, as discussed in the Appendix (see Eq. A.1).

first singular values for the 3-month optimal for the model without horizontal advection is 1.3. Among the four components of the horizontal advection: *(i)* $u_{sfc} \cdot \frac{\partial}{\partial x}(\bar{T} + T)$, *(ii)* $v_{sfc} \cdot \frac{\partial}{\partial y}(\bar{T} + T)$,*(iii)* $\bar{u}_{sfc} \cdot \frac{\partial T}{\partial x}$, and *(iv)* $\bar{v}_{sfc} \cdot \frac{\partial T}{\partial y}$, the most important term for determining growth is the meridional advection by the mean flow (term *(iv)*, Fig. 4.10 dashed line). The least important term is the zonal advection by the mean flow (term *(iii)*, Fig. 4.10 dash-dot line): neglecting this term leads to 3-month singular values which differ from those of the full model by less than 4%.

The initial perturbation in SST evolves into a final SST perturbation pattern that closely resembles the most unstable eigenmode of the coupled model (Battisti and Hirst 1989). Since the pattern of the final SST perturbation is largely independent of the duration for growth over a time period of 3 months or more, it is tempting - but incorrect - to interpret the final perturbation pattern as the most unstable eigenmode of the coupled system. This pattern is achieved in only about three months, while the time-scale associated with setting up the eigenmode is approximately determined by the adjustment time of the equatorial waveguide, which is about 9 months. Nevertheless, the rotation in phase-space of the dominant singular vector from an initial direction which is essentially orthogonal to the fastest growing normal mode, towards a final direction which is almost parallel to the fastest growing normal mode, is a general characteristic of optimal perturbation growth when there is an unstable normal mode (see Buizza and Palmer 1995).

For perturbations that grow over a time that is short compared to the basin adjustment time, the growth is best thought of as being due to a *local* atmosphere-ocean instability that is optimally realized by the initial perturbation previously discussed; the localization is due to the asymmetries of the climatological mean state (Battisti and Hirst

1989). Inspection of Fig. 4.1 indicates that maximum growth is realized in the boreal summer months: the maximum growth occurs in the 3-month integration spanning June-July-August, and in the 6-month integration spanning April-October. The period of weakest growth occurs in late boreal winter and boreal spring: the weakest growth over a 3-month interval is from January through April, and over a 6-month interval, from November through the next May. The explanation for the seasonal dependence lies in the seasonality of the strengths of the mean upwelling and the mean meridional current $\bar{v}_{sfc}$. Both are largely determined by the wind-driven Ekman transport and are maximal in amplitude in the late boreal summer. Hence, the processes that most amplify the optimal initial SST perturbation are also responsible for the strong seasonality in the amplification of the optimal perturbation. This seasonal dependence in the 3 and 6 month integrations is consistent with Battisti's (1988) results concerning the seasonality in the local stability properties of the mean state of the atmosphere-ocean system in the eastern equatorial Pacific.

4.5 Conclusion

We have examined the sensitivity of the Battisti (1988) coupled atmosphere-ocean model to perturbations in the sea surface temperature (SST) field applied at the beginning of model integrations. The spatial structures of the fastest growing SST perturbations are determined by singular vector analysis of an approximation to the propagator for the linearized system. Four reference trajectories are analyzed: *(i)* the annual cycle, *(ii)* a freely evolving model ENSO cycle with the annual cycle in the basic state, *(iii)* the annual mean climatology (i.e., seasonless), and *(iv)* a freely evolving model ENSO cycle with an annual mean basic state. Singular vectors with optimal growth for these idealized scenarios over periods of 3, 6 and 9 months are computed. Parallel analysis of the integrations with a sta-

ble version of the numerical model indicates that all of the major results presented in this paper are independent of whether or not the model supports an unstable eigenmode.

The magnitude of maximum growth is shown to be highly dependent upon both the phase of the annual cycle and the phase of the ENSO cycle at which the perturbation is applied and upon the duration that perturbations are allowed to evolve. However, the spatial structure of the optimal perturbation is remarkably insensitive to these factors. The structure of the optimal perturbation consists of an east-west dipole in the entire tropical Pacific basin superimposed on a north-south dipole spanning the eastern tropical Pacific, and has a simple physical interpretation. The growth is facilitated by two processes (illustrated here for perturbations which lead to warming): *(i)* weakened trades associated with the optimal SST perturbation lead to a deepening of the thermocline in the eastern equatorial Pacific and warming of the surface by changing the temperature of the water being entrained into the mixed layer. The weakened meridional wind stress along the equator in the eastern Pacific reduces the strength of upwelling, which also enhances warming; *(ii)* meridional advection of the optimal SST anomalies also contributes significantly to the perturbation growth.

The maximum growth takes place for integrations that include the period June-August, and the minimum growth for integrations that include the period January-April. The seasonal dependence of the optimal perturbation growth is consistent with the seasonality in the local stability of the coupled system in the central and eastern Pacific basin.

Maxima in the singular vector growth also occur at specific phases of the model ENSO cycle, with the largest amplifications occurring prior to the onset and decay of the ENSO warm phases, while minima occur for integrations starting at the peak of the warm event, after the transition from a warm to a cold phase, and continuing into the cold event.

Nonetheless, the overall effect of the ENSO cycle is to reduce the optimal growth compared to growth on the annual-cycle-alone reference trajectory.

It is notable that the spatial structure of the optimal perturbation in SST is of large zonal scale (~15,000 km). This is consistent with an analysis of the atmospheric response as a function of the zonal scale of the atmospheric heating anomaly. In this model the heating is roughly proportional to the SST anomaly. Achieving the greatest dynamical response in the equatorial waveguide (so that the ocean dynamics will be instrumental in affecting the SST later) requires forcing by a zonal wind stress anomaly within the equatorial waveguide (Clarke 1982). It can be shown that for the Gill-type models used in this and other coupled models of ENSO, the zonal wind stress anomaly in the equatorial waveguide, which results from a given amplitude of heating (SST) anomaly, is maximized when the heating has a zonal scale that is roughly the longitudinal extent of the Pacific Ocean basin ~15,000 km. The combination of maximum amplitude response and a large zonal extent ensures that the dynamical response in the ocean will be optimally realized when the initial perturbation in the SST is large-scale.

The wind stress (e.g., Fig. 4.8) and SST patterns (Fig. 4.2 and Fig. 4.5) could certainly correspond to plausible errors in the initial conditions for a coupled ocean/atmosphere model forecast if they were obtained from standard analyses of global observations. In practice, with limited observational data, such errors are often strongly determined by the ability of the atmospheric model used in the analysis to simulate the strength of the divergent circulations over the Pacific basin, which in turn, is related to the quality of the physical parameterizations in the atmospheric model. The ubiquitous initial singular vector we have found, which is associated with a weakening in the SST gradient across the Pacific basin, is consistent with an erroneously weak Walker circulation in the

atmospheric initial state. On the basis of this argument, an initial state with excessively strong divergent circulations would be equally likely.

The model employed by D. Chen *et al.* (1995) and previous versions of the ZC model do not use SST observations in their initialization scheme. Instead they initialize their forecast model using analyzed winds. If these winds are incorrect in the sense discussed above, then their initialization scheme could lead to initial SST errors which project strongly onto our first singular vector.

In most cases examined, the optimally growing pattern is the *only* growing pattern. Because the final pattern is similar to the model ENSO, this means that incorrect forecasts of the magnitude, the timing, or even the sign of an ENSO event could be compensated for by small corrections to the SST field at the time of the forecast. If the (measurement) error in SST projects strongly onto the first growing singular vector and is not removed from the initial conditions, large errors in the forecast will result. For example, if the error in the initial SST field had the pattern displayed in Fig. 4.5a with a maximum amplitude of 0.1°C, it would grow in 6 months to have a rather large error, with maximum amplitude of 0.9°C in SST, and a similar pattern to the observed ENSO phenomenon. On the other hand, because the error growth is dominated by only one growing pattern, forecast errors that do not project onto the final pattern cannot be compensated for by small corrections in initial SST alone. Therefore much of the observed SST variability outside of the equatorial waveguide cannot be better predicted by a better SST initialization using this model.

Finally, we note that Moore and Kleeman (1995; hereafter MK) have calculated the optimal growth patterns and rates for a coupled atmosphere-ocean model of the tropical Pacific and find somewhat different results from whose we have presented for the Bat-

tisti (1988) model. One important difference between these two studies is in the choice of which variables are initially perturbed and how the growth is measured. We have chosen to optimize the amplitude of the final state SST perturbation due to perturbation (uncertainty) in the SST field at the beginning of the integration. In contrast, MK optimize the total perturbation energy in the coupled system due to an initial perturbation in the total perturbation energy. MK find that the initial SST perturbations, which make up part of their optimal perturbation energy, is characterized by very small zonal scales, which are quickly damped to reveal the large scale structure. In addition, a large portion of the optimal error growth in the MK model is attributed mainly to perturbations in the ocean dynamics and less so to the accompanying SST perturbations.

We did not choose to perform calculations to optimize the total perturbation energy using our model, but one might anticipate that the initial optimal patterns will be sensitive to the choice of the norm that is being optimized (which is specific to the problem being analyzed) (Farrell 1989). We note, however, that the initial optimal perturbations in SST obtained by Thompson *et al.* (1996) for the Hirst (1988) model suggest the optimal SST patterns are of large-scale for a variety of norms, and important contributions to the amplification of SST are associated with the initial perturbations in SST, and less so in the perturbations of the dynamics.

Another likely explanation for the differences in the structure of the SST pattern associated with the optimal perturbation for the two models involves the differences in model physics. There are large differences in the governing equations for the two coupled models. In particular, MK make several assumptions that simplify the air-sea coupling and the SST equation used in the present study. Differences in the prescription of the atmospheric heating rate corresponding to a given SST field, and hence, differences in the coupling between the ocean and atmosphere, may also play a role. It is well known that

fundamental differences in the nature of the interannual variability simulated by freely evolving coupled models arise because of seemingly subtle changes in the ocean thermodynamics (e.g., Hirst 1986). Thus, we expect that even subtle differences in the ocean thermodynamic equation between the two models may greatly affect the optimal growth.

Blumenthal (1991) examined the optimal perturbation growth for the Zebiak and Cane (1987) model by first constructing a low-order Markov model that is a best fit to the output of the full numerical Zebiak/Cane coupled model, and then calculating the adjoint of the normal modes of this Markov model. The adjoint vectors are closely related to our singular vectors in that they provide an initial condition which efficiently excites the model ENSO mode, although they are not necessarily "optimal" for growth over a finite time interval. His choice of norm gives equal weight to thermocline displacement, wind stress and SST perturbations. Several properties of the optimal growth associated with this Markov model are also common to our numerical model: (*i*) there is one adjoint that grows much faster than all other singular vectors; (*ii*) the largest (smallest) 9 month growth is associated with perturbations applied in spring (fall); (*iii*) the SST component of the adjoint is of large-scale (though with a structure that is different from that shown in this study); and (*iv*) the adjoint evolves into a final state whose SST pattern is very similar to the ENSO footprint.

Penland and Sardeshmukh (1995), using a linear stochastic ENSO model derived from observations, also find only one growing singular vector. The large-scale aspects of this singular vector possess some similarity to the singular vectors in the present study, particularly in the north-south and east-west SST gradients in the Eastern tropical Pacific. However, their pattern includes a warm anomaly just east of the dateline and a banded structure in the Northern Hemisphere subtropics which are not seen in the optimal

perturbations of our model. Their pattern also has large amplitude in the Indian ocean, a region which was not included in our study.

The concordance between the results from the Markov model (Blumenthal 1991), the statistical model (Penland and Sardeshmukh 1995), and dynamical models (MK and this study) gives further credence to the idea that predictions of ENSO are usually sensitive to only one pattern of initial SST error.

TABLE 4.1 Leading singular values calculated from 6-month integrations starting from each calendar month about the annual cycle climatological trajectory and the annual mean climatological trajectory. Values in the second column that are greater than its mean value are shaded.

6-Month Integration Starting Month	Annual Cycle	Annual Mean
January	3.0568	
February	4.0583	
March	5.2203	
April	5.9360	
May	5.9156	
June	5.3052	4.1832
July	4.5363	
August	3.8253	
September	3.1585	
October	2.6561	
November	2.4040	
December	2.4625	
MEAN	**4.0446**	**4.1832**

TABLE 4.2 Leading singular values calculated from 6-month integrations starting from each month of a chosen freely-evolving model ENSO cycle on the annual cycle (second column) and the annual mean (third column) climatological basic state trajectories. Values in the second and third columns that are greater than the mean values reported in Table 4.1 are shaded.

6-Month Integration Starting Time: Model month_year_day	Standard: ENSO plus Annual Cycle	ENSO Plus Annual Mean
JAN9_2940	1.1471	
FEB9_2970	1.6263	
MAR9_3000	2.2626	
APR9_3030	2.8268	
MAY9_3060	3.5644	
JUN9_3090	3.9986	
JUL9_3120	4.2872	1.0123
AUG9_3150	4.4134	1.1753
SEP9_3180	4.8067	1.3956
OCT9_3210	4.8072	1.5168
NOV9_3240	4.0504	1.6446
DEC9_3270	3.5101	1.8894
JAN10_3300	3.6188	2.2076
FEB10_3330	4.1548	2.5856
MAR10_3360	4.8081	3.3258
APR10_3390	4.9944	4.0955
MAY10_3420	4.6138	4.6627
JUN10_3450	3.8373	5.1814
JUL10_3480	3.2808	5.3662
AUG10_3510	2.8272	4.8519
SEP10_3540	2.4060	4.3797
OCT10_3570	2.0902	4.1288
NOV10_360	1.9041	3.8018
DEC10_3630	2.0489	3.4548
JAN11_3660	2.5107	3.2596

TABLE 4.2 Leading singular values calculated from 6-month integrations starting from each month of a chosen freely-evolving model ENSO cycle on the annual cycle (second column) and the annual mean (third column) climatological basic state trajectories. Values in the second and third columns that are greater than the mean values reported in Table 4.1 are shaded.

FEB11_3690	3.6046	3.1348
MAR11_3720	4.1985	2.9266
APR11_3750	4.3487	2.8047
MAY11_3780	3.4251	2.6704
JUN11_3810	2.3920	2.6231
JUL11_3840	1.4293	2.6691
AUG11_3870	0.9718	2.7364
SEP11_3900	0.6959	2.8990
OCT11_3930	0.5857	3.1087
NOV11_3960	0.5597	3.4883
DEC11_3990	0.6652	3.8941
JAN12_4020	0.9612	3.9163
FEB12_4050		3.4523
MAR12_4080		2.7872
APR12_4110		1.9895
MAY12_4140		1.3512
JUN12_4170		0.9496
JUL12_4200		0.7377
AUG12_4230		0.6516
SEP12_4260		0.6345
OCT12_4290		0.6878
NOV12_4320		0.7917
DEC12_4350		0.8458
JAN13_4380		1.0427
MEAN	2.9252	2.6216

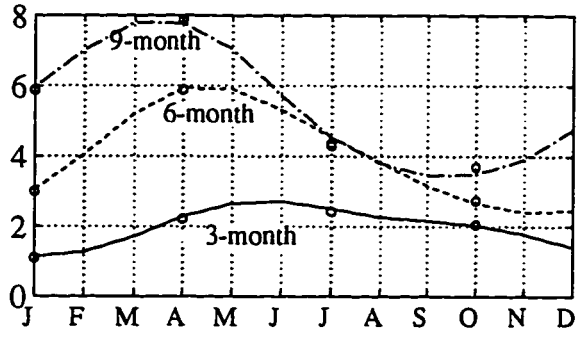

Figure 4.1 The optimal growth of SST (λ_1, the first singular value of R) as a function of the phase of the annual cycle, for 3-month (solid), 6-month (dashed) and 9-month (dash-dot) integrations about the prescribed climatological annual cycle reference trajectory (see section 4.3.1). For example, the maximum perturbation growth over a 6-month period starting in April and ending in October is 5.9. The initial amplitude of SST in perturbed integrations (see section 3.1, step *ii*) is ε = 0.5°C. The first singular values calculated using ε = -0.5°C are indicated by circles.

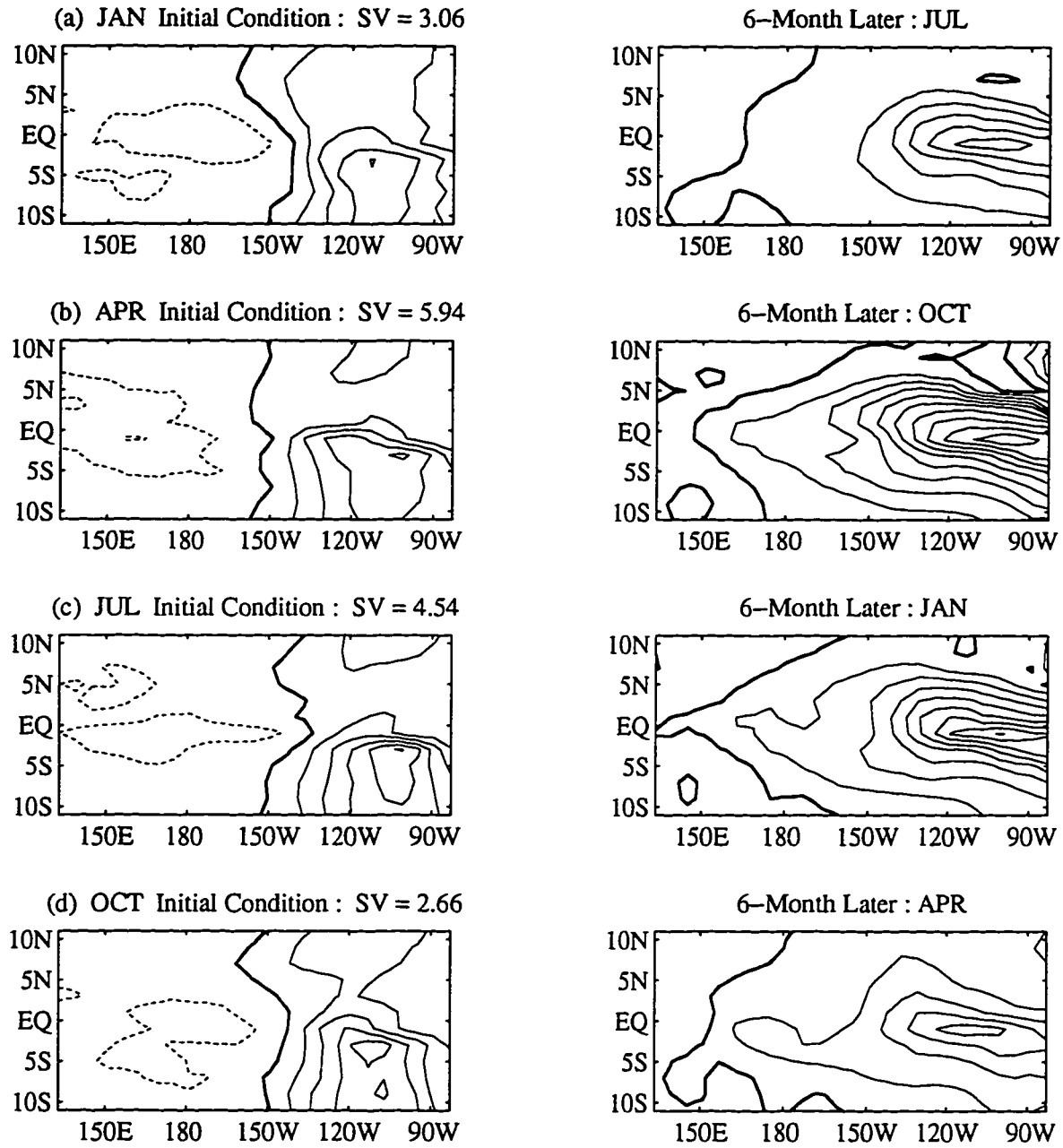

Figure 4.2 (a) The optimal SST perturbation applied in January (left) that produces the maximum amplitude in SST six months later in July (right). Panels (b), (c) and (d) are for optimal perturbations applied in April, July and October, respectively. The contour interval for the initial (final) perturbations in the left (right) column is 0.04°C (0.12°C). For each case, λ_1 is noted above the left panel.

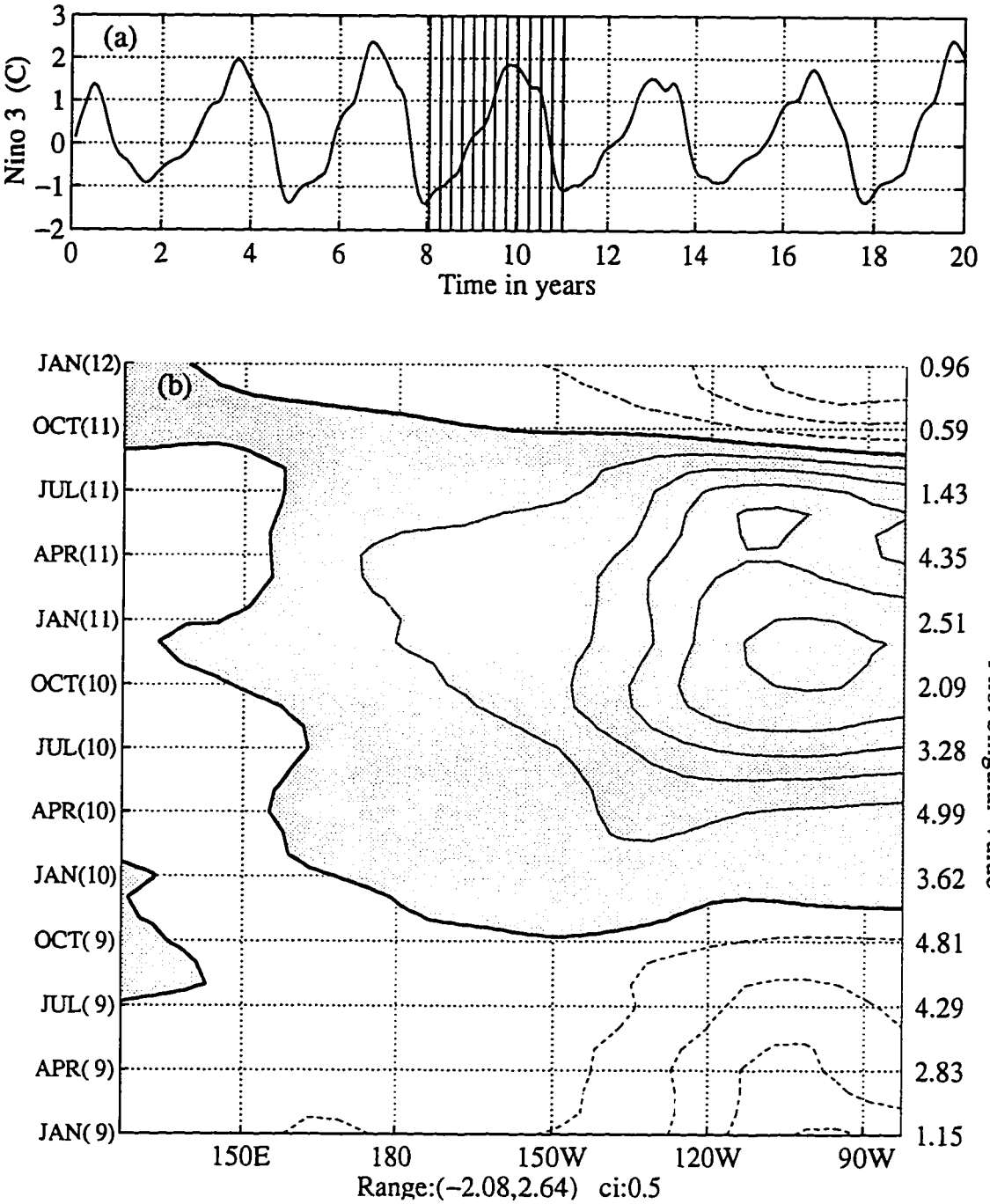

Figure 4.3 (a) 20-year time series of the Niño 3 index from the control integration of the coupled atmosphere-ocean model. (b) Time-longitude section of SST from the (arbitrarily chosen) fourth model ENSO cycle (SST is averaged from 2°S to 2°N; contour interval is 0.5°C). Positive (negative) contours are in solid (dashed) lines. Zero contours are in heavy lines. The first singular values for 6-month integrations starting with different months/ phases (indicated by vertical lines in (a)) are written on the right ordinate

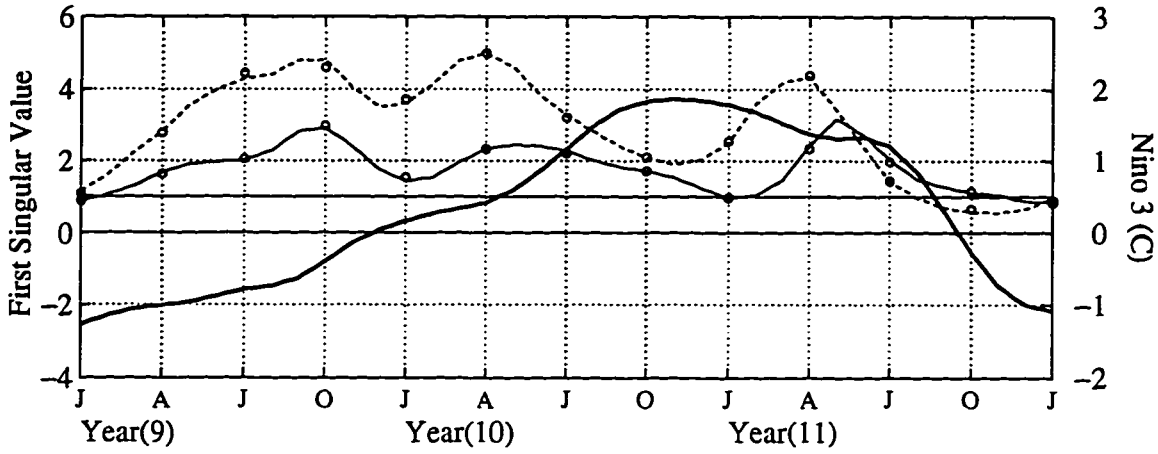

Figure 4.4 The first singular value (λ_1) for 3-month (thin solid) and 6-month (dashed) integrations performed on a freely evolving model ENSO reference trajectory, which includes both the interannual variability and the prescribed annual cycle (see section 4.3.2, $\varepsilon = 0.5°C$). The Niño 3 index (the fourth cycle in Fig. 4.3a) is indicated by the bold solid line and serves as a useful index of the reference for the state of the coupled atmosphere-ocean model (units denoted on the right ordinate). The circles indicate the first singular values with $\varepsilon = -0.5°C$. The zero line is plotted as a reference to separate the positive from the negative anomalies in the Niño 3 index. A horizontal line with λ_1 equals one is plotted as a reference, separating the growing singular values from the decaying singular values.

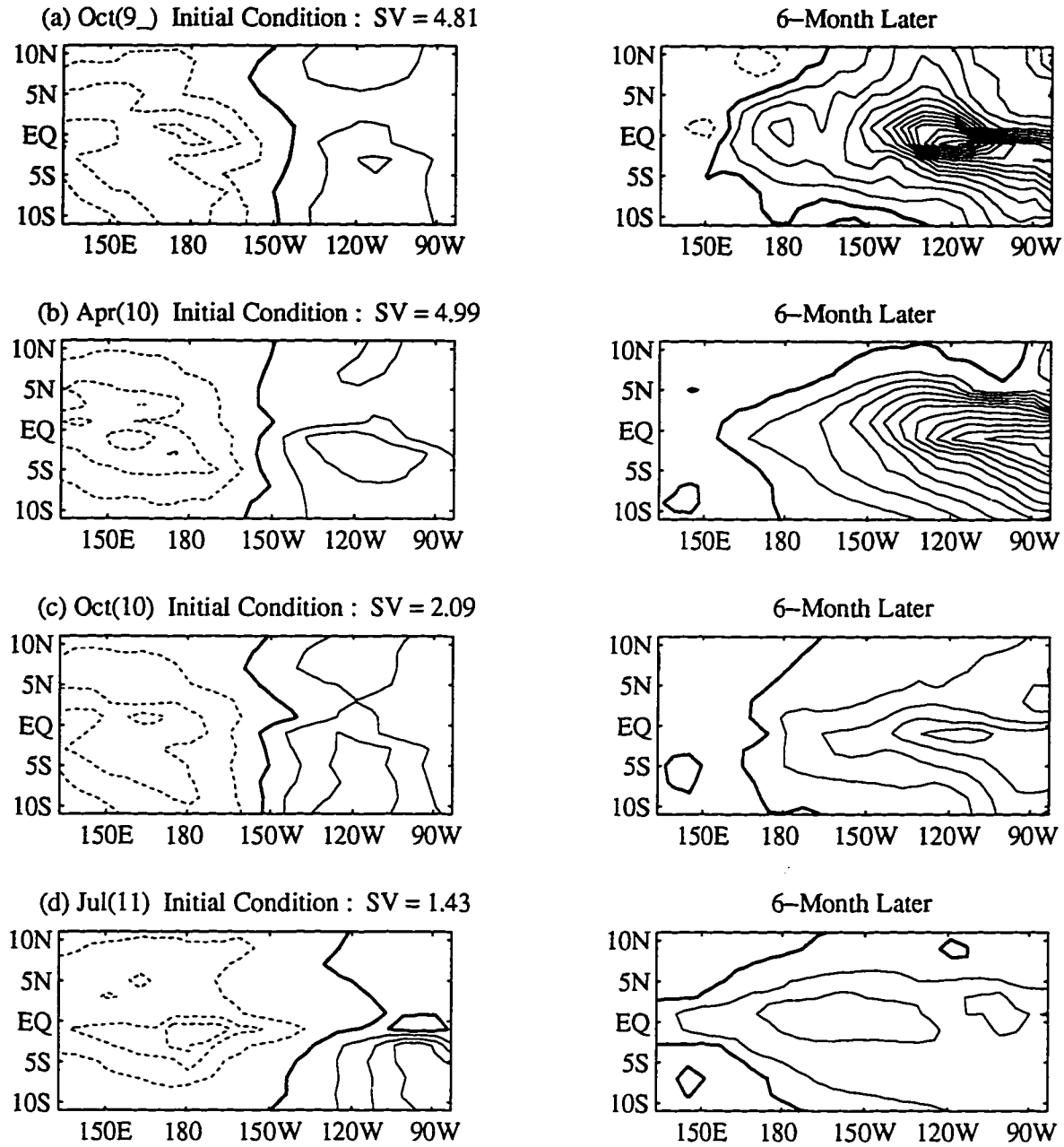

Figure 4.5 As in Fig. 4.2, but for 6-month integrations performed on a freely evolving model ENSO reference trajectory, which includes both the interannual variability and the prescribed annual cycle. Plotted in left (right) columns are the initial (final) patterns of the optimal perturbation for integrations starting at a specific phase of the model ENSO cycle: (a) prior to event onset [Oct(9)]; (b) during a warming phase [April(10)]; (c) at the peak of a warm event [Oct(10)]; (d) during the decaying phase [July(11)]. Contour interval in the left (right) column is 0.04°C (0.08°C).

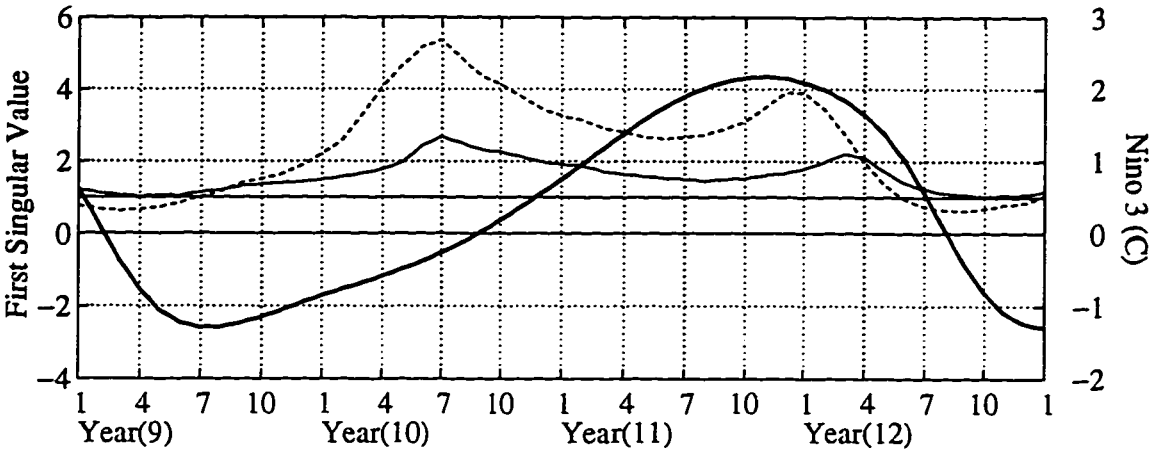

Figure 4.6 As in Fig. 4.4, but using for the annual mean basic state.

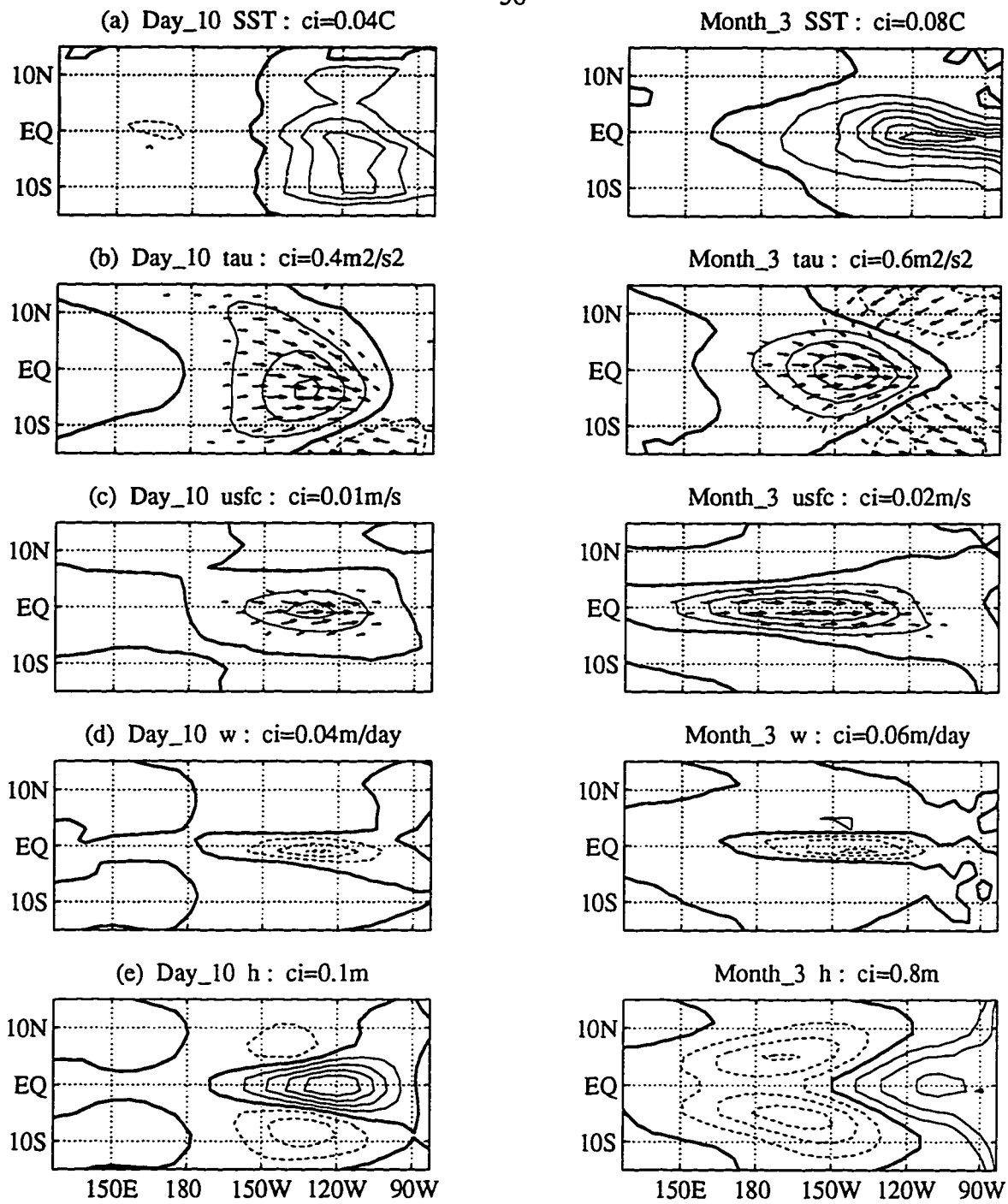

Figure 4.7 Coupled model response (15°S-15°N) in various fields after the 6-month optimal perturbation in SST (first singular vector, Fig. 4.2d) associated with the climatological October condition is applied: (a) SST, (b) surface wind stress, (c) surface current, (d) upwelling and (e) the thermocline depth perturbations. Left-column panels plot the day 10 response and right-column panels plot the model response at 3 months. Contour interval is noted for each panel. Panels b-c contour the zonal component of the vector field.

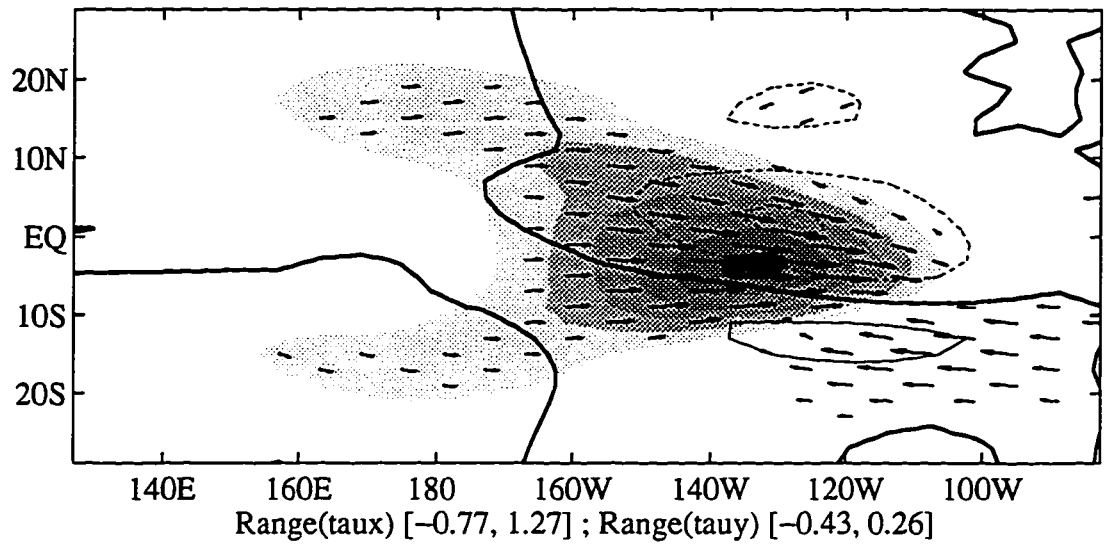

Figure 4.8 The immediate response of the atmosphere model in surface wind stress anomaly resulting from perturbing the SST with the 6-month optimal (shown in Fig. 4.2d) for the climatological October condition. Positive zonal wind stress anomalies are shaded dark (shading level is 0.2 m^2s^{-2} starting +0.2 m^2s^{-2}); meridional wind stress anomalies are contoured (contour interval is 0.2 m^2s^{-2}).

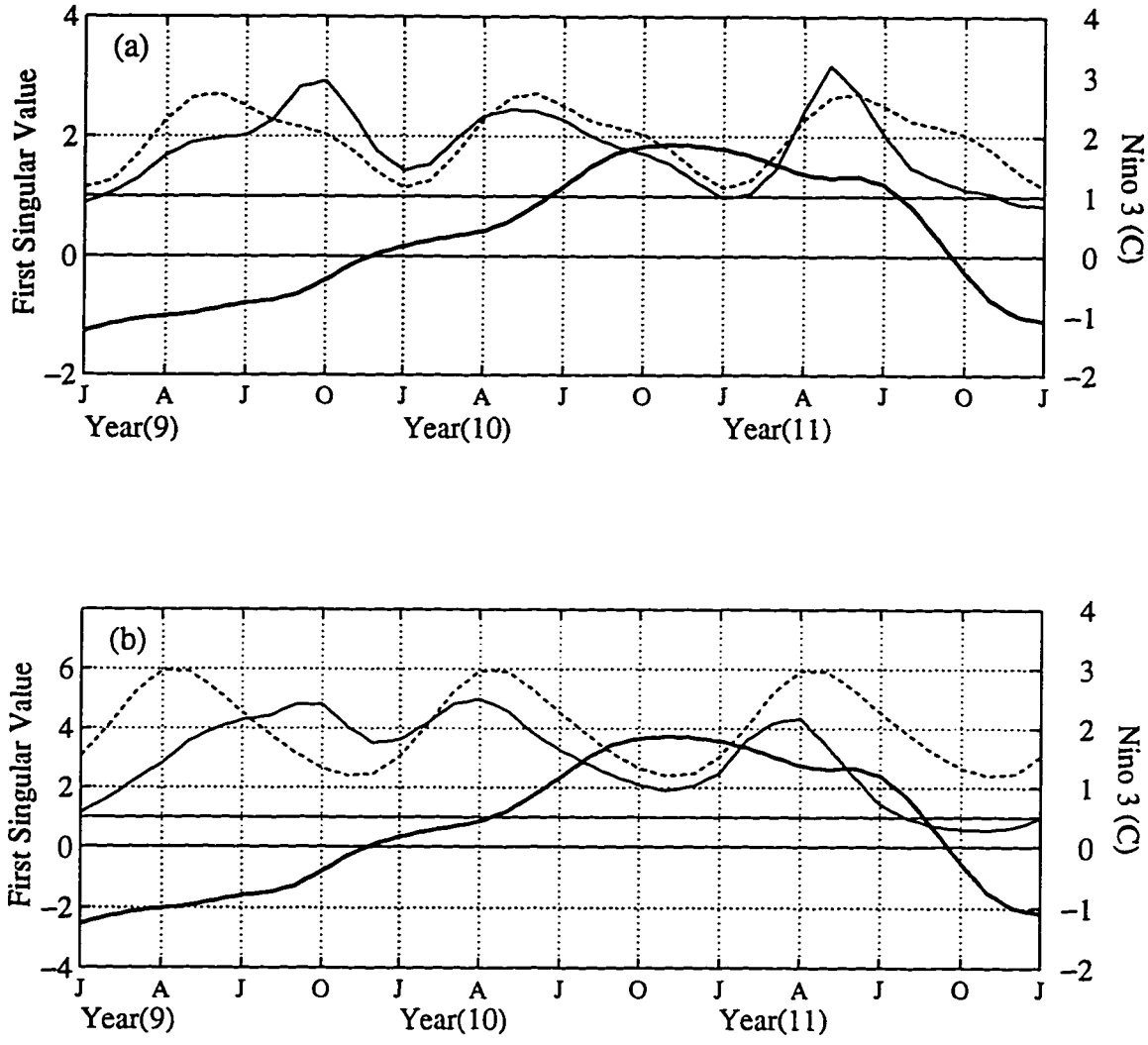

Figure 4.9 The first singular value (λ_1) about the climatological annual cycle reference trajectory (from Fig. 4.1, repeated cyclically, dashed line) are superposed on the maximum perturbation growth based on the freely evolving model ENSO trajectory (from Fig. 4.4, solid line): (a) 3-month and (b) 6-month integrations. The heavy line is the Niño 3 index.

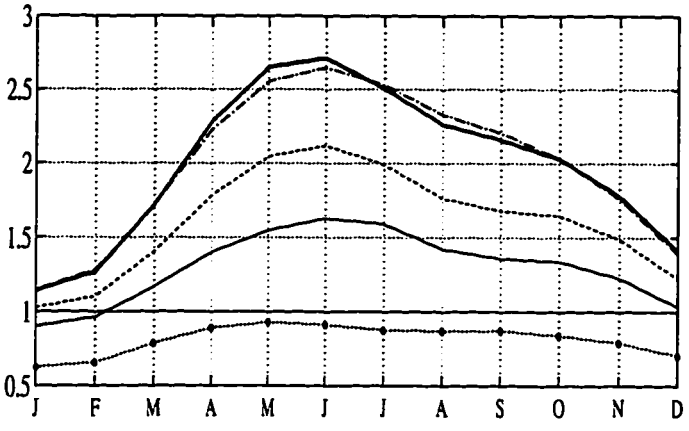

Figure 4.10 The first singular value (λ_1) for 3-month integrations performed on the annual cycle reference trajectory: standard full model (heavy solid line), no horizontal advection (solid), $\bar{v}_{sfc} = 0$ (dashed), $\bar{u}_{sfc} = 0$ (dash-dot) and no subsurface temperature anomalies, $T_s = 0$ (dotted).

CHAPTER 5 ENSO FORECAST SKILL AND OPTIMAL ERROR GROWTH

5.1 Introduction

To link our study to the forecast issue, we will evaluate the relationship between the skill of the short–term climate prediction and the fastest growing error in the coupled atmosphere–ocean model. We will focus our analysis on the six–month–lead forecast skill and the six–month optimal error growth to facilitate a comparison between the results discussed in this chapter and those presented in Chapter 4.

This chapter is outlined as follows. In section 5.2 we describe the initialization scheme and report the model nowcast skill in simulating the SST anomalies for the period 1967-1990. The model forecast skill for lead times from 0 to 12 months and the optimal error growth over six months are calculated for each month, starting in January 1961 and ending in December 1990. Section 5.3 examines the model forecast skill and section 5.4 presents the optimal error growth. The time series of the model forecast skill and the leading singular values are composited and presented as a function of the seasonal and the ENSO cycles, respectively. The model forecast skill and the optimal error growth are shown to be negatively correlated. Section 5.5 examines extreme cases in which this inverse relationship between the forecast skill and the optimal error growth breaks down. Results support the hypothesis that the growth of SST errors present in the initial conditions are responsible for a significant fraction of the poor SST forecasts made using this model. Finally, the discussion and conclusion are presented in sections 5.6 and 5.7.

5.2 Model Initialization and Nowcast Skill

5.2.1 Model initialization

An early initialization scheme for coupled model forecasts was developed by Cane *et al.* (1986). The initial conditions are generated by forcing the ocean component of the coupled model with the observed wind stress up to the forecast starting time. The ocean fields (ocean surface currents, upwelling, thermocline and SST fields) are stored in restart files. Using the restart files and the observed wind stress as the initial conditions, the coupled model then runs forward freely to make predictions. This (*old*) initialization scheme was subsequently shown to create a *shock* in the surface winds at the forecast initialization time that accounted for a significant fraction of the model forecast error (D. Chen *et al.* 1995).

D. Chen *et al.* (1995) developed a *new* initialization scheme which significantly improves the skill of the forecasts using the Zebiak and Cane model. In this new scheme, the coupled model is forced with a mixture of the model generated and the observed wind stress at each time step[1]. The mixture of the wind stress anomalies are:

$$\tau = \alpha\tau_o + (1-\alpha)\,\tau_m, \qquad \text{(EQ 5.1)}$$

where τ_o is the observed wind stress anomaly taken from the FSU (Florida State University) windstress product, and τ_m is the model generated wind stress anomaly, and the coefficient α is latitude (y)–dependent:

$$\alpha = \begin{cases} 0.25 & |y| = 1^\circ \\ 0.25 + (|y| - 1) \cdot 0.05 & |y| \le 7^\circ \\ 0.55 & |y| > 7^\circ \end{cases} . \qquad \text{(EQ 5.2)}$$

1. The model time step is 10 days.

This *nudged* wind stress and the model generated ocean fields are stored in restart files for further use. If α equals unity everywhere, $\tau = \tau_o$, and the old initialization scheme of Cane *et al.* (1986) is recovered. The new initialization scheme removes the initial shock of the coupled model due to the discontinuity in the surface winds that previously existed in the old initial conditions caused by switching from an ocean model in balance with purely observed to purely model generated surface winds.

5.2.2 Nowcast skill

Using the new initialization scheme, the coupled model is integrated from 1961 to 1990, creating restart files for each month. The model simulated the NINO1+2, NINO3 and NINO4[2] indices are compared against the observed as reported by the Climate Analysis Center (CAC) (see Fig. 5.1).

When compared with the nowcast using the old initialization scheme, the amplitude and the phasing of the warm events are close to the observed. The model nowcast using the new initialization scheme is significantly improved from that using the old initialization scheme. For example, over the 1967–90 period[3], the temporal correlation coefficient between the model simulated and the observed NINO3 is ~0.6 using the old initialization scheme (Fig. 2.2), and ~0.7 using the new initialization scheme (Fig. 5.1).

5.3 Six-Month Lead Forecast Skill Index: *FSI*

We take the monthly restart files from the integration described in section 5.2.2 as initial conditions for the coupled atmosphere–ocean model, from which the coupled model runs forward freely to make forecasts. A 12–month forecast is carried out starting every

2. NINO1+2, NINO3 and NINO4 refer to the area-averaged SST anomalies over the Niño 1+2 region [10°S to the equator and 6° offshore (to the equivalent of 87°W)], the Niño 3 region [5°S-5°N, 90°W-150°W], and the Niño 4 region [5°S-5°N, 150°W-160°E], which represent the equatorial coastal eastern Pacific, the eastern equatorial Pacific and the central equatorial Pacific, respectively.

3. Allowing 6 years of model spinning-up, we will only analyze the model output from 1967 to 1990.

month, using the January 1961 initial condition, the February 1961 initial condition, etc,..., up to the December 1990 initial conditions.

The correlation coefficient and the root–mean–square (rms) error between the model forecast and the observed data are the two most common indices in evaluating the skill of a forecast. In general, the correlation coefficient emphasizes the error in phasing, while the rms error emphasizes the error in amplitude. For convenience, we combine two statistics and define a *Forecast Skill Index* (*FSI*):

$$FSI = (cc_N - rms_N)_N,$$

where the subscript N refers to a *normalization*, such that the time series of the quantity has a zero mean and a standard deviation of one. The definition of *FSI* puts the same weight on both statistics, the correlation coefficient (*cc*) and the rms error (*rms*). Large positive *FSI* corresponds to a good forecast, and large negative *FSI* corresponds to a bad forecast.

5.3.1 Time series of *FSI* from 1967 to 1990

The model forecast skill at a six–month lead is evaluated using the pattern correlation coefficient, the rms error (in °C), and the relative rms (in standard deviation, see below) error over the equatorial Pacific region: 11°S–11°N along the equator. The pattern correlation coefficient and the rms error between the model forecast and the observed SST anomalies over the 11°S–11°N region is calculated with a point-by-point comparison. The relative rms error is defined as:

$$\sqrt{\frac{1}{N}\sum_{i=1}^{N}\left(\frac{T_{i,\,model} - T_{i,\,observed}}{\sigma_i}\right)^2}, \qquad \text{(EQ 5.3)}$$

i.e., the root-mean-square of the *error* that is normalized by the standard deviation. The index i indicates an individual grid point location, and N indicates the total number of grid points in the domain of interest. The standard deviation at each grid point used to normalize the error is calculated from the time series that are composed of the 24 elements (the

observed monthly SST anomalies at the model forecast verification time) over the 1967–90 record. That is, σ_i has a seasonal cycle.

The pattern correlation coefficient, the rms error and the relative rms error between the model forecast and the observed (COADS) SST anomalies over the 11°S–11°N band in the Pacific for the period of 1967–90 are shown in Fig. 5.2. During the ENSO events, the pattern correlation coefficient has higher values over an extended time, while the rms error -when it is large- is much more short–lived than the high value in the pattern correlation coefficient.

Fig. 5.3a plots the time series, from January of 1967 to December of 1990, of the normalized pattern correlation coefficient (cc_N) and the negative rms error ($-rms_N$) between the model forecast at a six–month lead time over the tropical Pacific 11° about the equator; superposed on which is the new index *FSI*. In most instances, the pattern correlation coefficient and the (relative) rms error between the model and the observed SST anomalies are inversely correlated (Fig. 5.3a): high correlation and small (relative) rms error indicates a high skill; low correlation and large (relative) rms error indicates a low skill. Notable exceptions include cases when the correlation is high but the rms error is very large (see Table 5.1) and cases when the correlation is very low but the rms error is also small (see Table 5.2).

Fig. 5.4 displays the forecast made in September of 1982, verified in March of 1983. The pattern correlation coefficient is very high, since the model forecasts the pattern accurately, but over-emphasizes the amplitudes, resulting in a large rms error. Fig. 5.5 on the other hand, shows the forecast made in August of 1978, verified in February of 1979. This is an example in which the model forecast is almost orthogonal to the observations, resulting in a very low pattern correlation coefficient. In addition, the amplitude of the difference between the model forecast and the observed data is very small.

TABLE 5.1 Six-month forecasts with high pattern correlation coefficient and large rms. These account for 4.2% of the forecasts (12 out of 288). Data in different years are separated by shadings.

Forecast Starting Time	CC	RMS	Relative RMS	*FSI*
October (68)	0.90	0.74	1.56	0.26
February (69)	0.67	0.75	1.13	0.00
May (72)	0.87	0.68	1.16	0.34
June (72)	0.89	0.70	1.13	0.33
July (72)	0.87	0.76	1.15	0.19
September (82)	0.92	0.71	1.56	0.33
March (83)	0.73	0.71	1.69	0.15
May (86)	0.72	0.82	1.18	-0.07
June (86)	0.73	0.83	1.10	-0.07
July (86)	0.78	0.78	1.06	0.06
August (86)	0.88	0.71	1.09	0.30
October (87)	0.77	0.67	2.04	0.25
Mean	**0.81**	**0.74**	**1.32**	**0.17**

Our new index *FSI* is shown to be a convenient index for the skill of the forecast that utilizes the spatial and the temporal information on the forecast error (i.e., the correlation coefficient and the rms error, see Fig. 5.3a). Fig. 5.3b plots the time series of *FSI* and the observed NINO3 for each forecast time (every month) from January 1967 to December 1990. There are five ENSO warm episodes in this period: the 1969–70, 1972–73, 1976–77, 1982–83 and the 1986–87 episodes. Notice that forecasts made prior and after the peak phase of ENSO are generally skillful ($FSI > 0.52$), while forecasts made starting at the peak phase of ENSO (e.g., summer 69, summer–winter 72, summer–winter 76, spring–summer 87) and forecasts starting 1-2 years before the peak phase of ENSO (e.g., spring 71, autumn 74–autumn 75, and summer–winter 85) have much larger error in them (see section 5.3.3). In the entire 30–year record from 1961–90, 63% of the cases have $FSI > 0$, 37% have $FSI < 0$; 30% have $FSI > (1-1/e = 0.63)$, and 23% $FSI < -(1-1/e)$.

TABLE 5.2 Six-month forecasts with low pattern correlation coefficient and small rms. These account for 4.2% of the forecasts (12 out of 288). Data in different years are separated by shadings.

Forecast Starting Time	CC	RMS	Relative RMS	*FSI*
February (68)	0.04	0.25	0.84	0.31
June (78)	-0.39	0.28	0.59	-0.18
July (78)	-0.24	0.17	0.54	0.19
August (78)	0.04	0.13	0.47	0.55
September (78)	-0.25	0.16	0.51	0.20
October (78)	-0.44	0.19	0.54	-0.06
November (78)	-0.35	0.20	0.56	0.02
February (80)	-0.34	0.30	0.56	-0.16
March (80)	-0.12	0.17	0.40	0.31
May (89)	-0.22	0.15	0.45	0.25
June (89)	0.25	0.10	0.33	0.81
August (89)	-0.02	0.23	0.52	0.29
Mean	**-0.17**	**0.19**	**0.53**	**0.21**

We now examine the model forecast skill over the 24–year period of 1967–90, presenting the *FSI* as a function of the annual cycle and the ENSO cycle. To examine the annual cycle dependence, we composite the 1967-90 time series of *FSI* based on the calendar months to obtain their seasonality (section 5.3.2). To examine the ENSO cycle dependence, we extract five ENSO events from this record and perform a four-year ENSO composite (section 5.3.3).

5.3.2 *FSI* as a function of the phase of the annual cycle

First, we examine the seasonality of the model forecast skill. Fig. 5.6 displays the pattern correlation coefficient and rms error between the model forecast and the observed SST anomalies between 11°S–11°N for lead times at 0 to 12 months. The twelve curves in Fig. 5.6a and Fig. 5.6c indicate the averages of the pattern correlation and rms error for the

forecasts made starting in the 24 Januaries (1967-90), 24 Februaries,..., and 24 Decembers, respectively. For example, the solid line in Fig. 5.6a starting with a value 0.23 at zero lead, has a value of 0.45 at nine month lead, which means that for the nine–month forecasts made in the January 67, January 77,..., January 90 (forecasting for October of the respective year), the average pattern correlation coefficient between the model forecast and the observed SST anomalies over 11°S–11°N is 0.45. The thick line indicates the grand mean over 1967–90 at the 0–12 month lead times. Fig. 5.6b and Fig. 5.6d are the equivalent contour plots. Each of the 12 curves in the left-column line-plots corresponds to one horizontal cross-section of the right-column contour-plots for 12–month forecasts made starting in January-December. On average, the pattern correlation coefficient is low (Fig. 5.6a–b), with a mean of the correlation coefficient at six–month lead of only 0.32.

The rms error for six–month forecasts made starting from June through November is larger than that for those forecasts made starting from December through May; the rms error for forecasts at lead times greater than eight months saturates and does not show a dependence on the forecast initialization month (Figs. 5.6c-d). The three areas of low correlation marked *I*, *II* and *III* in Fig. 5.6b correspond to the forecast verifying in late Northern winter–early spring, the time of year when the variance of SST anomalies in the equatorial region is the smallest. Hence, although the pattern coefficient indicates low skill at these times, the rms error is quite small (compare the shading areas in Fig. 5.6b and Fig. 5.6d).

NINO3 is the conventional index by which the community measures the ENSO forecast skill. The averaged seasonality of the model skill in forecasting NINO3 is displayed in Fig. 5.7, which shows the temporal correlation coefficient and the rms error of the 24–year time series of NINO3 for forecasts at the 1–month up to 12–month lead times. The model is shown to have *useful* skill. For the six–month forecasts, the averaged correlation coefficient between the model forecast and the observed NINO3 (which has a mean value of 0.64, see the thick solid line) is greater than persistence skill (0.45, see the thick dashed line), regardless of the forecast starting months (Fig. 5.7a). The average rms

error for the six–month forecasts is 0.86°C. Error saturation happens at forecast lead times longer than ~9 months (Fig. 5.7c).

It is interesting to note in Fig. 5.7b that forecasts made starting in February, March and April preserve a high correlation coefficient (~0.7) for up to 11 months, the correlation coefficient drops to ~0.5 for the 10-month lead time for forecasts made in September and October. These plots show that the forecasts made during Northern spring (February–May) have higher skill than forecasts starting from Northern autumn.

The pattern correlation coefficients between the model forecast and observed SST for the 11°S–11°N region (Fig. 5.6a) are much lower than the temporal correlation coefficient between the model forecast and the observed NINO3 (Fig. 5.7a). In general, the average over a domain of interest is easier to predict than the exact spatial pattern.

We show next the seasonality of model skill in NINO4, which represents the central equatorial Pacific. From Fig. 5.8a, the averaged correlation coefficient between the model forecast and the observed NINO4 for different starting months is low. The rms error indicates error saturation after only 3–4 months; the forecast skill for NINO4, unfortunately, fails to compete with persistence for lead times less than 6 months.

Coming back to the 11°S–11°N domain, Fig. 5.9 plots the annual cycle of the pattern correlation coefficient, the rms error and the relative rms error over the 11°S–11°N band in the Pacific. Specifically, the pattern correlation coefficients are highest for forecasts made starting from March and April and lowest when starting from July and November (Fig. 5.9a). The rms errors are lowest for forecasts initialized in February–March and largest for forecasts initialized in August–October (Fig. 5.9b-c).

We display in Fig. 5.10 the annual cycle of *FSI* (see the solid line; *SVI* will be discussed in section 5.4.2). It shows that the model has the highest skill for six–month forecasts initialized in February–April (forecasting for August–October), and the lowest skill for forecasts initialized in July–December, consistent with the skill plots in Figs. 5.6 - 5.7.

5.3.3 *FSI* as a function of the phase of the ENSO cycle

To examine the dependence of *FSI* on the phase of the ENSO cycle, we extract five ENSO episodes (1969–70, 1972–73, 1976–77, 1982–83 and 1986–87) and present the *FSI* for a four–year ENSO composite. The four–year composite is centered on warm (zeros) years. For example, for the 72–73 event, year(–1), year(–0), year(+0) and year(+1) refer to years 1971, 72, 73 and 74, respectively.

Fig. 5.11 displays the *FSI* and the observed NINO3 associated with the composite ENSO. (Also plotted in Fig. 5.11 is the composite *SVI*, which will be discussed in section 5.4.3.) The composite *FSI* varies with the annual cycle, e.g., the larger *FSI* is for forecasts made in February–April (Fig. 5.10). Forecasts made prior to December (–1) have the poorest skill and forecasts made around the composite peak phase also have low skill, e.g., August (–0) through September (+0). Forecasts made during the onset phase (February through July (–1)) are the most skillful and forecasts made during the cold phase (November (+0) to June (+1)) also have high skills.

5.4 Six-Month Optimal Error Growth: *SVI*

Recall from Chapter 3, the leading singular value is a measure of the maximum possible growth of errors in the initial conditions. Using the coupled model, we calculated the singular vectors and singular values over a six–month growth period starting from the January 1967 initial condition, from the February 1967 initial condition,..., and from the December 1990 initial condition[4]. We will next examine the optimal error growth over the 24–year period from 1967 to 1990 as a function of the annual cycle and of the ENSO cycle. To examine the annual cycle dependence, we composite the 1967-90 time series of the leading singular value based on the calendar months to obtain their seasonality (sec-

4. The initial conditions are the same as the restart files used to initialize the forecasts described in section 5.2.

tion 5.4.2). To examine the ENSO cycle dependence, we extract five ENSO events from this record and perform a four-year ENSO composite (section 5.4.3).

5.4.1 Time series of *SV1* from 1967 to 1990

Fig. 5.12 plots the time series of the leading singular value *SV1* (the optimal SST error growth) and the second singular value *SV2*. Also plotted for reference is the observed NINO3. The time axis indicates the integration starting time. If the singular value is greater than 1, the initial error can grow, but if *SV1* is less than 1, no SST error growth can occur. For most of the 288 forecasts, the optimal initial conditions and their patterns in the final state resemble that presented in Chapter 4. We plot in Fig. 5.13 the initial and final patterns of the first two singular vectors for an integration started in October 1982. The first singular vector (i.e., the optimal error), features an east–west dipole across the basin and the center of contours in the eastern equatorial Pacific is located a few degrees south of the equator (Fig. 5.13a). This optimal pattern develops into an ENSO–like pattern six months later as shown in Fig. 5.13b. This is a typical example in which only one singular vector grows and all others decay (Fig. 5.13c–d).

In this 24–year period, 17 occasions (5.9%) have no growing singular vectors at all (Table 5.3) and 4 occasions (1.4%) have two growing singular vectors (Table 5.4). We have never found three simultaneously growing singular vectors in this model. For all cases, *SV1* and *SV2* are very well separated, i.e., *SV1* is much greater than *SV2*.

TABLE 5.3 *SV1* and *SV2* for 17 six-month integrations during 1967–90 with no growing singular vectors. These account for 5.9% of the forecasts. Data in different years are separated by shadings.

Starting Time	*SV1*	*SV2*
January (67)	0.84	0.48
October (73)	0.91	0.36
November (73)	0.93	0.35
October (83)	0.99	0.74
November (83)	0.81	0.48
December (83)	0.69	0.57
January (84)	0.66	0.35
February (84)	0.79	0.49
March (84)	0.78	0.52
April (84)	0.92	0.56
October (87)	0.99	0.39
November (87)	0.87	0.55
December (87)	0.81	0.39
January (88)	0.72	0.38
February (88)	0.69	0.33
March (88)	0.83	0.50
April(88)	0.84	0.48
Mean	**0.83**	**0.47**

All of the 17 cases that have no growing singular vectors are instances where the integrations were initialized from October–April (see also Fig. 5.10). The initial and final state patterns of the leading singular vectors for six of these cases are plotted in Fig. 5.14 (cf. Fig. 4.2 and Fig. 4.5). We display in Fig. 5.15 the spatial patterns for 3 of the 4 cases with two growing singular vectors. The first singular vectors resemble those presented in Fig. 4.2 and Fig. 4.5; the final state of the first singular vector features the ENSO–like pattern. For most of the cases we analyzed, there is one highly dominant singular vector

in this model. Thus, although we found some cases with two growing singular modes, we will not put emphasis on the second mode here.

TABLE 5.4 *SV1* and *SV2* for four six-month integrations during 1967–90 with two growing singular vectors. These account for 1.4% of the forecasts. Data in different years are separated by shadings.

Starting Time	*SV1*	*SV2*
July (73)	1.57	1.31
March (76)	4.26	1.80
April (76)	5.12	1.42
August (87)	2.42	1.28
Mean	**3.34**	**1.45**

5.4.2 *SV1* as a function of the phase of the annual cycle

In this section we compare the annual cycle of *SV1* for the 1967-90 forecast trajectories, the annual cycle climatological trajectory, and the perpetual January (February, etc.) trajectories. The annual cycle of *SV1* for these three cases is shown in Fig. 5.16.

The six–month optimal error growth for integrations with starting months from May to September is large, while error growth for starts spanning the Northern winter (December to February) is much smaller (Fig. 5.10, the dashed line). Recall from Table 5.3 that all of the 6-month integrations with no growing singular vectors (*SV1* < 1) are integrations starting with the October–April conditions. This is consistent with the composite figure presented here; integrations beginning in this period are least unstable to initial error (for this model). The six–month optimal achieves peak values of *SV1* in Northern summer (*SV1* = 3.9 in July) and has low values in Northern winter (*SV1* = 2.4 in January), with an annual mean of 3.1.

This annual cycle in *SVI* for the forecast trajectory is phase-shifted 2 or 3 months toward the end of the calendar year compared to the *SVI* for the annual cycle trajectory (Fig. 5.16). For the idealized, annual cycle climatological reference trajectory (see section 4.3.1), the six–month optimal perturbation growth is achieved in the April–May starts (see the dashed line in Fig. 5.16). In the forecast mode, however, the optimal error growth is achieved for July starts (see the solid line in Fig. 5.16); see Chapter 6 for further discussion. The similarity of the two annual cycle *SVI*s can be understood by the following explanation. From the calculation of six–month optimal perturbation growth on the perpetual climatology trajectories, we found that the optimal growth is greatest for the July–August condition and smallest for the February–April condition (the dash-dot line). The model sensitivity to errors during the boreal winter is much less than that for boreal summer, consistent with the analysis presented in Battisti (1988) which showed that the boreal summer and fall is the most unstable time of the year (in the Battisti model). Hence, the optimal error growth over a six–month period will be greater if this period includes the Northern summer, and smaller otherwise. For example, the growth starting between December and next June is small while growth starting July through next January is large.

5.4.3 *SVI* as a function of the phase of the ENSO cycle

We compare in Fig. 5.11 the composite interannual *SVI* (defined in section 5.3.3 and hereafter *ISVI*; thin solid line) with the composite annual cycle *SVI* (defined in section 5.4.2 and hereafter *ASVI*; dotted line). We find that the *ISVI* is dominated by seasonal variability with some degree of modification by interannual variability. *ISVI* is greatest 1-2 years prior to the peak of ENSO and lowest one year after the peak of ENSO, which corresponds to a low and high *FSI* for these two periods of time respectively (see section 5.3.3).

In addition, for the major part of the ENSO event (from August (–0) through July (+1)), the *ISVI* is smaller than the *ASVI*, and during the year before the peak of ENSO

(prior to July (–0)) and after August (+1), the *ISVI* is greater than the *ASVI*. These results are consistent with the arguments presented in Chapter 4 (see also Chen *et al.* 1996) and are repeated here. In the central and eastern equatorial Pacific, change in upwelling due to change in the thermocline depth is the most prominent process for producing SST anomalies. During the warm phase of ENSO, the thermocline in the central and eastern equatorial Pacific is much deeper than normal and the system is therefore less sensitive to errors/perturbations at the initial time, i.e., *SVI* is smaller during the warm phase of ENSO. On the other hand, during the ENSO cold phase, the thermocline in the central and eastern equatorial Pacific is very close to the surface and the low *SVI* is due to nonlinear saturation in the formulation of the subsurface temperature.

5.5 Examination of the Relationship Between *FSI* and *SVI*

We have looked at the long time series of *FSI* (see section 5.3) and *SVI* (see section 5.4) and their composite annual cycle and ENSO cycle. Although from Fig. 5.10 we demonstrated that they are inversely related over the seasonal cycle, we also noted that this inverse relationship between *FSI* (Fig. 5.3b) and *SVI* (Fig. 5.12a) breaks down at times: a high *SVI* is not always accompanied by a low *FSI* and a low *SVI* is not always accompanied by a high *FSI*. Hence, further examination of their relationship, especially when the inverse relationship breaks down, is carried out through an analysis of sub-groups of the ensemble of monthly *FSI* and *SVI* pairs.

First we plot in Fig. 5.17 the normalized time series of the smoothed[5] *FSI* and *SVI*, both indices having a zero mean and a standard deviation of one. The observed NINO3 is superposed on the plot. Choosing a threshold value s, we define the four sub-groups by the following criteria:

5. A three–month running-mean is applied before the normalization.

- Group I (Fig. 5.17a): $SVI_N \geq s$ and $FSI_N \geq s$,
- Group II (Fig. 5.17b): $SVI_N \geq s$ and $FSI_N \leq -s$,
- Group III (Fig. 5.17c): $SVI_N \leq -s$ and $FSI_N \geq s$,
- Group IV (Fig. 5.17d): $SVI_N \leq -s$ and $FSI_N \leq -s$.

The distributions of the *FSI* and *SVI* for forecasts in these four groups are displayed in Fig. 5.18. There are 288 total cases in the 24–year time series (24x12=288). For a threshold[6] $s = 1 - e^{-1} \approx 0.63$, there are 152 cases (53%) with $|FSI_N|$ (i.e., the absolute value of FSI_N) greater than s, and there are 165 cases (57%) with $|SVI_N|$ (i.e., the absolute value of SVI_N) greater than s. We will only consider the extreme cases with both $|FSI_N|$ and $|SVI_N|$ greater than the threshold s. Other non-extreme cases will be ignored in this study.

Of the 92 cases in Groups I-IV, 64 cases fall in Groups II and III. Groups II and III together account for 22% of the total forecasts. Group II indicates cases in which low skill is accompanied by large sensitivity, and Group III is comprised of cases with high skill and low sensitivity. Thus, forecasts that comprise Groups II and III account for the strong negative correlation between the *FSI* and *SVI*. This relationship in Groups II and III is expected if the model forecast skill is indeed sensitive to errors in the initial conditions of SST and to the projection of the initial error in SST onto the first singular vector.

To assist understanding the details of the forecasts for the four groups, the following three figures are presented. For each forecast in each group, we project the error realized at the forecast initialization time, defined as the difference between the model nowcast and the COADS SST anomalies, upon the leading singular vector for the 11°S–11°N region. This projection is displayed in Fig. 5.19a. Fig. 5.19b displays the projection of the model 6-month forecast error upon the rescaled final pattern of the leading singular vector for each forecast in each group. The final pattern is rescaled such that the norm of

6. Since the normalized time series has a zero mean and a standard deviation of one, the threshold is chosen to be the typical e-folding cut-off, which roughly selects the upper and lower quartiles of *FSI* and *SVI*.

the rescaled final pattern of the optimal error is one. Fig. 5.20 plots the rms error in SST (a) at the forecast initialization time and (b) at the forecast verification time. In addition, the observed and the model forecast NINO3 for the 6-month lead at the forecast verification time is plotted in Fig. 5.21; also indicated on the plot by vertical lines are repeated from Fig. 5.17).

Group II (Fig. 5.17b): $SVI_N \geq s$ and $FSI_N \leq -s$

Group II includes 31 poor forecasts with high *SVI* (Fig. 5.17b, Fig. 5.18 and Fig. 5.21). These forecasts correspond to a high projection of the final state forecast error upon the final state of the optimal (Fig. 5.19b). The projection of the error at the initial time upon the initial pattern of the optimal is comparable to that in Group III (Fig. 5.19a), but large *SVI* (Fig. 5.18b) severely degrades the model forecasts.

Group III (Fig. 5.17c): $SVI_N \leq -s$ and $FSI_N \geq s$

Group III on the other hand, is comprised of 33 accurate forecasts with low *SVI* (Fig. 5.17c and Fig. 5.18). The final state error project weakly onto the final state of the optimal error (Fig. 5.19b) and the rms error of the forecast at the final time is small (Fig. 5.20b and Fig. 5.21c). The optimal growth is trivial due to small *SVI*.

Group I (Fig. 5.17a): $SVI_N \geq s$ and $FSI_N \geq s$

Group I includes 17 skillful forecasts but their corresponding *SVI* are very large. Some statistics of these 17 *fortunate* forecasts are listed in Table 5.5. Fig. 5.22a shows some of the individual maps of the model six-month forecast SST anomalies at the verification time, Fig. 5.22b shows the corresponding maps from COADS, and Fig. 5.22c plots the forecast error, i.e., the difference between the model forecast and COADS SST anomalies. The time indicated on the plots is the forecast initialization time. The model forecast SST anomalies resemble the spatial pattern of the observed to a fairly large extent, but the amplitude is not accurate.

TABLE 5.5 Some statistics for forecasts in Group I. Data in different years are separated by shadings.

Group I		*SVI*	*FSI*	CC	RMS	Relative RMS
1	May (69)	5.20	1.20	0.90	0.25	0.50
2	September (71)	4.79	0.91	0.76	0.33	0.79
3	October (71)	4.04	1.12	0.85	0.26	0.85
4	March (76)	4.26	1.03	0.79	0.28	0.94
5	April (76)	5.12	1.18	0.82	0.21	0.69
6	May (76)	5.58	0.98	0.81	0.31	0.58
7	June (76)	6.07	0.80	0.81	0.41	0.64
8	July (76)	5.78	0.73	0.83	0.45	0.65
9	May(77)	6.63	0.78	0.53	0.27	0.80
10	June (77)	7.80	0.94	0.66	0.25	0.69
11	March (79)	3.80	1.30	0.83	0.15	0.33
12	April (79)	7.15	1.21	0.80	0.19	0.38
13	May (79)	5.33	0.88	0.64	0.28	0.48
14	November (81)	4.71	0.76	0.50	0.26	0.92
15	December (81)	4.78	0.98	0.68	0.25	0.82
16	January (82)	4.13	1.08	0.79	0.25	0.79
17	July (82)	3.95	0.74	0.90	0.49	1.00
Mean		**5.24**	**0.98**	**0.76**	**0.29**	**0.70**

The projection of the forecast error (Fig. 5.22c) upon the final pattern of the optimal error is much smaller compared to the projections for forecasts in Group II and Group IV. The rms error for this group is relative small among the four groups (see Fig. 5.20a), but the projection of the initial error onto the initial pattern of the optimal error scatters over a wide range (Fig. 5.19a). The cases in Group I with small initial projection are expected to yield good forecasts. However, the majority of the forecasts in Group I have high initial projectibility and large *SVI*. Two possible reasons for why these forecasts were unexpectedly good are: *(i)* there is error in the COADS such that the true SSTA looks

more like the initialization analysis from the COADS, or *(ii)* the optimal error growth somehow compensates for error in the model physics.

Group IV (Fig. 5.17d): $SVI_N \leq -s$ and $FSI_N \leq -s$

Group IV contains 11 poor forecasts in which the corresponding *SVI* are small. Some statistics of these cases in Group IV are listed in Table 5.6.

TABLE 5.6 Some statistics for forecasts in Group IV. Data in different years are separated by shadings.

Group IV		*SVI*	*FSI*	CC	RMS	Relative RMS
1	November (73)	0.93	-0.41	-0.29	0.46	1.09
2	December (73)	1.17	-0.38	-0.27	0.44	1.02
3	April (83)	1.77	-0.57	0.48	0.95	1.84
4	January (86)	2.00	-1.88	-0.47	1.13	2.09
5	February (86)	1.70	-0.91	-0.10	0.93	1.69
6	March (86)	1.47	-0.45	0.32	0.81	1.37
7	May (87)	1.82	-1.44	-0.58	0.84	1.48
8	June (87)	1.48	-1.69	-0.62	0.95	1.58
9	July (87)	1.47	-1.57	-0.49	0.96	1.57
10	August (87)	2.42	-0.99	0.01	0.92	1.77
11	September (87)	1.11	-0.22	0.55	0.81	1.97
Mean		**1.58**	**-0.96**	**-0.11**	**0.84**	**1.59**

Notice the (relative) rms error is very large and the pattern correlation coefficient is very low. Fig. 5.23 plots the maps of (a) the model forecasts, (b) the COADS, and (c) the forecast error at the verification time. Again, the time indicated on the plots is the forecast initialization time. For all cases, the model greatly over-estimates the amplitude of the SST anomalies and the model forecast spatial structure is quite inaccurate. The projection of both the initial state and the final state error upon the optimal error is largest and

spreads over the widest range among all the cases (Fig. 5.19). Eight out of the 11 forecasts in this group have a very high projection of the forecast error onto the final pattern of the optimal error, while only three of these 11 forecasts have a very small projection (see Fig. 5.23). Thus, while the *SVI* in this group is small, the rms errors in the initial conditions and at the final time (Fig. 5.20 and Fig. 5.21d) are large. In short, cases in Group IV represent times that are relatively stable in the system, however, the forecasts are poor because the large error in initial conditions persists through the forecast. Poor forecasts in Group IV are therefore largely due to poor initializations of the model.

5.6 Discussion

One way to evaluate the forecast skill is to draw a time series of the observed data and put an error bar to indicate the observational uncertainty at each point. If the forecast lies within the error bar, a successful forecast is claimed; otherwise, it is a poor forecast. We now demonstrate this idea but with an extra twist. Fig. 5.24 plots the time series of the six-month-lead model forecast NINO3 at the verification time, enveloped by two curves representing the errors obtained over a six–month growth period starting with the first growing singular error vector in SST with a peak amplitude of 0.3°C that is comparable to the measurement error[7]. Also plotted in the thick line is the observed NINO3 for the time indicated, surrounded by two curves that are the observed NINO3 plus/minus 0.3°C, representing the observational uncertainties. *For 68% of the forecasts during the 1967–90 period, the observed NINO3 falls within the envelope of forecast SST anomalies bounded by the optimal (maximum possible) error growth. This implies that for these cases, the model forecast errors could be accounted for by initial errors in SST alone due to observational uncertainties*[8]. This percentage is considerable and alarming, indicating

7. The TOGA Advisory Panel has commented: "From the TOGA experience it is clear that high-quality (within 0.1°C) in situ observations must be made globally to produce a global SST field to the accuracy (within 0.3°C to 0.5°C) needed for TOGA and for future climate prediction research." (see also Reynolds and Smith 1993 for suggestions of a necessary spatial resolution of the in situ device in order to have an accurate data sampling.

that a higher accuracy in the initial SST field would lead to improved forecast skill using this atmosphere-ocean model. Forecasts of the demise of the warm ENSO in 1973, 1983, 1987 are unskillful (Fig. 5.24): the observed NINO3 is not within the optimal error envelope. It is interesting to note that the envelope at these times is relatively narrow, and these cases include all the cases in Group IV.

One important question to ask from this study is, how important it is to know the optimal error growth? How much of the forecast error is due to the optimal error growth in SST? Hence, we project the forecast error in SST on the final state of the singular vectors, i.e., expand the forecast error in terms of the (final state of the) singular vectors. Since the complete set of singular vectors is dominated by the leading singular vector, we keep only the leading term of the expansion. The ratio of the variance of the first term to the variance of the forecast error gives the portion of the variance in the forecast error explained by the optimal growth of the error in the initial SST. Fig. 5.25a displays the variance in the model forecast error at 6-month lead time for forecasts from 1967-90, and the variance of the error at the forecast verification time explained by the optimal error growth. Fig. 5.25b displays the percentage of the variance in the forecast error explained by the optimal error growth. Fig. 5.26 displays a scatter plot for the percentage of the variance in the forecast error explained by the optimal error growth (Fig. 5.25b) vs. the rms error at the forecast verification time. Note that the low percentages are mainly at times of low total error. *On average over the 24 years, the mean percentage of the variance in the forecast error for the 6-month lead explained by the optimal error growth (the growth by the leading singular vector) is 68%, assuming that the forecast error with the structure of the final pattern of the leading singular vector is resulted from the growth of the leading singular vector in SST in the initial conditions.* If we include the first five singular vectors, the total effect of the first five singular vectors can account for about 80% of the forecast error.

---

8. When we replace the maximum initial SST amplitude of 0.3°C with 0.2°C (0.1°C, 0.5°C), the percentage of forecasts that fall within the envelope is 50% (23%, 87%).

The above mentioned variance of the forecast error explained by the optimal error growth estimate an upper bond since the forecast error with a structure of the final state of the optimal error does not necessarily result from the optimal error in the initial SST: it may come from observational error or error in model physics. A better estimate of the importance of the optimal error growth to the forecast error is obtained as follows. We project the nowcast error on the optimal error in SST, i.e., expand the nowcast error in terms of the singular vectors and keep only the first term, since the first singular value is much greater than the higher-order singular values. This portion of the nowcast error grows over a 6-month period of time with an amplification equal to the leading singular value. The variance of the forecast error that results form this portion of the error in the nowcast is compared to the variance of forecast error that results from the remaining error in the nowcast for each forecast from 1967-90. *The percentage of the variance in the forecast error due to the growth of the optimal error in the nowcast is 42.6% over 1967-90.*

Analysis of *FSI* and *SVI* suggests that singular vector analysis provides very useful but incomplete information about the dependence of the model forecast skill on the optimal error growth in the coupled system. The error growth due to the optimal perturbations at the initial condition is indeed the main factor that degrades the forecasts made using the Battisti model.

Unfortunately, we have little information regarding the structure or the amplitude of the errors and uncertainties in the observations. We have assumed that in this study the observations are without error. For forecasts in Group II and Group III, the model forecast skill can be explained simply by the optimal error growth. For example, the forecasts in Group II have poor skills because the optimal error growth is large, and forecasts in Group III are successful because of small optimal error growth. For forecasts in Group I, the skill is high even in the presence of large optimal error growth because the initial nowcast error is small. Forecasts in Group IV, however, are poor even though the optimal error growth is small due to large nowcast error in the initialization. The insufficiency of information in the structure of the initial error causes a problem for further investigation. If the

error in initial conditions due to the observational uncertainties has a structure of the fastest growing error, it may amplify or compensate for the error growth estimated with the singular vector analysis, and the singular vector analysis will not be directly related to the model predictability.

Xue *et al.* (1997) in their study use singular vector analysis applied to a reduced ZC model to select the fastest growing error, which is measured using a norm defined as the initial error covariance. They carried out two sets of experiments, using the *old* (Cane *et al.* 1986) and the *new* coupled model (D. Chen *et al.* 1995) initialization schemes. Adopting the new initialization scheme significantly improves the model forecasts. Hence, the forecast with the new initialization is taken as the *true* solution. This approach avoids the difficulty that the initial errors are in fact unknown. Comparing the old initial condition with the new initial condition, they are able to identify that the difference fields in the old and new initial conditions account for much of the optimal error growth which seriously impairs the forecast.

5.7 Conclusion

In this chapter, we have examined the sensitivity of the Battisti coupled atmosphere–ocean model to errors in the tropical Pacific SST at the forecast initialization time over a domain of 11°S–11°N along the equator. We defined a useful new forecast skill index *FSI*, which takes into account both the pattern correlation coefficient and the rms error between the model forecast the observed SST anomalies. We examined the relationship between the model forecast skill (*FSI*) and the optimal error growth in SST (*SVI*) for the period of 1967-90; they are shown to be negatively correlated.

For most of the forecasts (267 out of 288) over the 1967-90 period, there is only one growing singular vector. The spatial pattern of the optimal is not sensitive to the initial conditions experienced over this 24-year period. The growth, however, is strongly dependent on the seasonal cycle and is also modified by the interannual variability.

Two sets of composite analyses are performed to examine the relationship between the model forecast skill and the optimal error growth as a function of the phase of the annual cycle and the phase of the interannual ENSO cycle. Results show that, on average, at the six–month lead, the model skill is highest for forecasts initialized in February–April, and lowest for forecasts starting in the Northern summer. The composite ENSO analysis demonstrates that there is high skill for six–month forecasts made during the onset phase and the post-warm cold phase; skill is low for forecasts made during the peak phase, implying that the model fails to forecast the accurate timing of the shut–down of ENSO (see Fig. 5.1).

The optimal error growth is largest for six–month integrations starting June–August and lowest starting December–February. The optimal error is greatest 1-2 years prior to the peak of ENSO and lowest one year after the peak of ENSO, which corresponds well to the composite ENSO *FSI* in which the lowest value is achieved 1-2 years prior to the peak phase of ENSO and high values are found for the post-warm cold phase.

For the period 1967-90, the average of the *SVI* for the 6-month integrations is 3.1. This value is comparable to the mean of the six-month optimal perturbation growth about the idealized ENSO–on–annual–cycle reference trajectory (2.9) (see Fig. 4.4), and is somewhat smaller than the mean value of the six–month optimal perturbation growth about the idealized annual–cycle–only trajectory (4.0) (see Fig. 4.1 or Fig. 5.16). This supports the argument presented in section 4.4 that the interannual variability acts to suppress the instability due to annual variability alone.

By employing the singular vector analysis to analyze the model forecast error, we demonstrate that a large portion of errors of the forecasts can be accounted for by the growth of the initial errors in the tropical Pacific SST – errors that are within the observational uncertainties. This speaks strongly to the need for more accurate observations of SST for successful forecasts of the state of the tropical Pacific climate system.

Many studies have reported evidence of the decadal climate variability in SST and other fields. In Chapter 6, we will further investigate the decadal variability of the *FSI* and *SVI* using the 24-year time series obtained from this chapter. We will show that the model forecast skill and the optimal error growth are markedly different throughout different decades.

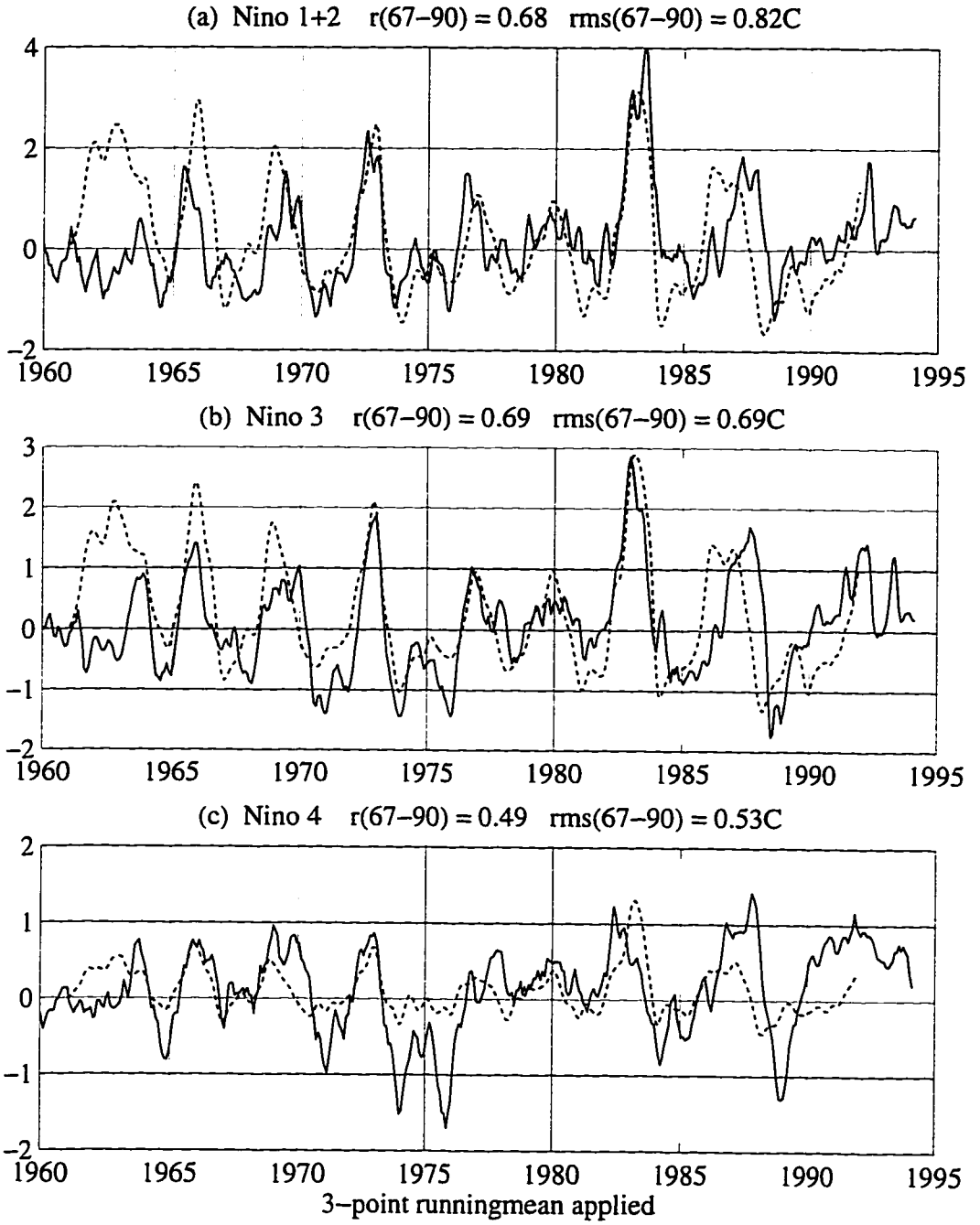

Figure 5.1 Time series of the observed (data from CAC, solid line) and model nowcast (with D. Chen *et al.* (1995) new initialization scheme, dashed line) Niño indices: the SST anomalies in the (a) Niño 1+2 (NINO1+2), (b) Niño 3 (NINO3) and (c) Niño 4 regions (NINO4). The observation is from 1960 to 1993, and the model nowcast is from 1961 to 1991. Tick marks are for Januaries of every five years. A three-point running-mean is applied to all curves. The temporal correlation coefficient and the rms error between the observation and the model simulation over 1967–1990 are noted on the top of each panel.

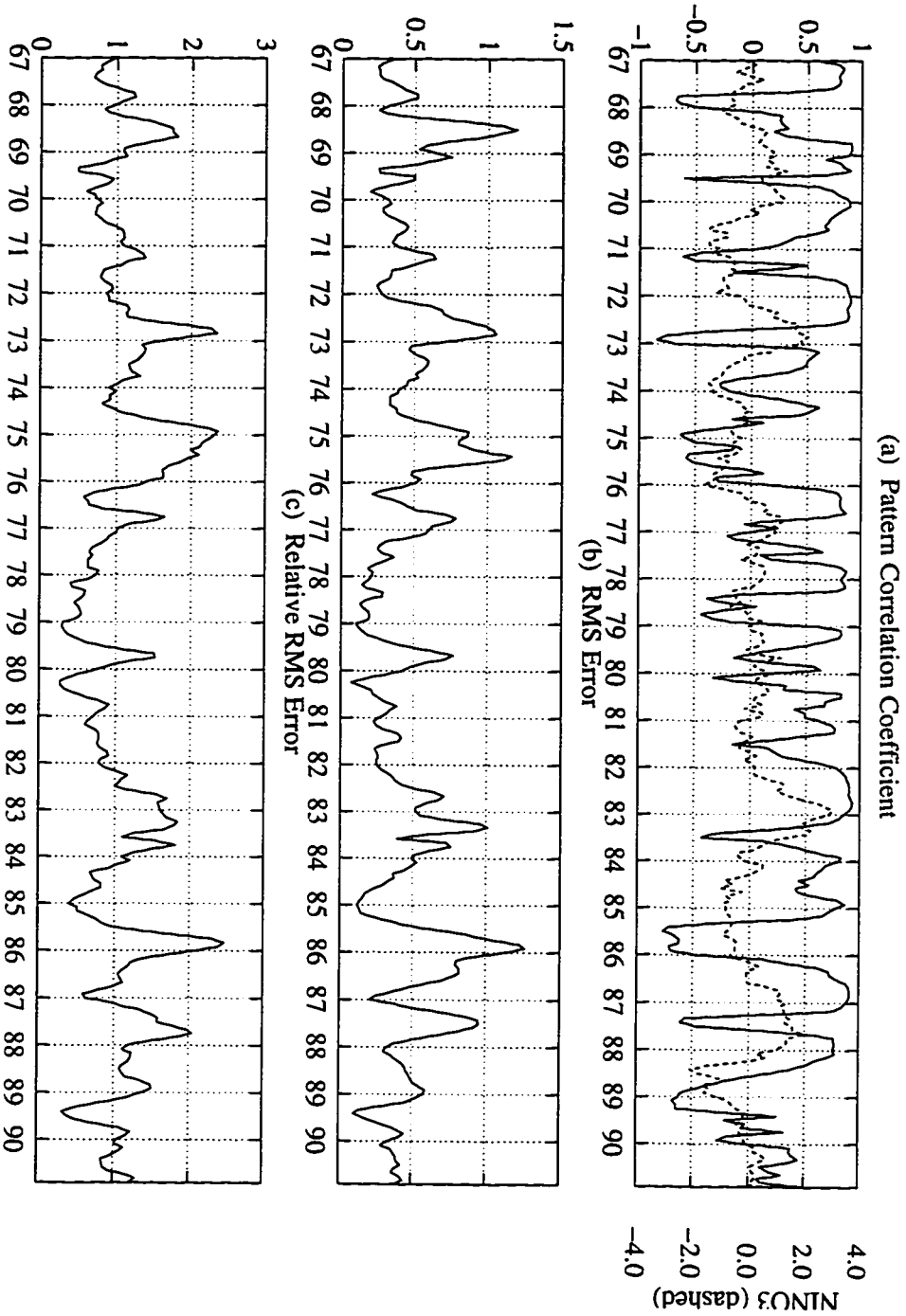

Figure 5.2 Model forecast skill at a six month lead time over the 11°S–11°N band in the equatorial Pacific, showing (a) pattern (point-by-point) correlation coefficient, (b) the rms error (in °C), and (c) the relative rms error (in standard deviation of the observation at the forecast verification time within the same domain). The time axis indicates the forecast initialization time. The dashed line plotted in panel (a) is the observed NINO3. Tick-marks are on the January of each year from 1967-1990.

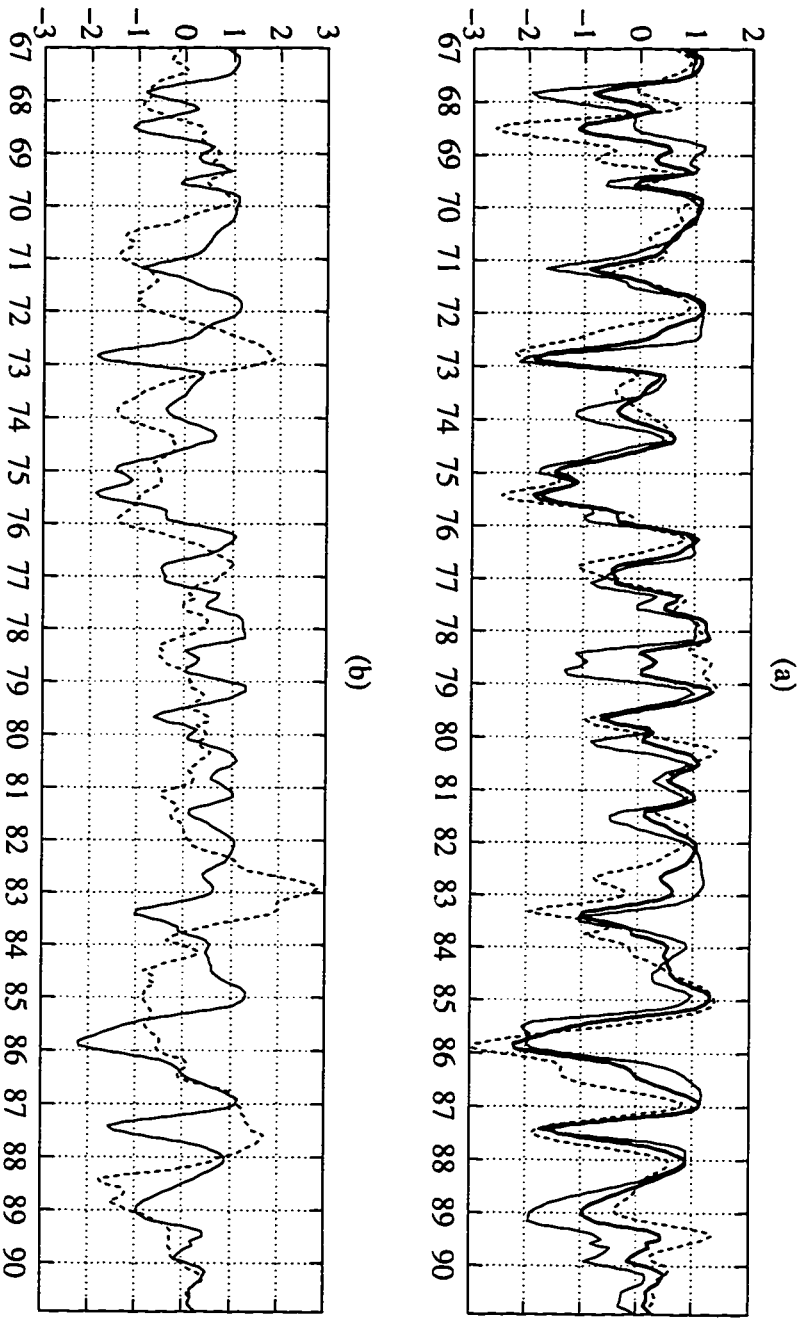

Figure 5.3 (a) The normalized time series of the correlation (solid) and the negative of the rms error (dashed) between the six–month-lead model forecast and the observed SST anomalies over the 11°S–11°N band in the equatorial Pacific. Superposed in thick line is the forecast skill index, *FSI*; see text for definition. (b) The *FSI* (solid) starting January 1961 to December 1990. The dashed line is the observed NINO3 (data from CAC). A three–month running-mean is applied to the curves. The time axis indicates the forecast starting time, and the ticks mark the January of each year.

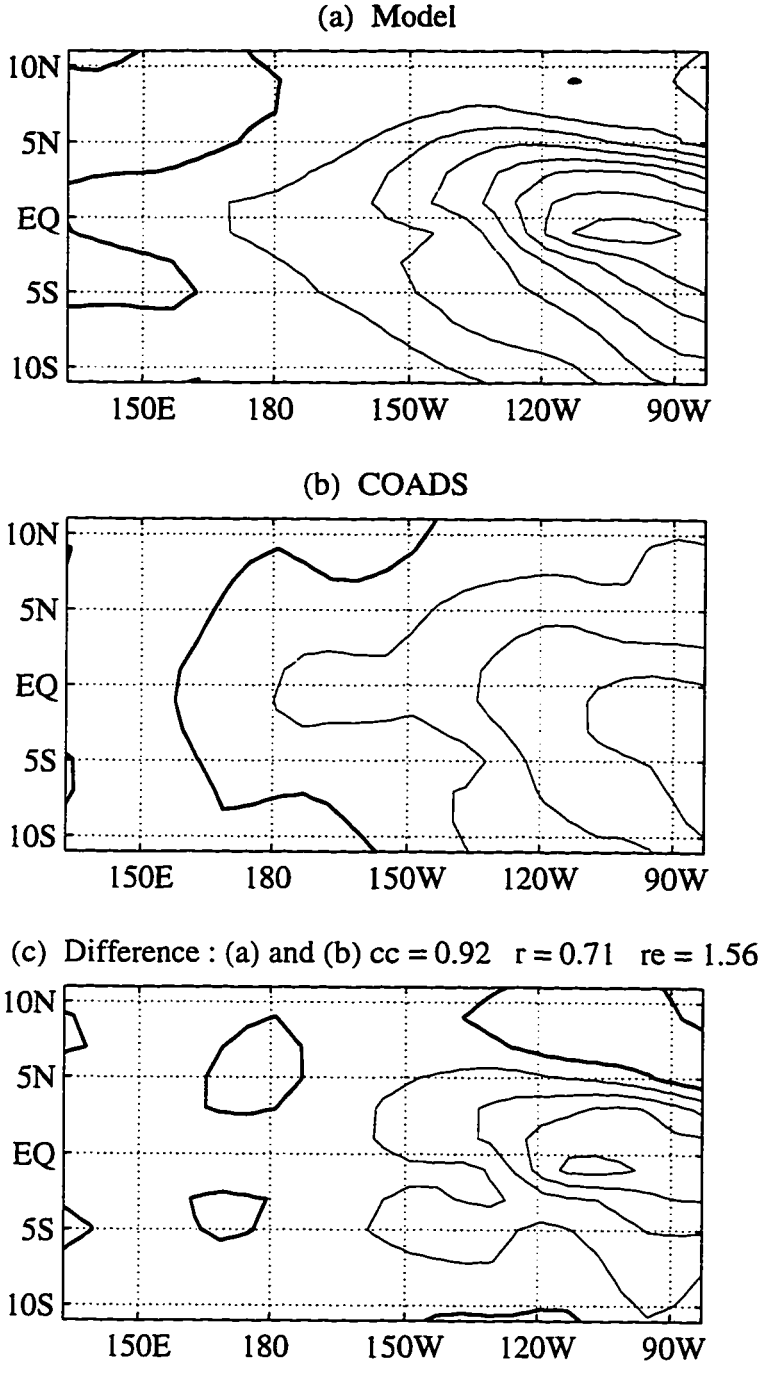

Figure 5.4 (a) Model forecast SST anomalies for March of 1983, i.e., forecast made starting in September 1982. (b) COADS SST anomalies at the verification time, March of 1983. (c) The difference map. The pattern (point-by-point) correlation coefficient within the 11°S–11°N equatorial Pacific (cc), the rms error (r), and the relative rms error (re) over the same domain are printed. The contour interval is 0.6°C. A 1-2-1 filter in the zonal direction is applied to all three plots.

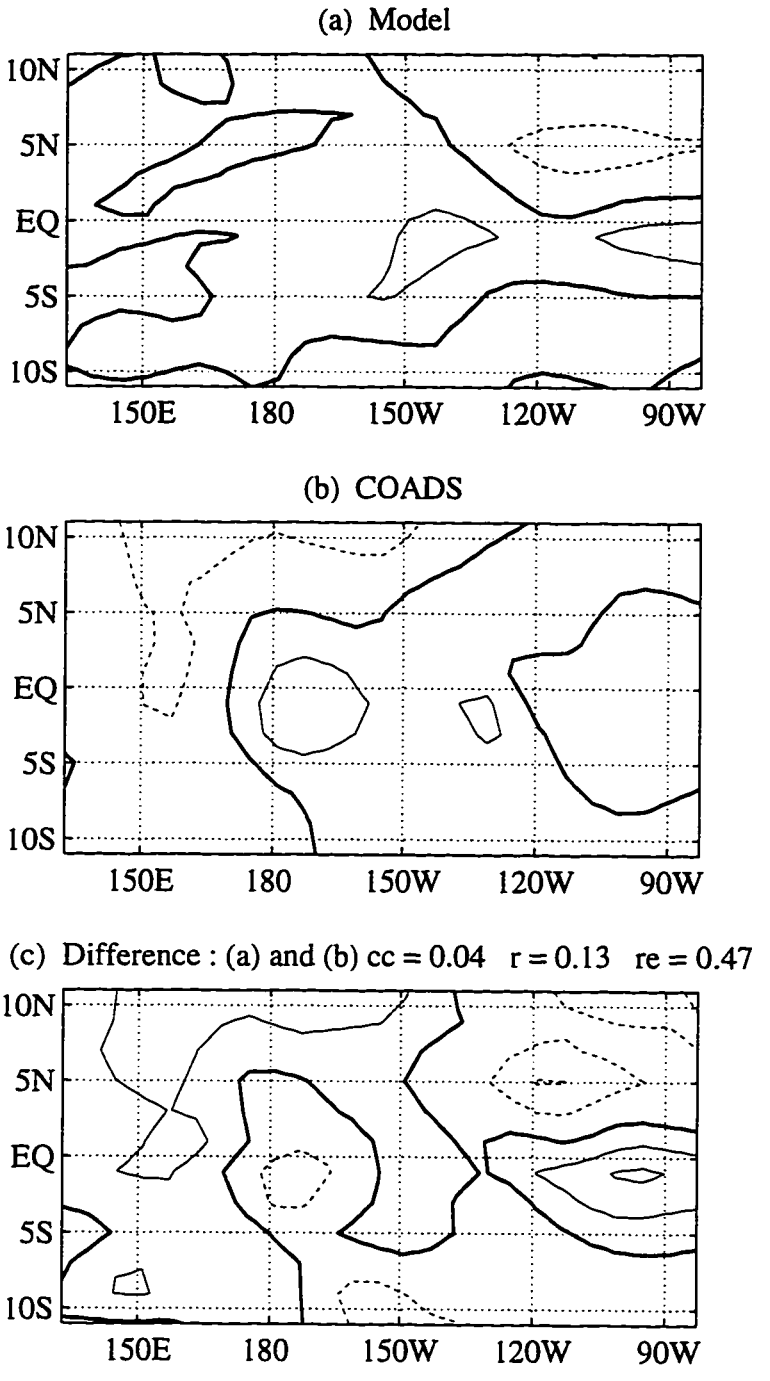

Figure 5.5 Same as Fig. 5.4, but for six–month forecast made starting in August of 1978, verified in February of 1979. The contour interval is 0.15°C.

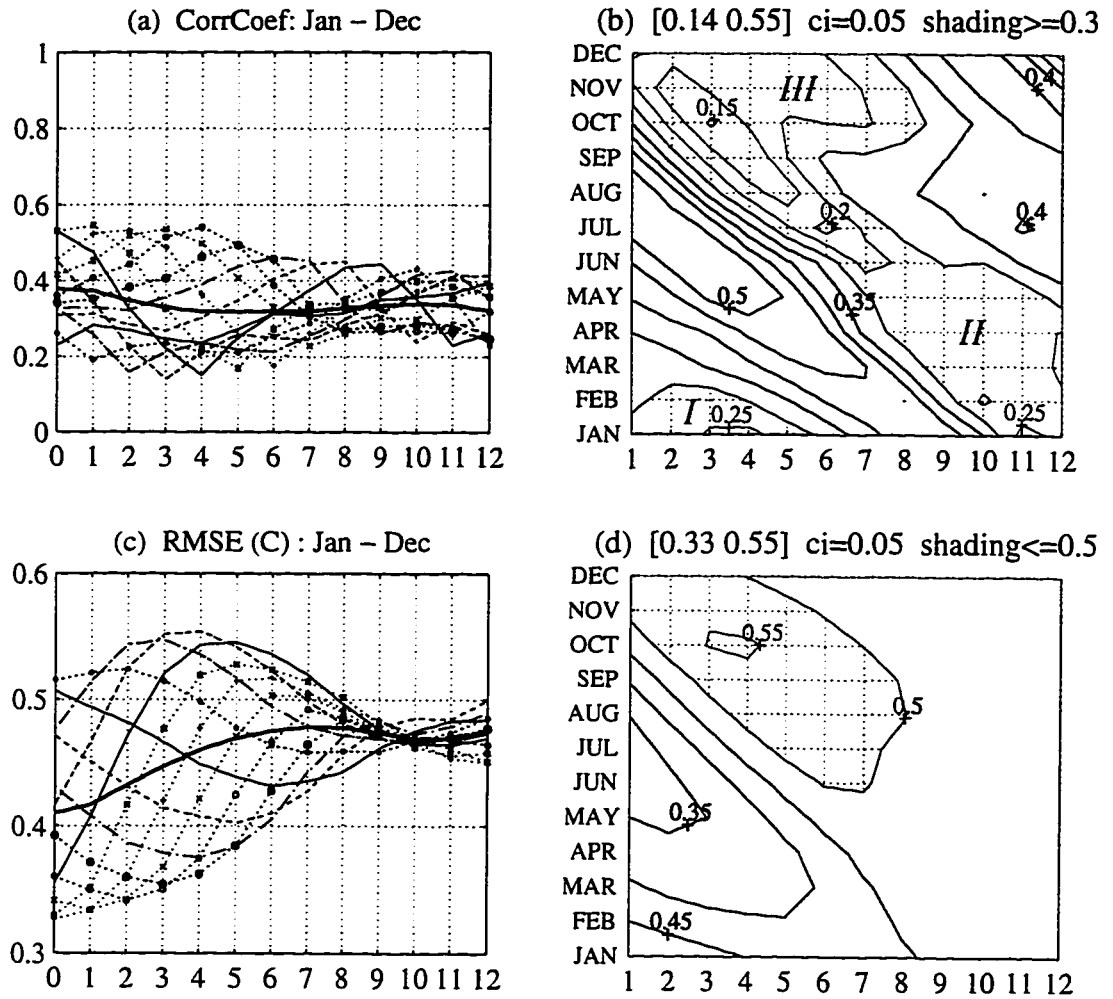

Figure 5.6 The seasonality of the model skill in forecasts of SST anomalies over the 11°S–11°N band along the equator averaged over the period of 1967-90. (a–b) The pattern correlation coefficient, and (c–d) the rms error between the model forecast and the observed SST anomalies from COADS over the 11°S–11°N along the equator. The left column figures are line plots; each plot includes twelve curves: one curve for the average January starts, one curve for the average of February starts, etc. The thick solid line is the grand mean of the correlation coefficient for lead times 0 up to 12–months. The right column figures are the equivalent contour plots, starting January to December for one–month forecast to twelve–month forecast lead times. The contour interval and the shading level are printed as reference.

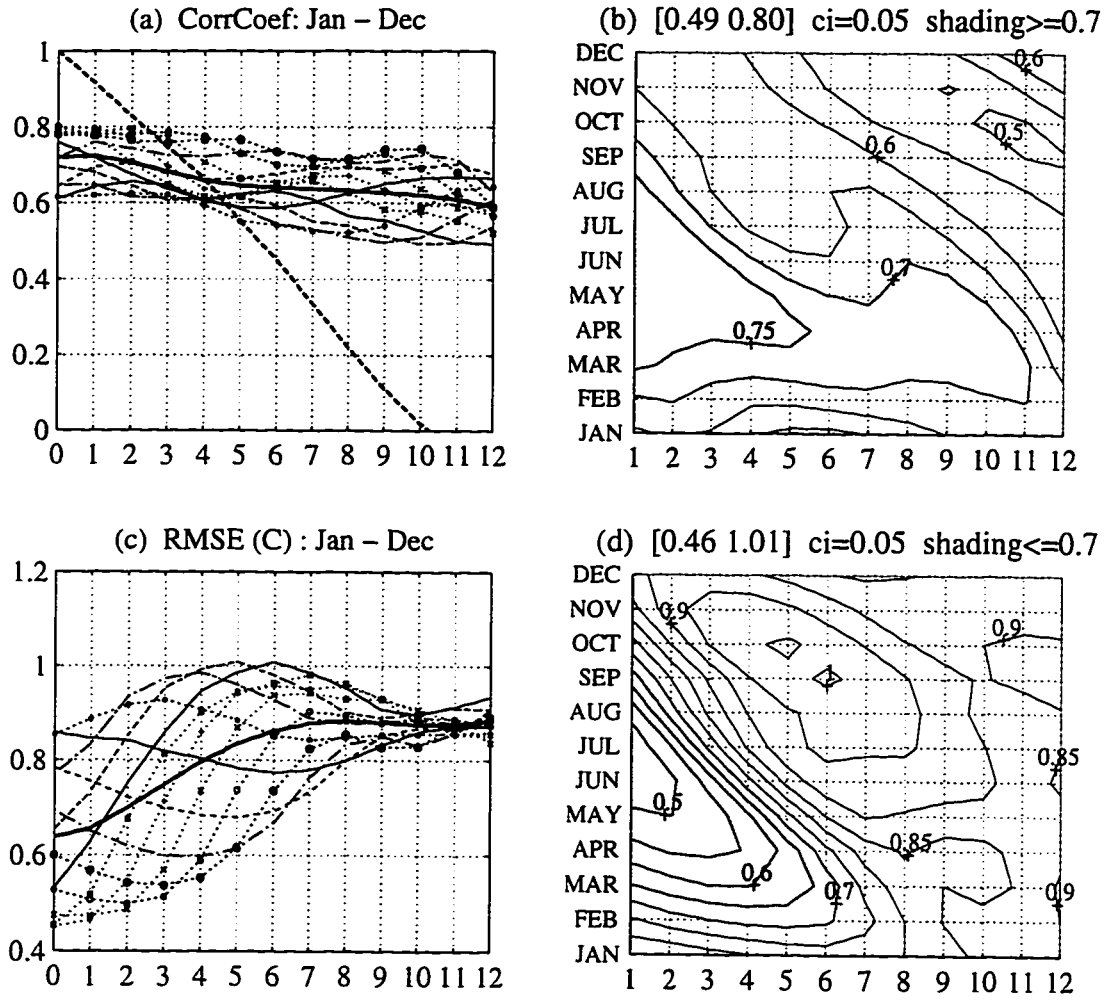

Figure 5.7 Same as in Fig. 5.6, but for the seasonality of the forecast skill in NINO3 averaged over the period of 1967-90: the temporal correlation coefficient and rms error between the model forecast and the observed time series in the SST anomalies averaged over the Niño 3 region. Observed NINO3 is data from CAC. The persistence skill in NINO3 is plotted in thick dashed line in (a).

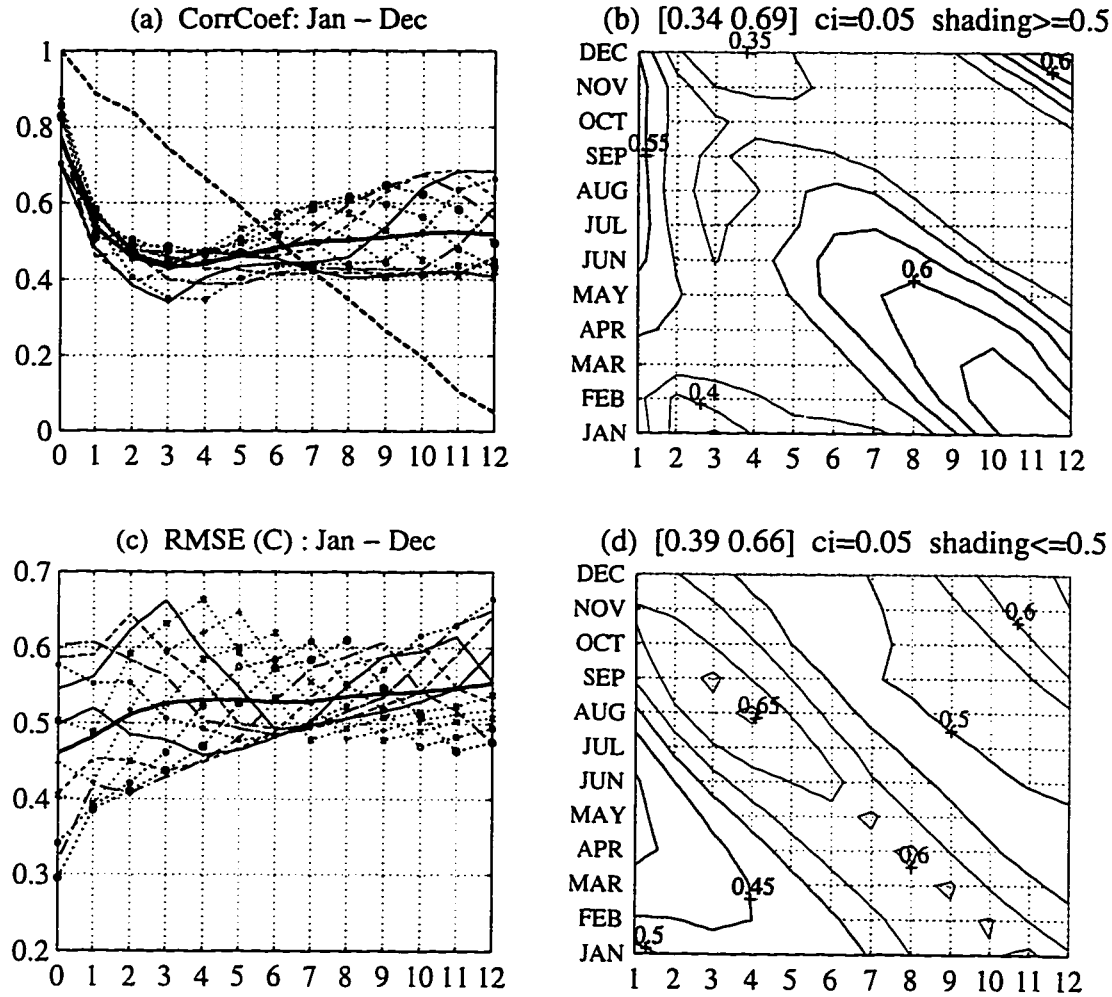

Figure 5.8 Same as in Fig. 5.7, but for the forecast skill in NINO4. Observed NINO4 is data from CAC. The persistence skill in NINO4 is plotted in thick dashed line in (a).

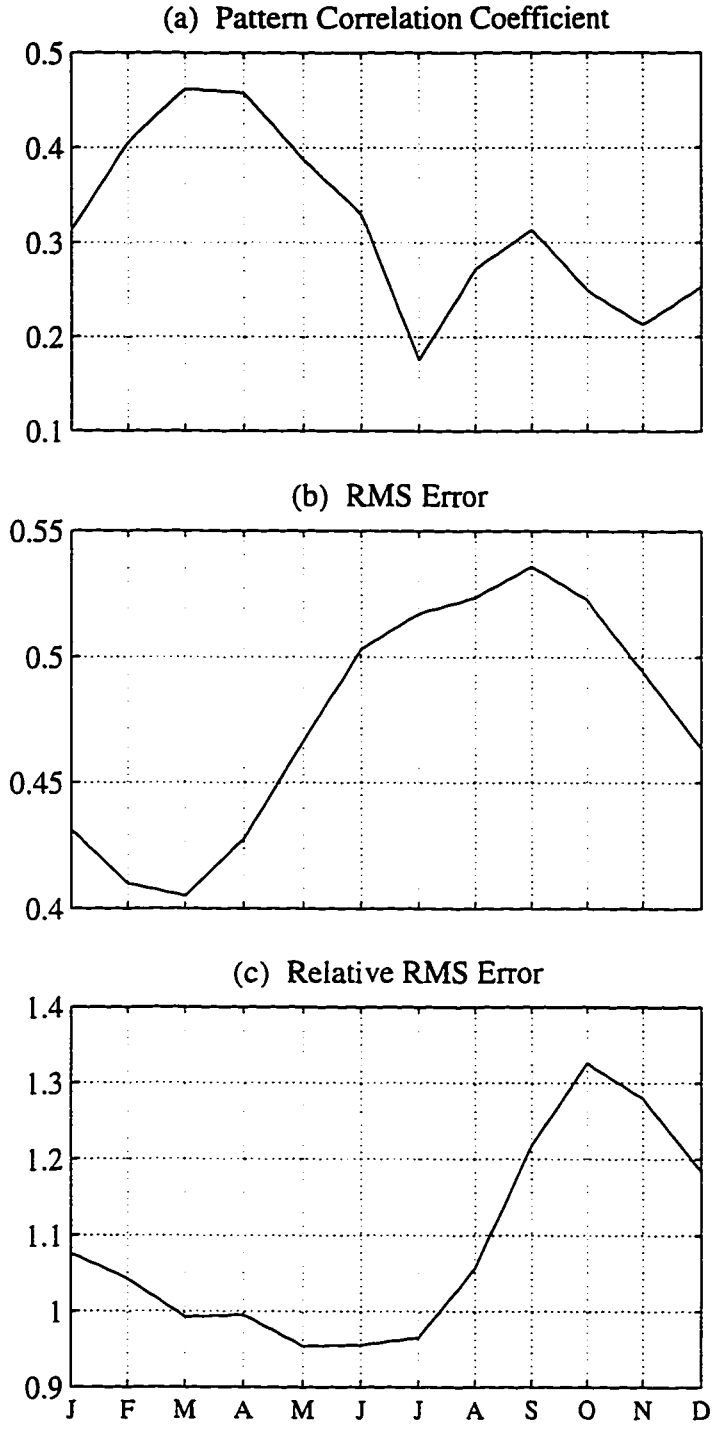

Figure 5.9 The annual–cycle composite of the 6-month lead model forecast skill, starting January 1967–December 1990: (a) the pattern correlation coefficient, (b) the rms error and (c) the relative rms error, over the region of 11°S–11°N in the Pacific. The time axis indicates the 6–month forecast starting month.

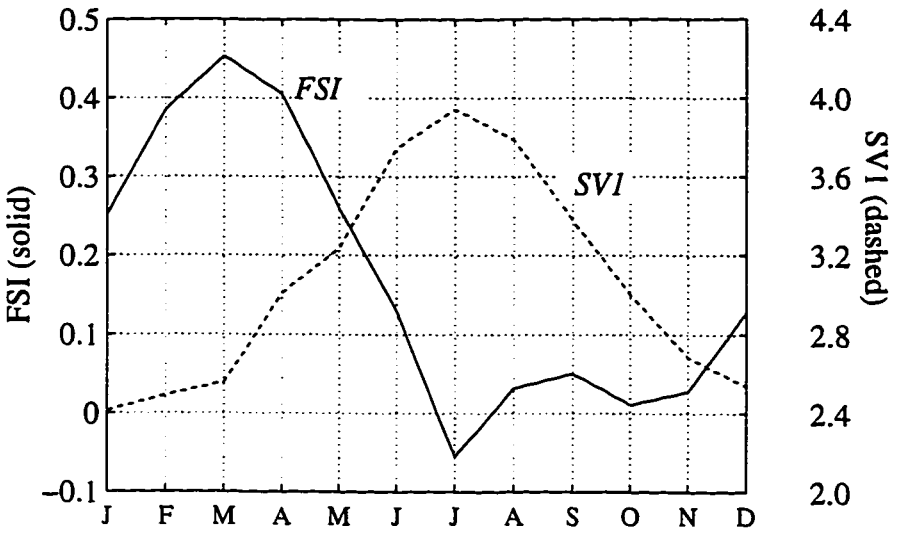

Figure 5.10 The annual–cycle composite of *FSI* (solid line, see discussion in section5.3) and *SVI* (dashed line, see discussion in section 5.4) using data for integrations starting January 1967–December 1990. The time axis indicates the starting month of the 6–month forecast/integration.

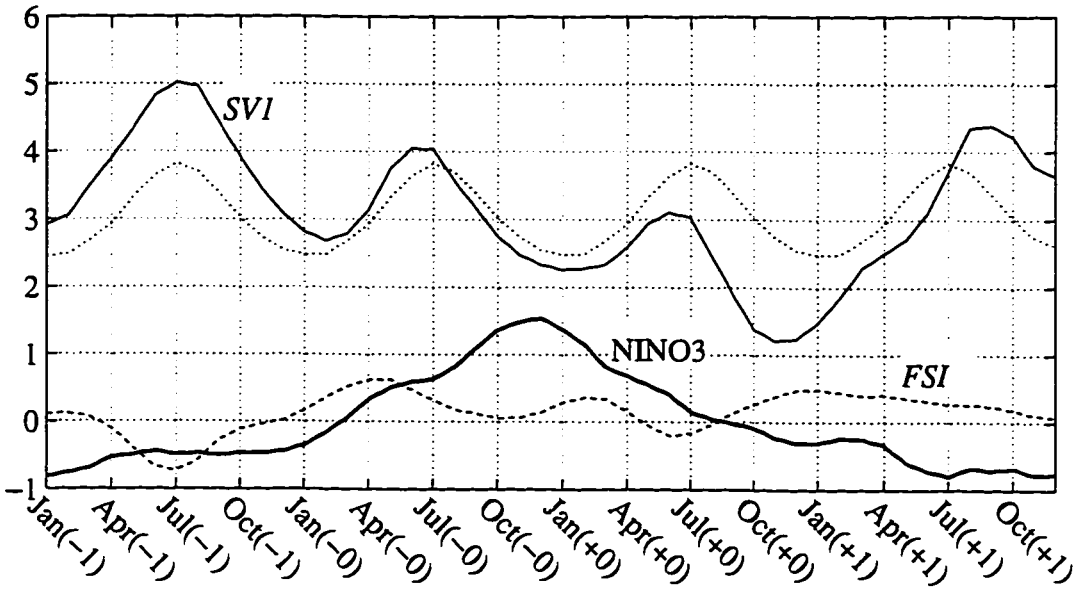

Figure 5.11 The four–year composite for *SVI* (thin solid), *FSI* (dashed). Superposed is the composite from the observed NINO3 (in °C, data from CAC, the thick solid line), and the repeated annual–cycle *SVI* (dotted). The five ENSO events that go into the composite are the 69–70, 72–73, 76–77, 82–83 and the 86–87 episodes. A three–month running-mean is applied to all curves.

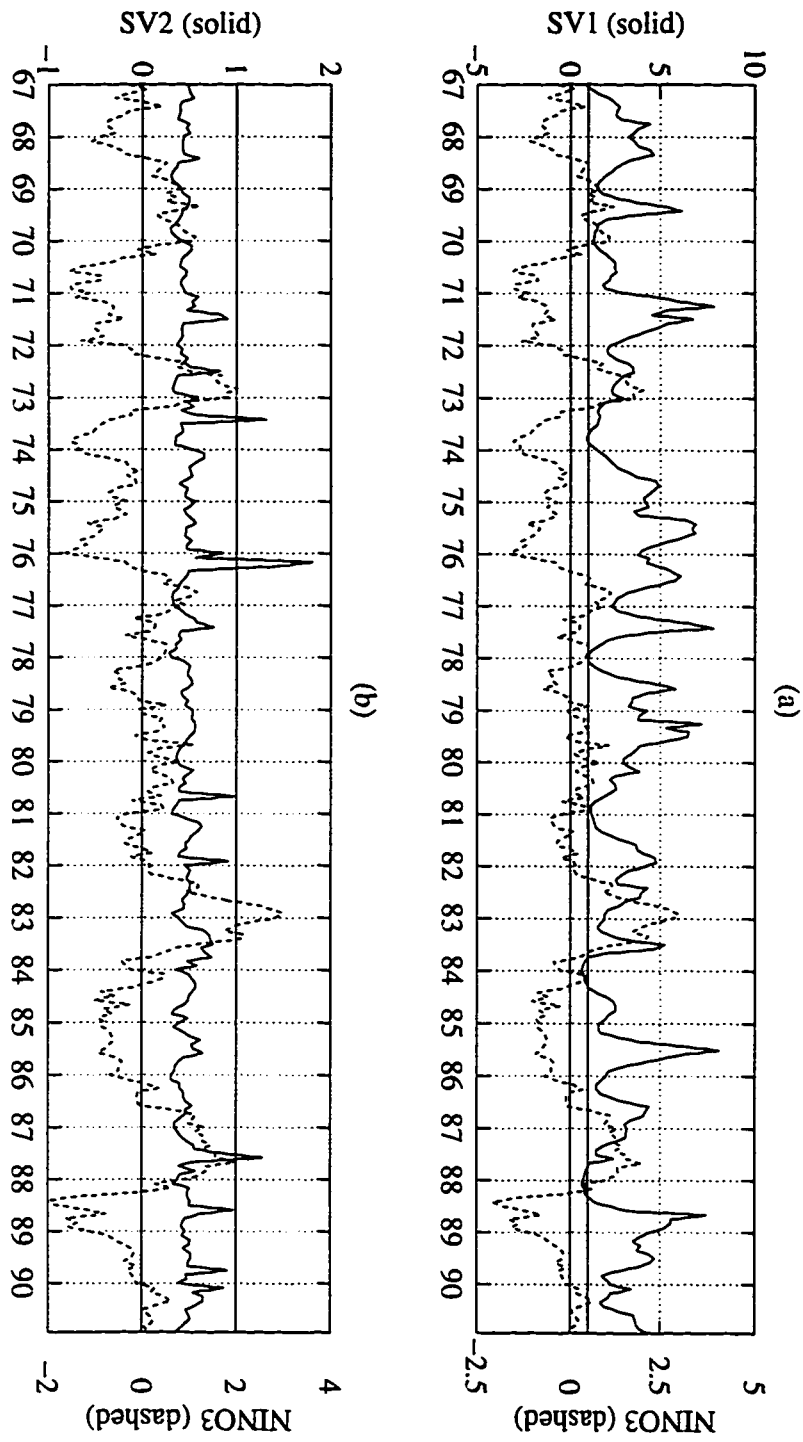

Figure 5.12 (a) The first (*SV1*) and (b) the second (*SV2*) singular values (solid line) for six–month integrations starting with the January 1967 initial condition to the December 1990 initial condition. Also plotted as reference is the observed NINO3 (dashed line).

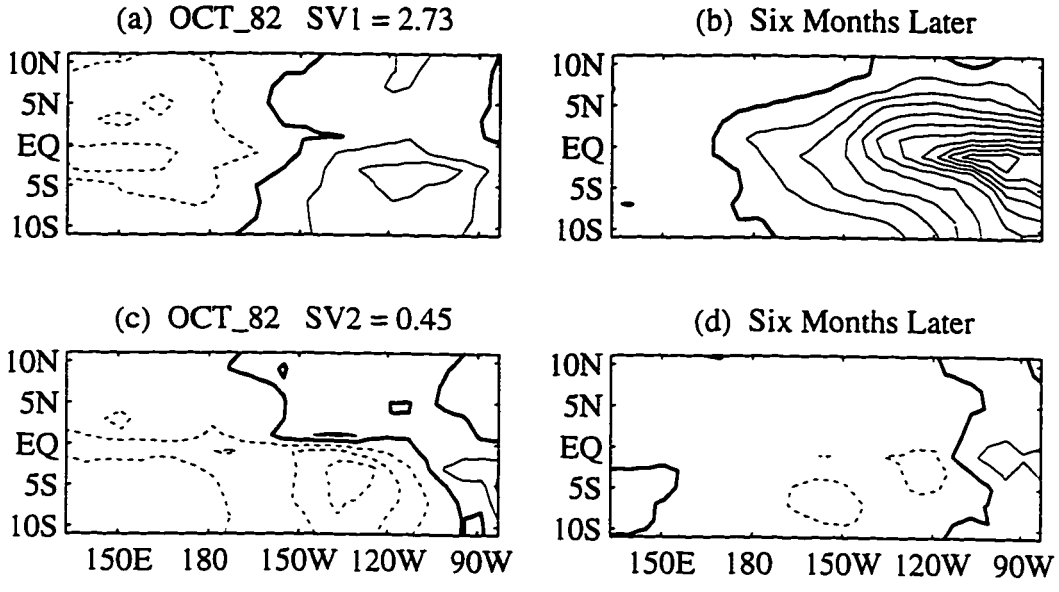

Figure 5.13 The first singular vector at (a) the initial time: October 1982, and (b) the final time: April 1983; The second singular vector at (c) the initial time, and (d) the final time. The contour interval is 0.05°C.

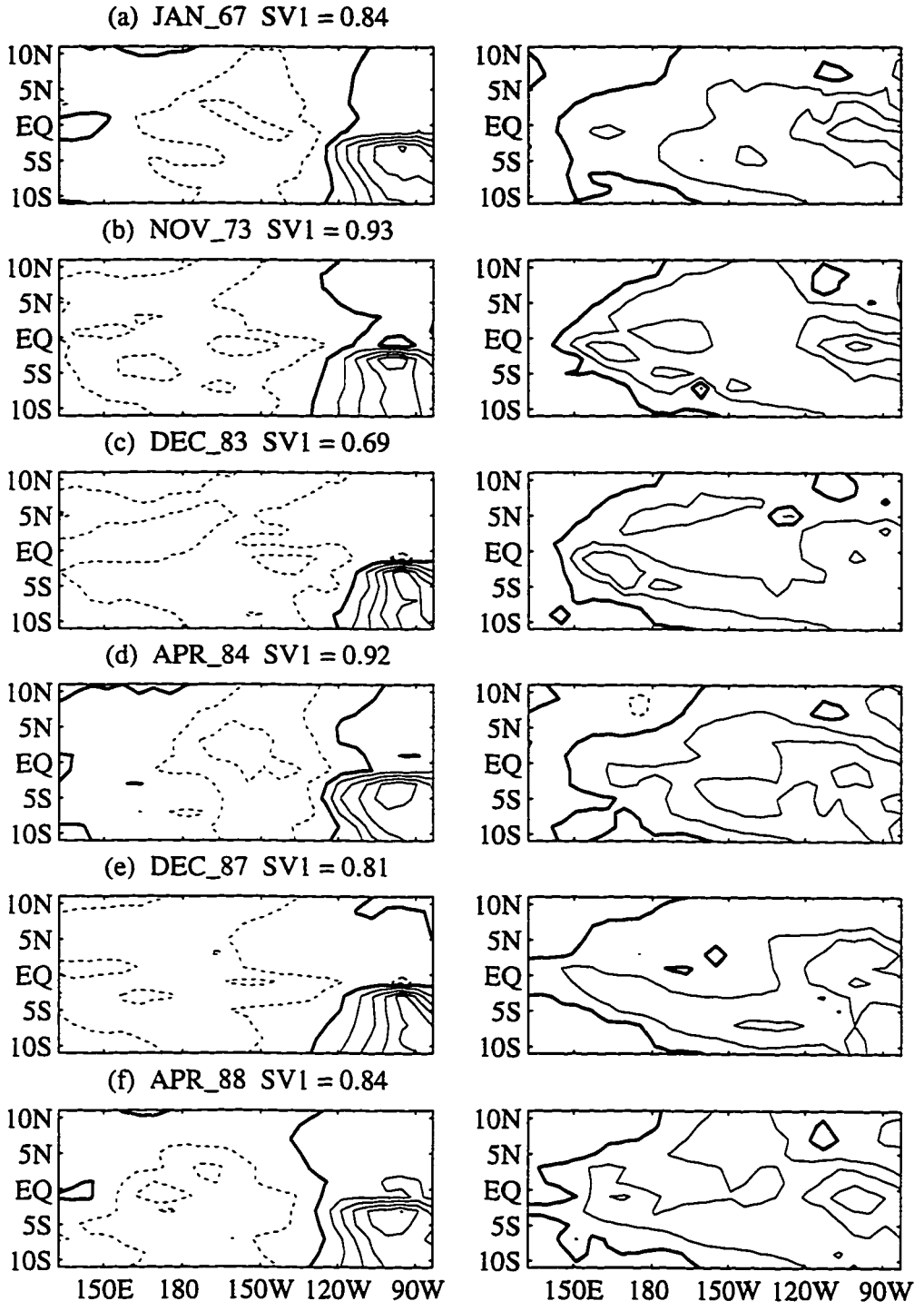

Figure 5.14 The initial (left column) and the final (right column) patterns of the first singular vector for six examples in which no growing singular vectors are found: (a) January 67, (b) October 83, (c) January 84, (d) April 84, (e) December 87, (f) March 88.

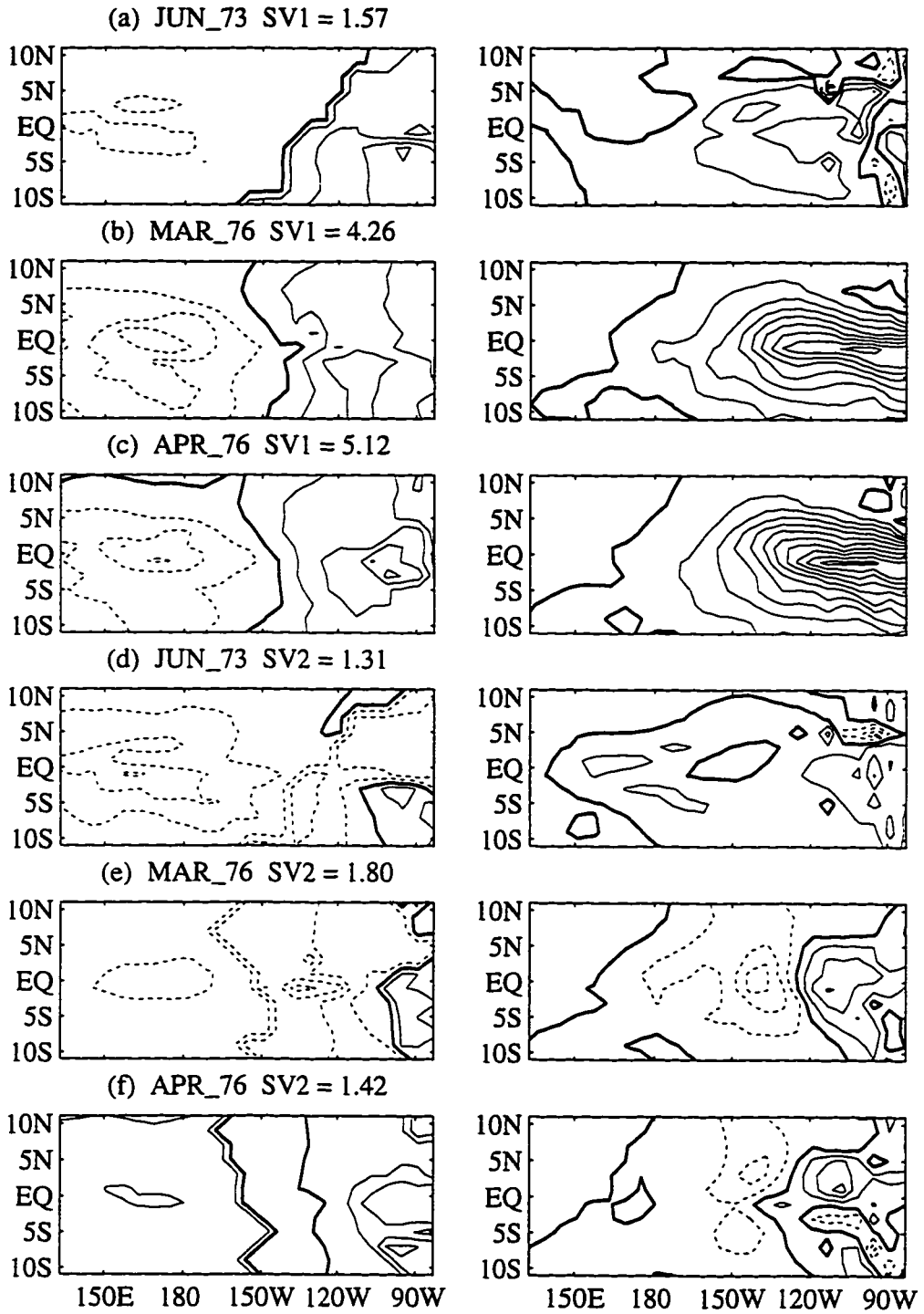

Figure 5.15 The initial (left column) and the final (right column) patterns of the first (a–c) and the second (d–f) singular vectors for three examples in which two growing singular vectors are found: June 73, March 76 and April 76.

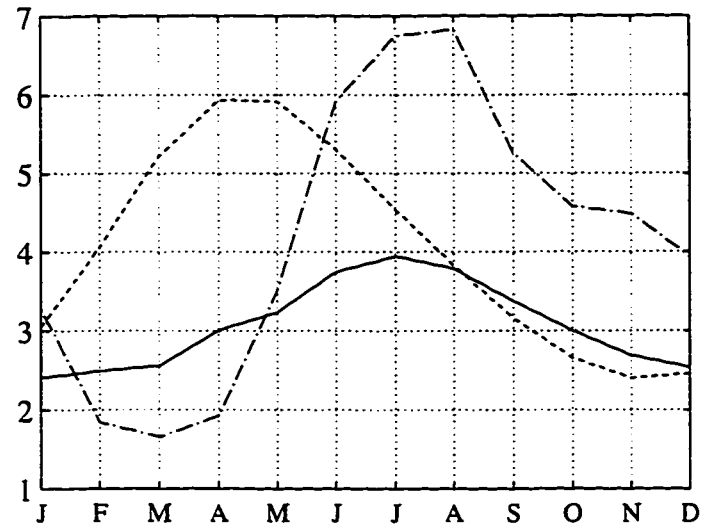

Figure 5.16 Six–month optimal perturbation growth. The solid line: annual cycle composite *SV1*, same as the dashed line in Fig. 5.10. The dashed line: *SV1* on the annual cycle climatology trajectory, same as the dashed line in Fig. 4.1. The dash-dot line: *SV1* for the perpetual January, perpetual February,..., and perpetual December conditions. The time axis indicates the 6–month integration starting month.

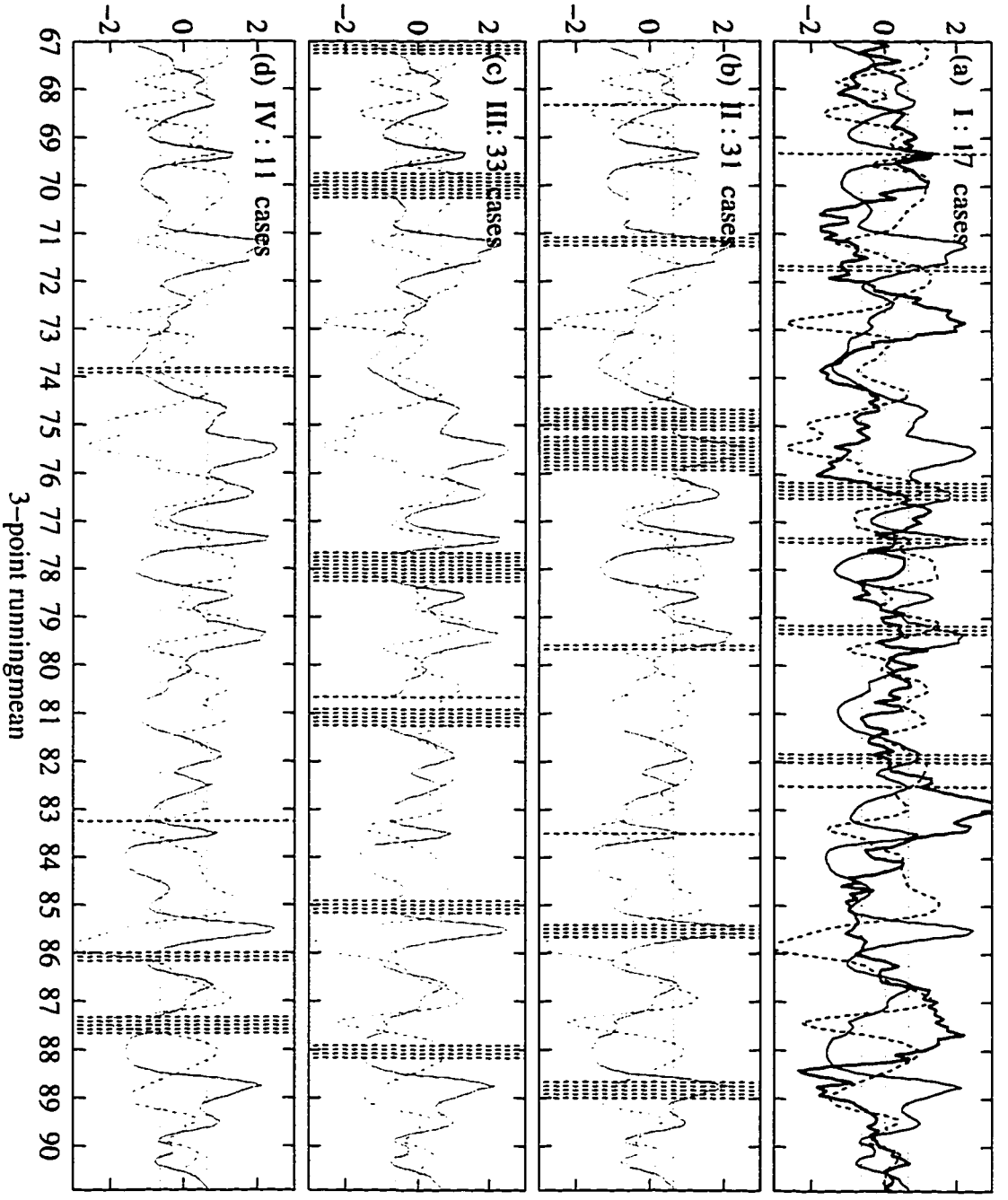

Figure 5.17 The 24–year time series of the normalized first singular values $|SV|$ (solid line) and the model forecast skill index $|FSI|$ (dashed line) from January 1967 to December 1990. Superposed in panel (a) with the thick solid line is the observed NINO3 (data from CAC). A three–month running-mean is applied to all curves. The curves in the four panels are identical, except that the vertical lines represent the forecasts belonging to the Groups I, II, III and IV defined in section 5.5.

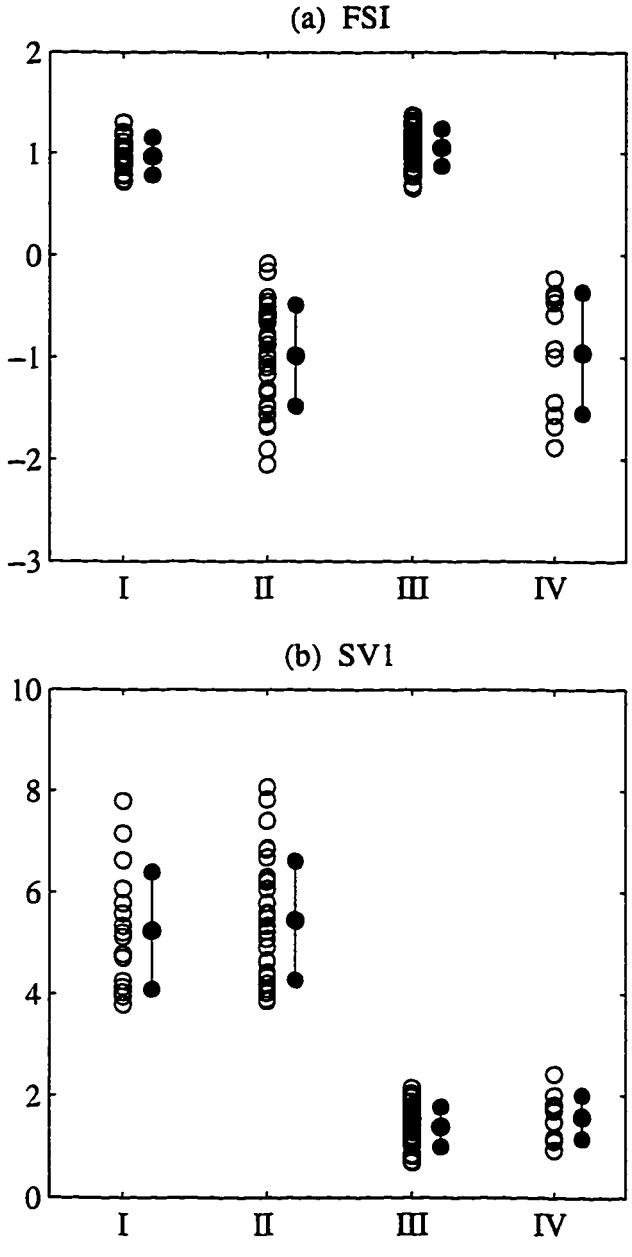

Figure 5.18 Distribution of (a) *FSI* and (b) *SV1* for forecasts in the four groups. The error bar centered with the mean of the set of values in each group is plotted. The width of the error bar is one standard deviation of the set of values in each group.

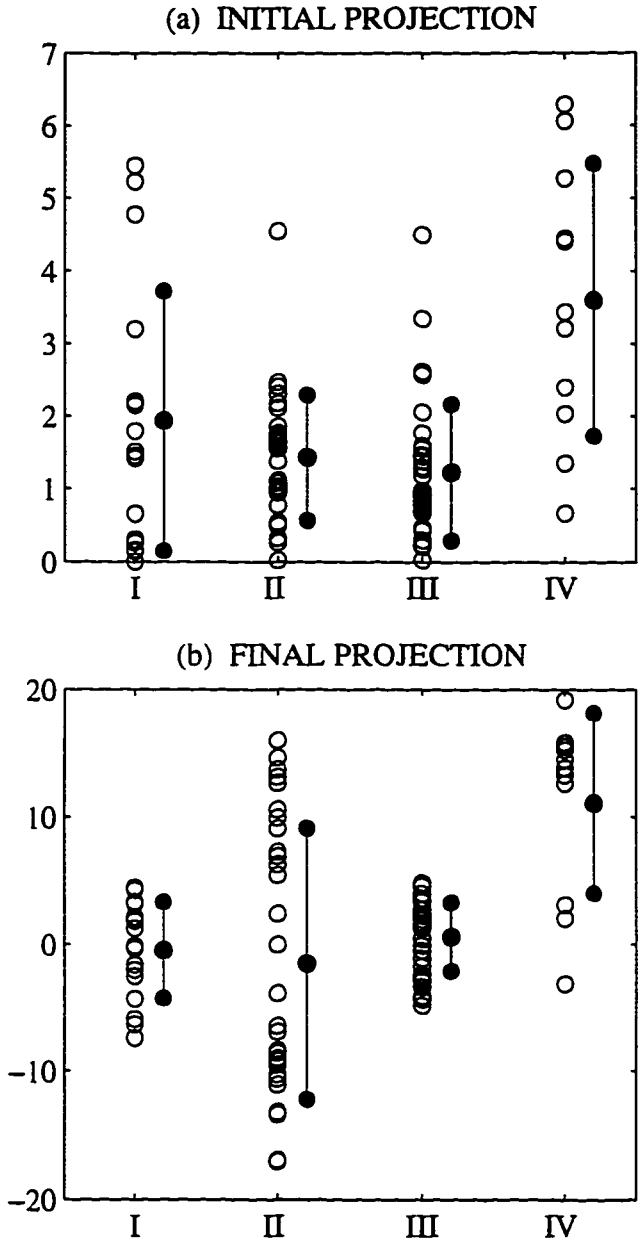

Figure 5.19 (a) Projection of the model nowcast error within 11°S–11°N of the tropical Pacific SST anomalies onto the initial pattern of the six–month optimal for Group I, II, III and IV. (b) Projection of the model forecast error within 11°S–11°N of the tropical Pacific SST anomalies onto the final pattern (rescaled, so that the norm of the final pattern optimal error is one) of the six–month optimal for Group I, II, III and IV. The error bar centered with the mean of the set of projections in each group is plotted. The width of the error bar is one standard deviation of the set of projections in each group. Here, the projection is non-dimensional.

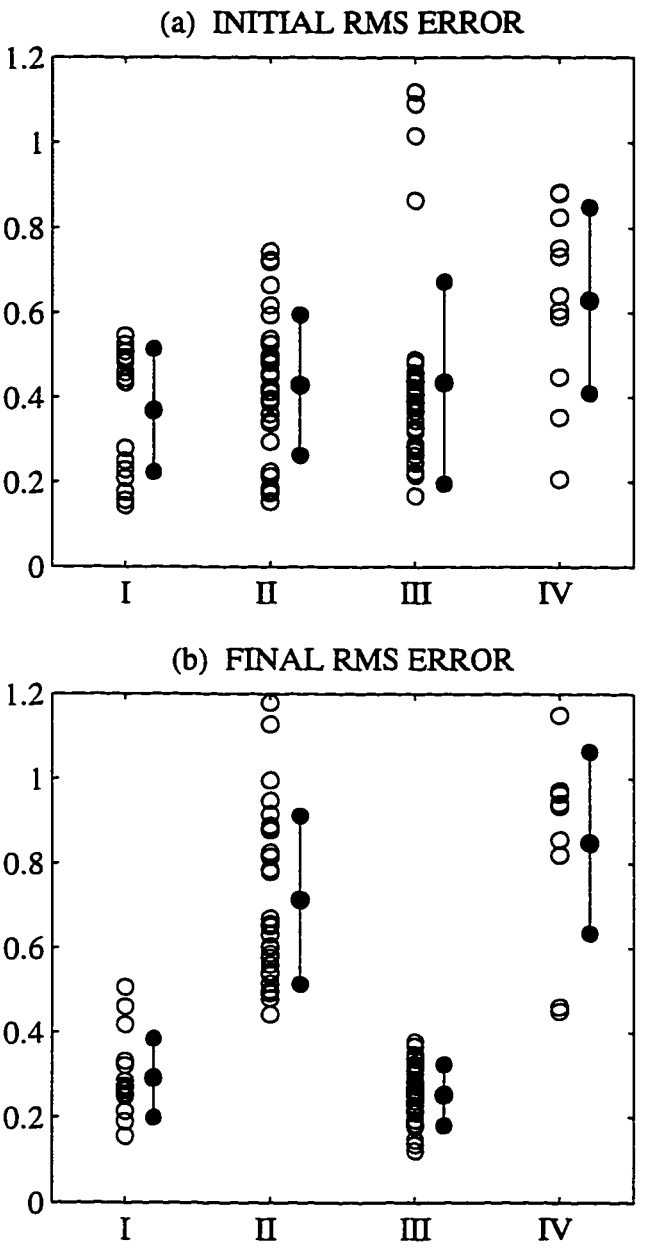

Figure 5.20 Same as in Fig. 5.19, but for the rms error in SST anomalies (°C): (a) at the forecast initialization time (nowcast error) and (b) at the forecast 6-month-lead verification time (forecast error).

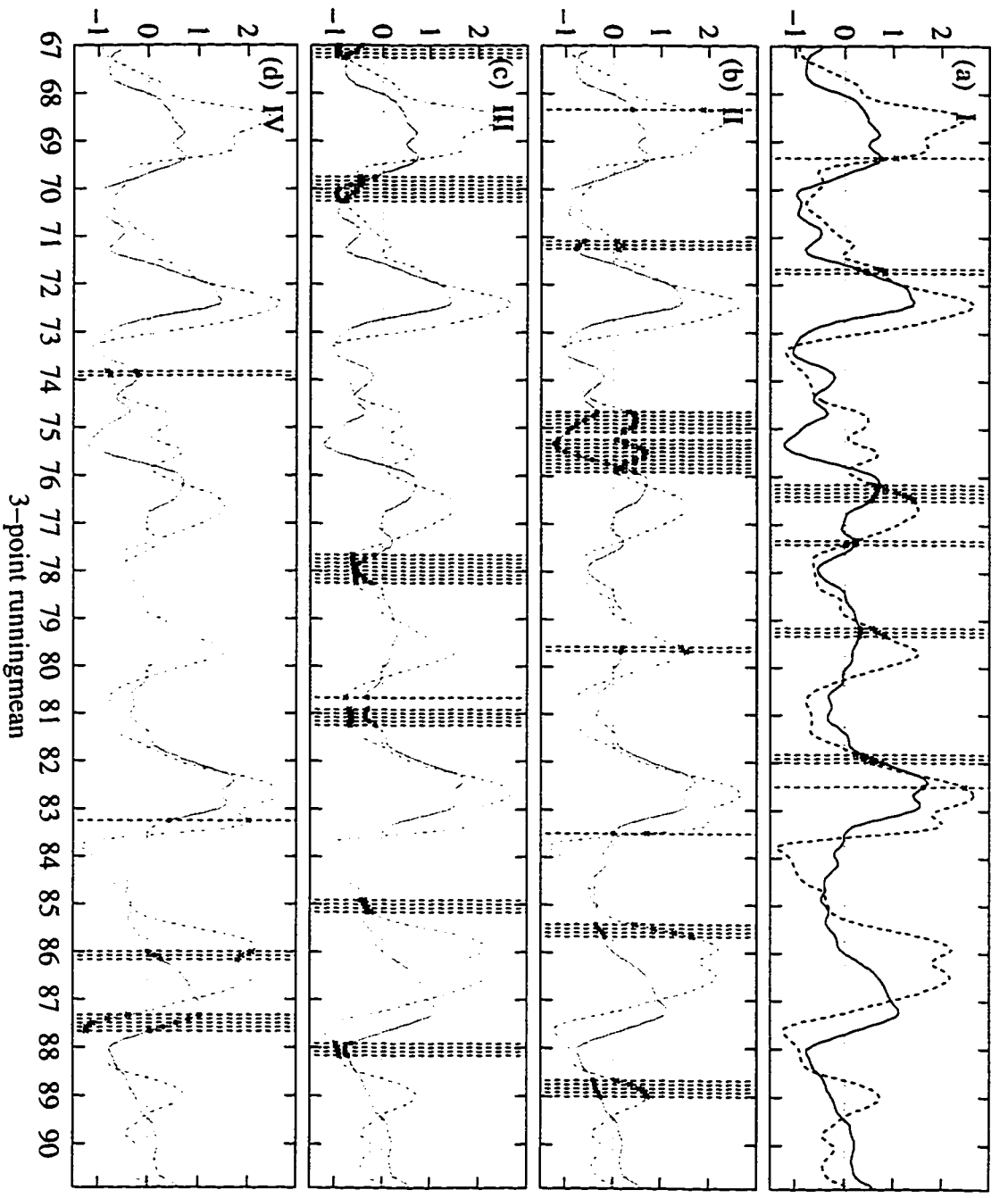

Figure 5.21 The observed (solid line) and the model forecast (dashed line) NINO3 at the six-month lead time, *verified* at the time indicated in the time axis. Forecasts in four groups are indicated by the vertical lines; the time axis referred to the forecast *initial* time (cf. Fig. 5.17).

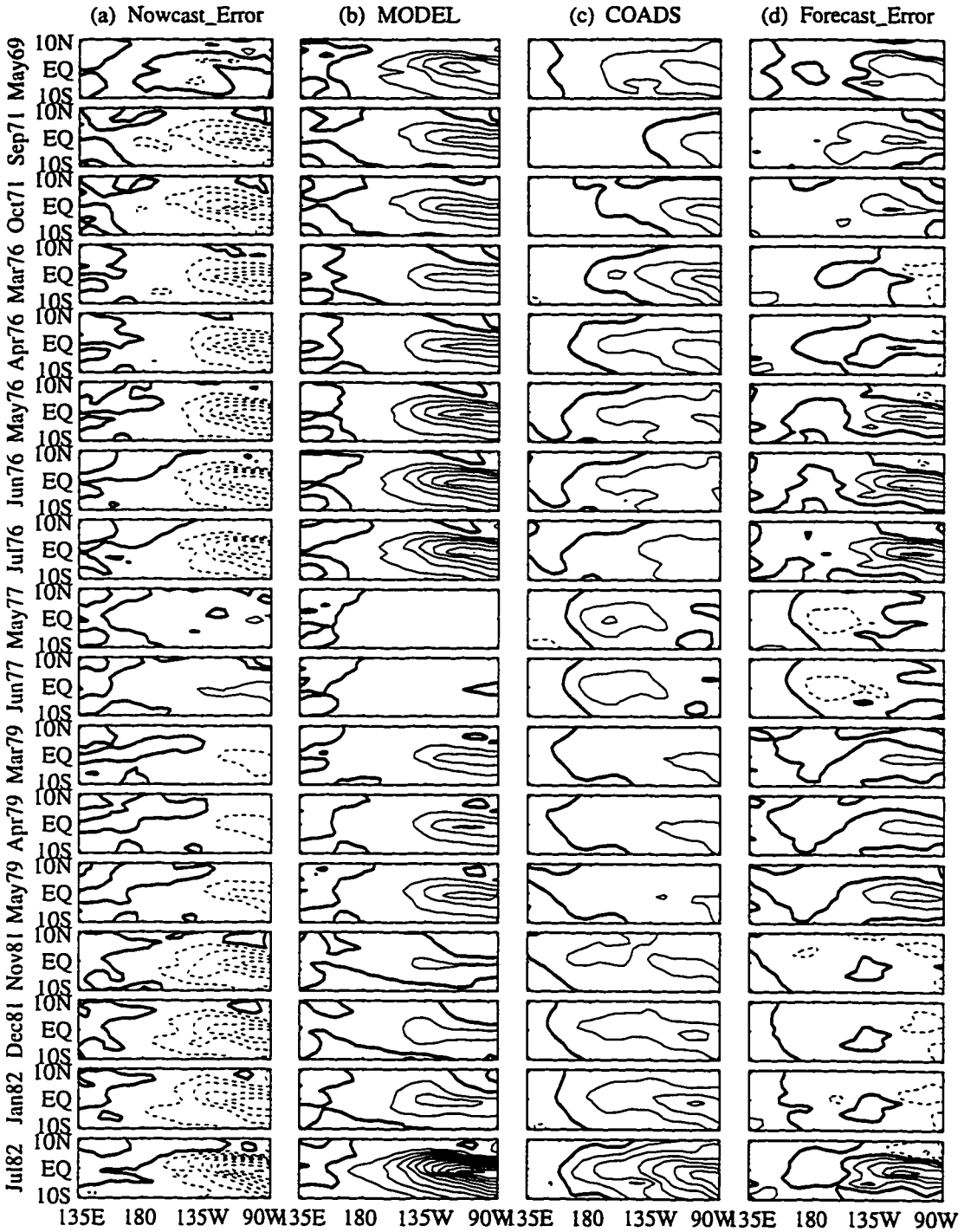

Figure 5.22 (a) Individual maps of the Group I forecasts: column (a) plots the model nowcast error, column (b) the model forecast SST anomalies at six-month lead, column (c) the COADS SST anomalies at the verification time, and column (d) the forecast error at the 6-month lead. The time indicates the forecast initialization time. Contour interval is 0.4°C for all panels.

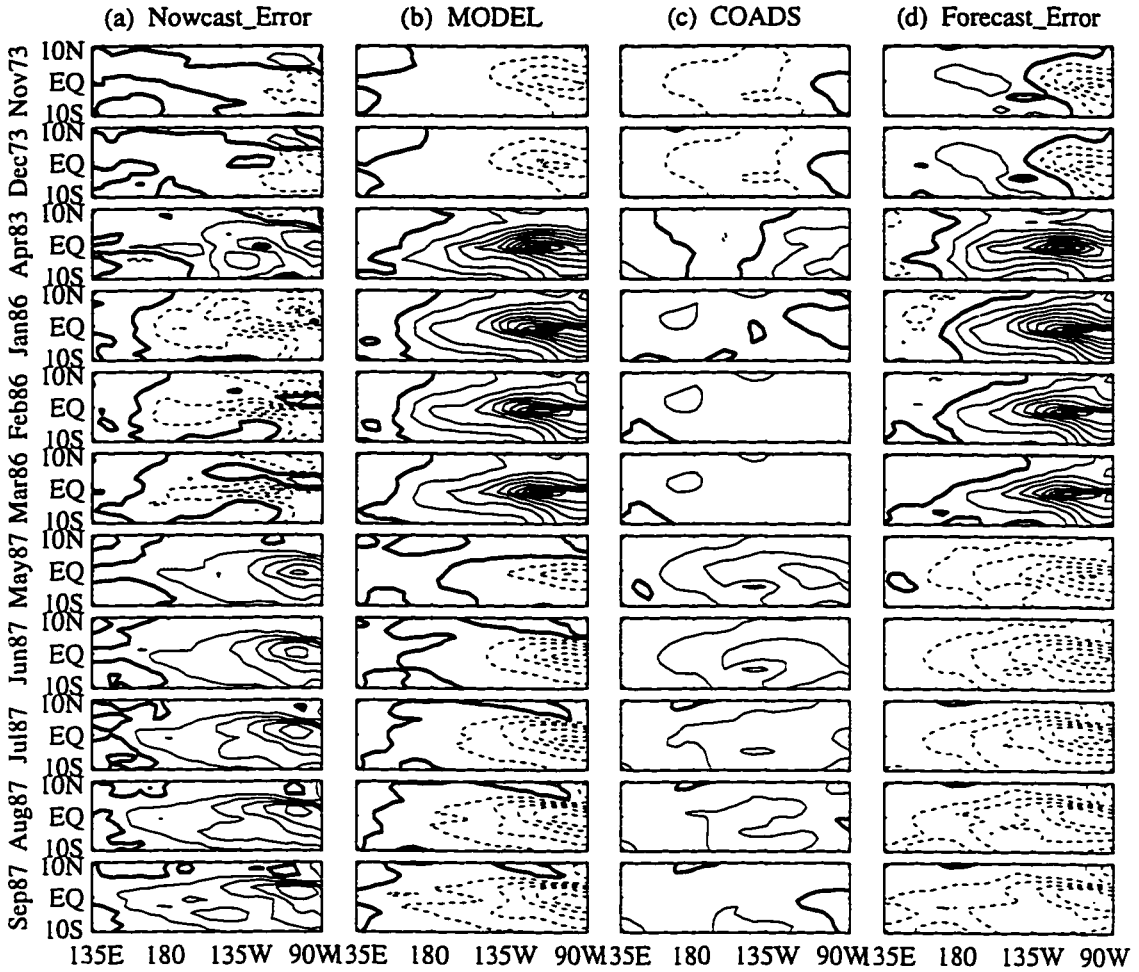

Figure 5.23 Same as Fig. 5.22, but for selected forecasts of Group IV. Contour interval is 0.4°C.

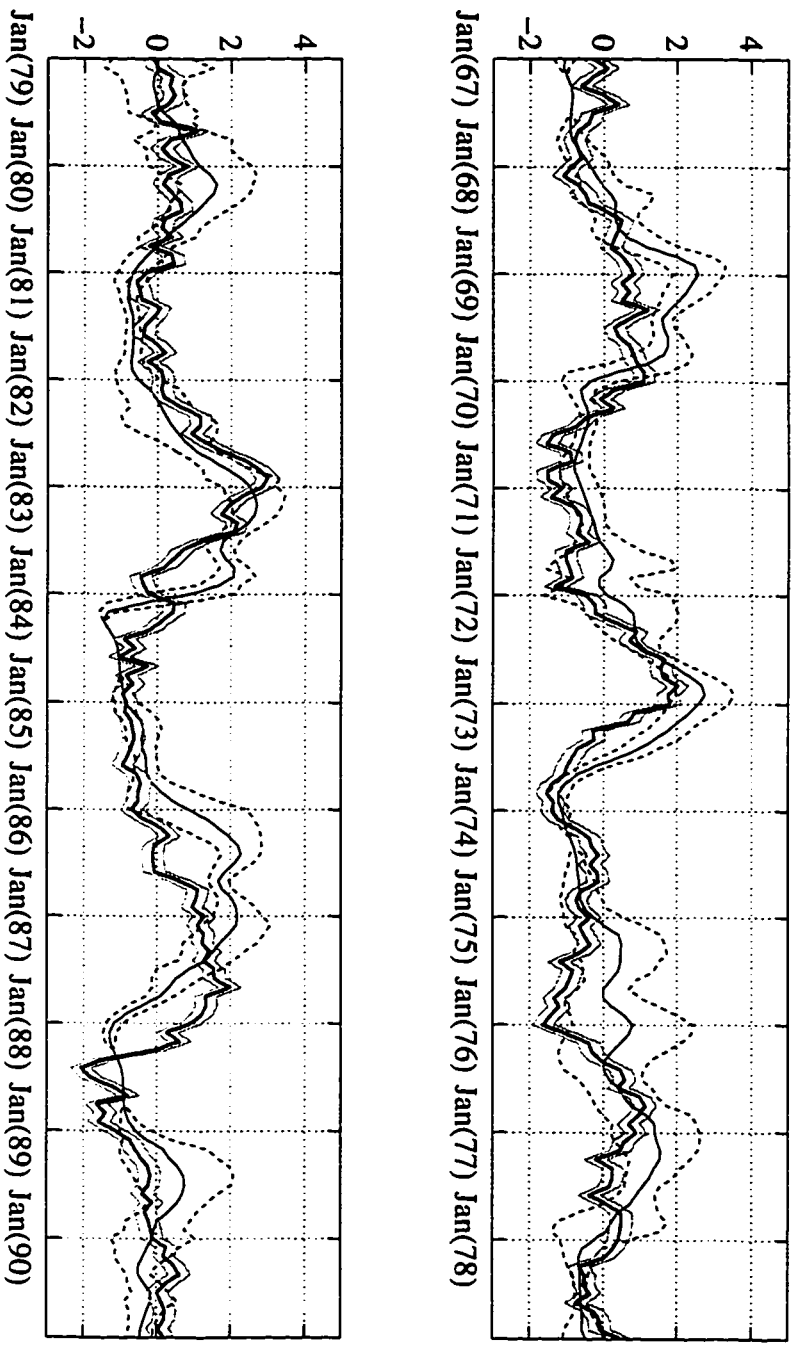

Figure 5.24 Thin solid line is the 6–month model forecast NINO3 at the verification time, enveloped by dashed lines indicating the maximum possible error implied by the optimal error growth due to initial errors in SST field alone with a 0.3°C maximum amplitude in the initial error. The thick line is the observed NINO3; surrounded with two lines representing an observational uncertainty of 0.3°C. 68% of the observed values fall within the envelop. For cases with no growing singular vectors, the width of the envelope is zero.

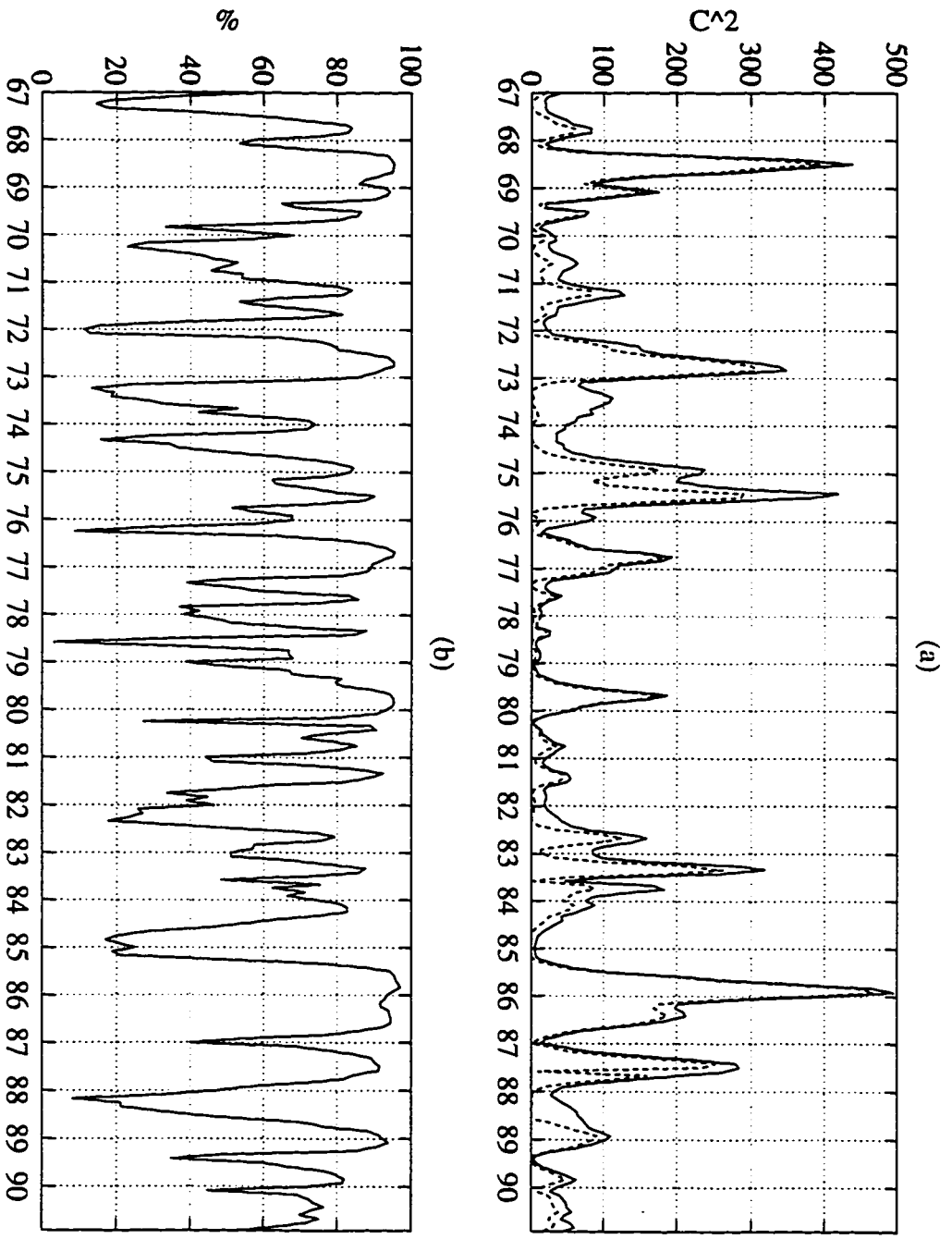

Figure 5.25 (a) The time series of the variance in the model forecast error at 6-month lead time for forecasts from 1967-90 in plotted in the solid line. The variance of the error at the forecast verification time explained by the optimal error growth is plotted in the dashed line. (b) The percentage of the variance in the forecast error explained by the optimal error growth. Time axis indicates the forecast initialization time.

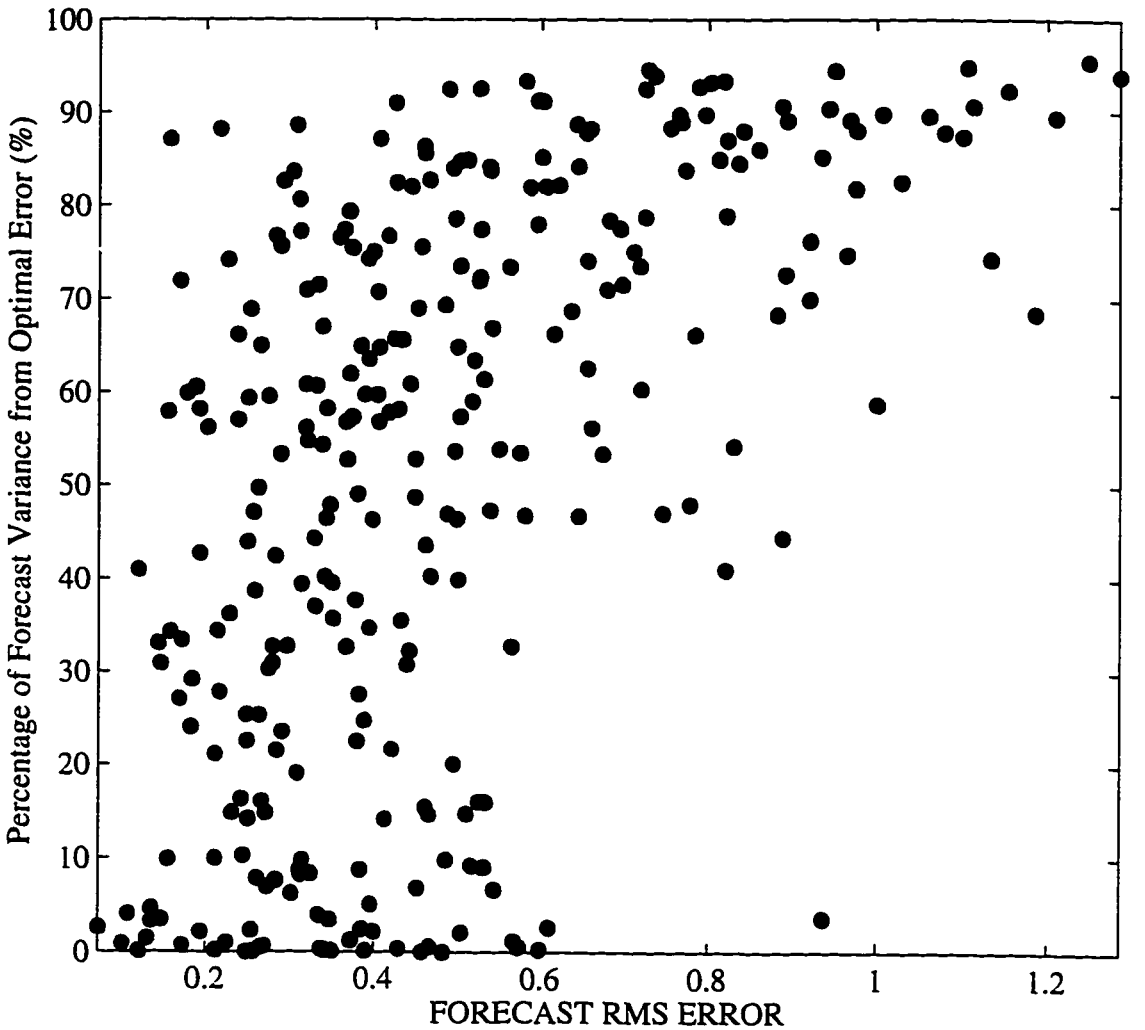

Figure 5.26 A scatter plot for the percentage of the variance in the 6-moth-lead forecast error explained by the optimal error growth vs. the rms of the 6-month forecast error.

CHAPTER 6 DECADAL VARIABILITY IN FORECAST SKILL AND OPTIMAL ERROR GROWTH

6.1 Introduction: Evidence of Interdecadal Variability

In their recent study, Zhang *et al.* (1996) constructed global regression maps of several fields (including SST, wind stress and sea level pressure) upon the *global residual* (hereafter GR) time series from 1903 to 1990. The GR time series, displayed in Fig. 6.1, was constructed by first obtaining the expansion coefficient of the leading EOF of the monthly SST anomaly field over the global domain, and then by removing from this time series the least-squares best fit to the cold tongue index, defined as the average of the SST anomalies in the eastern and central equatorial Pacific region (6°S-6°N, 90°W-178°W). Thus, the GR time series primarily represents the very low frequency variation in the Pacific climate system. Shown in Figs. 6.2a-b are the tropical portion of the global regression maps of the SST and wind stress anomalies. The large-scale SST anomalies peak in the south-eastern equatorial Pacific, and they extend throughout the subtropics in the eastern Pacific. The wind stress anomalies are also large-scale, with westerly anomalies in the central equatorial Pacific west of 145°W and easterly anomalies east of 145°W. Fig. 6.2c plots the GR time series for the period of record 1965-90; an abrupt shift in 1976 is prominent[1] in this time series. The difference in the means for the two periods is 1.5 times the standard deviation of the GR time series from 1903 to 1990.

This conspicuous climate shift is revealed not only in the regression maps but also in the time series from observations. For example, shown in Fig. 6.3 is the observed monthly NINO3 index for the period of record 1967–90. The increase in the mean value of NINO3 from 1967-75 to 1977-87 is 0.58°C.

---

1. Zhang *et al.* 1996 pointed out that, 'In the context of this longer time series, the *regime shift* in 1976-77 does not appear to be of singular importance: it is but one of a number of manifestations of the decade-to-century scale variability.'

These observations lead us to the following interesting questions. For instance, is the forecast skill different for the pre-1976 and the post-1976 epochs? Is the mean value of the skill level changed? Is the seasonal dependence of skill changed? Is the growth of the optimal error different for the two epochs? Has the mean value of the optimal error growth of the SST anomalies changed? Has the seasonal cycle of the optimal growth changed as a result of the 1976 climate shift? If the answers are *yes*, what are the possible causes? Through what mechanisms are the change in skill and the optimal error growth related?

In this chapter we will analyze the 6-month-lead model forecast skill (*FSI*) and the optimal error growth (*SVI*) over the 24-year record from 1967 to 1990 (presented in Chapter 5) and seek answers to the above questions. We first present in section 6.2 the differences of the following variables for the 1967-75 and 1977-87 epochs[2]: *(i)* the nowcast skill in NINO3, *(ii)* the forecast skill in NINO3, *(iii)* the annual cycle of *FSI* (over the 11°S-11°N domain), *(iv)* the annual cycle of *SVI* (over the 11°S-11°N domain), and *(iv)* the nowcast error and its projection upon the optimal error in SST over the 11°S-11°N domain. We pose two hypotheses to explain the change of the annual cycle in *SVI* for the two epochs and test them in section 6.3: *(i)* Change in *SVI* in the two epochs due to change in the background state climatology, or *(ii)* Change in *SVI* due to differences in the actual forecast trajectories about which the error develops. An alternative hypothesis is that change in *SVI* is due to difference in the nowcast error in two epochs. We investigate this hypothesis in section 6.4 by examining the sensitivity of the relationship between annual cycles of *FSI* and *SVI* for the two epochs to *(i)* the forecast initialization scheme and to *(ii)* the SST anomalies used in the initialization. Section 6.5 summarizes the findings.

2. The 1976 is the transient year from a cold climate state to a warm climate state, and is not included in either period.

6.2 Decadal Variability of the Forecast Skill and Optimal Error Growth

6.2.1 Nowcast skill

The nowcast is the four-dimensional model's estimate of the climate state as the model is nudged along using the observed winds (see section 5.2). In the parlance of weather forecasting, it *can be thought of* as the initialized *analysis product* using this coupled model[3]. Fig. 6.4 plots the model nowcast NINO3 (at zero-lead time) and the observed NINO3 over the periods of (a) 1967-90, (b) 1967-75, and (c) 1977–87. The temporal correlation coefficient of the model simulated and the observed time series in NINO3 is 0.7 for 1967-90. The model is more skillful in nowcasting NINO3 in the early period than in the later period: the correlation coefficient is 0.82 for the period of 1967–75, and is 0.7 for the period of 1977–87, while the rms error in NINO3 is 0.57°C for 1967-75, and is 0.7°C for 1977-87.

6.2.2 Forecast skill in NINO3

Fig. 6.5 and Fig. 6.6 display the seasonality of the model forecast skill: the averaged temporal correlation coefficient and the rms error between the model forecast and the observed time series in NINO3, for lead times from 0 to 12 months averaged over the periods of 1967-75 and 1977-87, respectively. The persistence skill is also plotted for comparison (Fig. 6.5a and Fig. 6.6a, the thick dashed curves). Note that the persistence in NINO3 for the 1977–87 period (Fig. 6.6a) is much higher than that for the 1967–75 period (Fig. 6.5a) for lead times from 0 to 16 months. Specifically, the persistence skill for the six month lead is 0.34 for the period 1967-75, it is 0.57 for the period 1977-87, and is 0.45 for the period 1967-90 (Fig. 5.7a).

---

3. There is substantial difference from the usual *analysis* because of the large influence of the model, since only the winds are nudged in the initialization (not SST or thermocline) and because of the simplified model physics. Thus, it is an *initialization* of the model.

The average temporal correlation between the time series from the model forecast and the observed NINO3 at the 6-month lead is 0.72 for the period 1967–75, and is 0.64 for the period 1977–87. Hence, in terms of temporal correlation between the model forecast and the observed time series in NINO3, forecasts made throughout the early period displayed a higher skill than forecasts made in the later period. Although the averaged model forecast skill in the correlation in NINO3 at the 6-month lead time is only slightly higher than the persistence for the period of 1977-87, the model skill over persistence is pronounced in the period 1967-75. Thus, this model is considered to have *useful* skill.

A striking difference noted in the skill plots is that the forecasts made from the period 1967-75 have a higher nowcast skill in NINO3 in the initial conditions. The temporal correlation in NINO3 decreases, and the rms error increases monotonically as the forecast lead time increases for the 1967-75 forecasts (Figs. 6.5a, c). For the period 1977-87, however, the forecasts start with a lower nowcast skill in NINO3; the temporal correlation in NINO3 decreases for lead times from 0 to 6 months but it increases for lead times from 6 to 12 months; the rms increases for lead times from 0 to 6 months but it falls back as the forecast lead time increases from 6 to 12 months (Figs. 6.6a, c). While this is interesting, we will only limit our analysis to the 6-month forecasts in this study.

The contour plots of the temporal correlation in NINO3 for the period 1967-75 exhibits a hint of the so-called *spring barrier* to predictability (Fig. 6.5b), i.e., the skill drops drastically for forecasts verified in Northern spring. This feature, however, does not show for the period 1977-87 (Fig. 6.6b); instead, forecasts verified in October exhibit a low temporal correlation in NINO3 for this later period. The reason for this striking difference may have to do with the difference in the signal-noise ratio for the two periods. To demonstrate this, we calculate the variance of the SST anomalies from observational data, by taking the square of the standard deviation of the monthly NINO3 over the selected period. Fig. 6.7 plots the annual cycle of the variance in the observed monthly mean NINO3 over the periods of 1967–75, 1977–87, and 1967–90. Notice that the variance in NINO3 for the epoch prior to 1976 has a strong annual cycle with the lowest variance in

Northern spring (March–May) and the highest variance in Northern winter (November–December). The month-to-month changes in variance for the post–1976 epoch are much weaker in comparison. The variance in February–June is increased and the variance in August–December is decreased after the climate shift. This may explain the differences displayed in Fig. 6.5 and Fig. 6.6 that one exhibits a spring barrier and the other does not. The earlier epoch 1967-75 has a clear annual cycle in the variance in SST anomalies. Hence, for forecasts verified in Northern spring, small forecast errors could represent relatively large errors, resulting in an apparent spring barrier. In the later epoch, on the other hand, the variance in SST anomalies does not change much with the seasons and the forecast skill is much less dependent on the annual cycle.

6.2.3 Six-month lead forecast skill index: *FSI*

Figs. 6.8a-b show the annual cycles of the pattern correlation coefficient (CorrCoef) and the rms error between the model forecast and the observed SST anomalies over the 11°S–11°N band, averaged over the three periods: 1967-90 (the thick solid line), 1967-75 (the thin solid line), and 1977-87 (the dashed line). Note that the pattern correlation coefficient for forecasts made starting from May through August is higher in the pre-1976 epoch, and the pattern correlation coefficient for forecasts made starting in January-April or September-December is higher in the post-1976 epoch (Fig. 6.8a). The rms error, on the other hand, is smaller during the post-1976 epoch than during the pre-1976 epoch, regardless of the forecast starting month (Fig. 6.8b). These two combining effects result in a higher score of the monthly *FSI* for the forecasts made in the post-1976 epoch, but the forecasts made starting in May-June for the two epochs in fact have comparable *FSI* (Fig. 6.8c).

6.2.4 Six-month optimal error growth: *SVI*

Shown in Fig. 6.8d are the annual-cycles of the *SVI* for the two periods. Both are strongly dependent on the seasonal cycle. We note that *SVI* for the early period 1967-75 has an annual cycle peaking in June, while the annual cycle of *SVI* for the period 1977-87 achieves its peak value in July, with a slightly greater amplitude in its peak value. However, the overall average of the *SVI* is slightly higher for the early period than that for the later period (3.12 vs. 2.88). This decrease in *SVI* is consistent with an increase in the skill *FSI* of the forecasts made in the later period.[4]

6.2.5 Pattern nowcast error in SST and it projection upon the optimal error

Fig. 6.8e further displays the annual cycle of the nowcast error in SST over the 11°S-11°N domain for the three periods: 1967-90, 1967-75 and 1977-87. Fig. 6.8f displays the annual cycle of the projection (non-dimensional) of the normalized (unit-norm) nowcast error upon the optimal error in SST (with a unit norm). The pattern nowcast error and the projection on the optimal SST is smaller in the later epoch, contrary to the nowcast error in NINO3 which shows an increase in the later epoch.

6.3 Why did the Annual Cycle of *SVI* Shift from 1967-75 to 1977-87

Recall that the six-month optimal perturbation growth calculated from the annual cycle climatological reference trajectory has an annual cycle *SVI* that peaks in April (Fig. 4.1). The six-month optimal error growth calculated from the actual forecast trajectory, however, achieves its peak value in July (Fig. 5.10). In addition, when the annual-cycle

---

4. The difference in the annual-means of *FSI* and *SVI* in two periods are tested using student t-test. The means of the *FSI* and *SVI* fail to pass the significant test. However, if only the seasonal means are taken into consideration, and the independent number of degrees of freedom are estimated by assuming independent annual mean values from year to year; i.e., we have 9 independent points for the first period and 11 for the later period. The November-February means of *FSI* over the two periods are significantly different at a confidence level of 88%; the March-May means of *SVI* over the two periods are significantly different at a confidence level of 72%.

SVI is obtained from 1967-75 and 1977-87 separately, we find a slight difference in the phasing of the two annual cycles (Fig. 6.8d). These raise some questions. Why is the instability in the atmosphere-ocean climate system changed from decade to decade? Is the change in climatology after the 1976 climate shift the major cause of the phase shift between the annual cycle of the two epochs? Or, is the change due to the difference in the forecast trajectories? To answer these questions, we will first design experiments to identify the affect of the change in the model basic state climatology[5] on the change in the annual cycle of *SVI*.

6.3.1 Sensitivity of *SVI* to the observed change in climatology

The restart files described in section 5.2 contain the surface current, the upwelling, the thermocline displacement, the SST and the surface wind anomalies for each month from January 1961 to December 1990. The anomalies averaged over the periods 1967-75 and 1977-87 are the model estimate of the change in the annual-cycle climatology before and after 1976, representing a cold (1967-75) and a warm (1977-87) tropical climate state, respectively. For convenience, we will refer to the average of the model-generated anomalies over the period 1967-75 as *CLIM_I* and the average of the period 1977-87 as *CLIM_II*. The difference maps (*CLIM_II* minus *CLIM_I*) for January, April, July, and October of the surface wind anomalies and the SST anomalies are displayed in Fig. 6.9 and Fig. 6.10. The difference map in surface wind stress field displays westerly anomalies in the central equatorial Pacific (Fig. 6.9), which corresponds to positive SST anomalies in the eastern and central equatorial Pacific (Fig. 6.10). These difference maps show a larger amplitudes in April and smaller amplitudes in October in both the surface wind stress and the SST anomaly fields.

5. From a long-term integration using the Battisti coupled model, we notice that the average of the long-term time series of the model generated anomalies is not zero: a warm *bias* exists.

We design the following three experiments:

- *Experiment i – the standard climate*: This is the control experiment that is described in section 4.3.1. In this experiment, we calculate the 6-month optimal perturbation growth on the reference trajectory defined by the standard annual-cycle climatology. Results are summarized in Fig. 4.1.
- *Experiment ii – the colder climate*: This is a second set of calculations carried out using *CLIM_I* added to the standard model climatology as the model basic state.
- *Experiment iii – the warmer climate*: A third set of calculations is carried out using *CLIM_II* added to the standard model climatology as the model basic state.

The resulting annual cycle of the 6-month optimal perturbation growth for the above three experiments are plotted in Fig. 6.11. The three curves are qualitatively the same, except for a slight change in amplitude but not in phasing. The 6-month optimal growth of the perturbation starting in April and May and ending October and November is the greatest, while the growth starting November and December and ending May and June is the least. The 6-month integrations starting November-April experience the warm seasons in the tropical Pacific; when the climatology is changed to the slightly colder climatology, the basic state (in the warm season) is slightly closer to the annual mean, resulting in a small increase of instability and hence, a small increase in the optimal perturbation growth. Contrarily, when the climatology is changed to the warmer climatology, the basic state (in the warm season) is even farther away from the annual mean value. For example, the thermocline is even deeper in the warm climatology, making it more difficult to exhibit more instability, hence, a smaller *SVI* results. The difference between the two decades for integrations starting in the second half of the year is much smaller.

Obviously, the change in climatology does *not* explain the change in phasing of *SVI* for the two epochs, 1967-75 and 1977-87 (cf. Fig. 6.11, Fig. 6.8d and Fig. 4.1), and we must appeal to an alternate hypothesis.

The three sets of experiments in section 6.3.1 rejects the hypothesis that the phase shift in the annual cycle of *SVI* in the two epochs resulted from the change in climatology in the two epochs. We will examine in next section an alternative hypothesis: is the change in *SVI* due to the change in the actual forecast trajectories?

6.3.2 Sensitivity of *SVI* to the actual forecast trajectories

Recall from Fig. 5.11 that *SVI* on the four-year composite ENSO cycle is dominated by the annual cycle, and modified by the interannual variability. Here, instead of doing the composite, Fig. 6.12 displays the four-year time series of *FSI*, *SVI*, and NINO3 for each of the five individual ENSO events, which we summed to form the composite discussed in sections 5.3.3 and 5.4.3. We will now focus only on the four-year time series of *SVI* (the thin solid curve). The *SVI* for the 69-70 event has three peaks, which are all found in Northern spring, April-June (Fig. 6.12a). *SVI* for the 72-73 event, on the other hand, has two major peaks, one in Northern spring and the other in September (Fig. 6.12b). For the 76-77 event, *SVI* has one major peak each year, in July, June, May-June, and August (Fig. 6.12c). The peaks of *SVI* for the four years centered on the 82-83 event occur in November-December, July, and July, and September (Fig. 6.12d). Finally, for the 86-87 event, *SVI* peaks in July, August-September, and October (Fig. 6.12e).

Since the *SVI* is dependent on both the phase of the annual cycle and the ENSO cycle, and the ENSO episodes are not perfectly phase-locked to the annual cycle, it is not surprising that the annual cycle of *SVI* changes when different decades are averaged. In our study, peak *SVI* for the period of 1977-87 happens to be achieved one month later than does the peak *SVI* for the period of 1967-75. To further elucidate this point, we take the four-year time series of *SVI* from each of the five ENSO episodes, and average about the calendar months to obtain the annual cycle for each of the five ENSO episodes. The five annual cycles are displayed in Fig. 6.13. It is clear that the 82-83 and the 86-87 ENSO events contribute to shift the peak of *SVI* toward later in the year (Fig. 6.13b).

6.4 The Impact of Nowcast Error on the Annual Cycle *FSI* and *SVI*

One may speculate the change in the annual cycle of *FSI* and *SVI* after the 1976 climate shift might be due to the difference in the nowcast error in the two epochs. To examine this possibility, we perform and discuss another two additional sets of experiments in the following sections.

6.4.1 Sensitivity to the initialization scheme

To examine the sensitivity of our results to the initialization scheme, we perform a set of calculations using the same model but with the *old* initialization scheme of Cane *et al.* 1986 (see also section 5.2.1). Model forecasts for lead times from 0 to 12 months and the optimal error growth over six-month integrations starting each month from 1967 to 1990 are carried out and analyzed. It is worth mentioning again that when the observed surface winds are replaced with the model winds at the forecast initial time, it creates a shock to the model at the beginning of the forecast which seriously affects the coupled model performance through atmosphere-ocean coupling processes.

Fig. 6.14 briefly summarizes the results of the forecast skill and the optimal error growth. The annual cycles of the *FSI* (Fig. 6.14c) and *SVI* (Fig. 6.14d) for the two periods before and after 1976 are different from those presented in Fig. 6.8c-d. The difference in *FSI* for two periods using the old initialization scheme is much more distinct than that using the new initialization scheme. The later period has a higher forecast skill than the early period in terms of the pattern correlation (Fig. 6.14a), the rms (Fig. 6.14b) and the *FSI* (Fig. 6.14c), independent of the forecast starting months. In addition, when the old initialization scheme is adopted, the optimal error growth over six-month integrations starting January–June is much larger in the 1967-75 period than in the 1977-87 period; the difference for integrations starting July–November is small. Specifically, the mean values of the *FSI* are -0.22 and 0.43 for the 1967-75 and 1977-87 periods, respectively. This

increase is consistent with the decrease seen in the mean values of the *SVI* (3.54 vs. 3.15 for the 1967-75 and 1977-87 periods): the *FSI* and *SVI* are primarily inversely correlated.

6.4.2 Sensitivity to the SST anomalies in the initialization

Next, to examine the sensitivity of our results to the SST anomalies at the forecast initial time, we perform another set of calculations using the same model and the same new initialization scheme as in section 5.2.1, except that at the forecast/integration starting time, the SST anomalies generated by the coupled model are replaced by the *COADS* SST anomalies. This replacement, on the one hand, minimizes the nowcast error in the SST anomalies, hence, the nowcast error is entirely observational and is independent of the model. On the other hand, this initialization creates a shock in the SST anomalies at the initialization time which immediately generates a wind shock in the forecast.

Model forecasts for lead times from 0 to 12 months and optimal error growth over the six-month integrations starting each month from 1967-90 are carried out. Fig. 6.15 displays the resulting annual cycle of the forecast skill and the optimal error growth. As we can see, the later period has a larger mean value of *FSI* and a much larger *SVI* that is independent of the starting months, breaking the inverse relation. This implies that, neglecting changes in the nowcast error (i.e., making the nowcast error independent of the model forecast), the model is more sensitive in the later period than in the early period. The fundamental difference between the results from this experiment and those in our standard case (Fig. 6.8) suggest that the nowcast error (or the initialization in SST) may play a crucial role in affecting the model sensitivity and in determining the model predictability.

6.5 Conclusion

In Chapter 5, we examined the relationship between the model six-month forecast skill and the optimal error growth in the equatorial sea surface temperature (SST) for the period of 1967–90. Systematic variations in the model forecast skill and the optimal error growth are dominated by the seasonality with some degree of modification by the interannual variability. In this chapter, we demonstrated that the seasonalities in both the model forecast skill and the optimal error growth exhibit a decadal change for the periods before and after 1976.

The *pattern* correlation coefficient and rms error between the model forecast and the observed SST anomalies over the 11°S–11°N band is higher during the post-1976 epoch than during the pre-1976 epoch. However, for NINO3, the *temporal* correlation coefficient and rms error between the model forecast and the observed time series in NINO3 is higher in the pre-1976 epoch than it is in the post-1976 epoch.

The optimal error growth about the forecast trajectory is given by the leading singular value (*SV1*). For the 6-month optimal growth, *SV1* exhibits a decrease in late Northern spring and an increase from Northern summer to Northern fall from the pre-1976 epoch to the post-1976 epoch. We carried out experiments to examine the sensitivity of *SV1* to the change in the basic state climatology, where the change in climatology is taken from the model generated anomalies averaged over the pre-1976 and post-1976 epochs, which represent times of cold and warm climatological deviations, respectively. Results imply that the low frequency change in climatology does not account for the change in the annual cycle of the leading singular values. We demonstrated that the differences in the trajectory of the individual ENSO cycles from the pre-1976 to the post-1976 epochs was most responsible for the phase shift of the annual cycle of *SV1*. Hence, the climate trajectory has an important impact on the seasonality of *SV1* on the decadal time scale.

Having examined the cause of the change in *SV1* for the two epochs, we qualify the above discussion that although there seems to be a change in the annual cycle and the

mean value of the *FSI* and *SVI* for the two epochs, the difference in the mean *FSI* and mean *SVI* for the two epochs does not pass the significant test at the 90% confidence level owing to a small sample in the record: 9 for the early period and 11 for the later period. Even so, the decadal change in these statistics are consistent. *Compared to the 1967-75 period, the 1977-87 period sees an increase in FSI (Fig. 6.8c) that is accompanied by a decrease in SVI (Fig. 6.8d), a decrease in the nowcast error (Fig. 6.8e) and a decrease in the projection of the nowcast error upon the optimal error in SST (Fig. 6.8f) over the 11°S-11°N domain.* Hence, in the later epoch, all three effects are compounded in a manner that lead to an increase in forecast skill.

To summarize, we have shown the optimal error growth (*SVI*) is largely determined by the seasonal cycle in the basic state and secondly by the reference trajectory on which the integrations are performed. For the calculations that we carried out (in Chapters 4, 5 and 6), even though there is a phase change in the seasonality of *SVI*, the peak values are all achieved in Northern spring or Northern summer (see Figs. 4.1, 4.9, 4.10, Figs. 5.10, 5.11, and Figs. 6.12, 6.13). The reason for this is that the six-month integrations starting Northern spring and Northern summer experience the most unstable time of the year (i.e., the Northern summer), which allows the error to develop efficiently. Six-month integrations starting Northern winter, however, exhibit much smaller error growth because the integrations do not include the Northern summer.

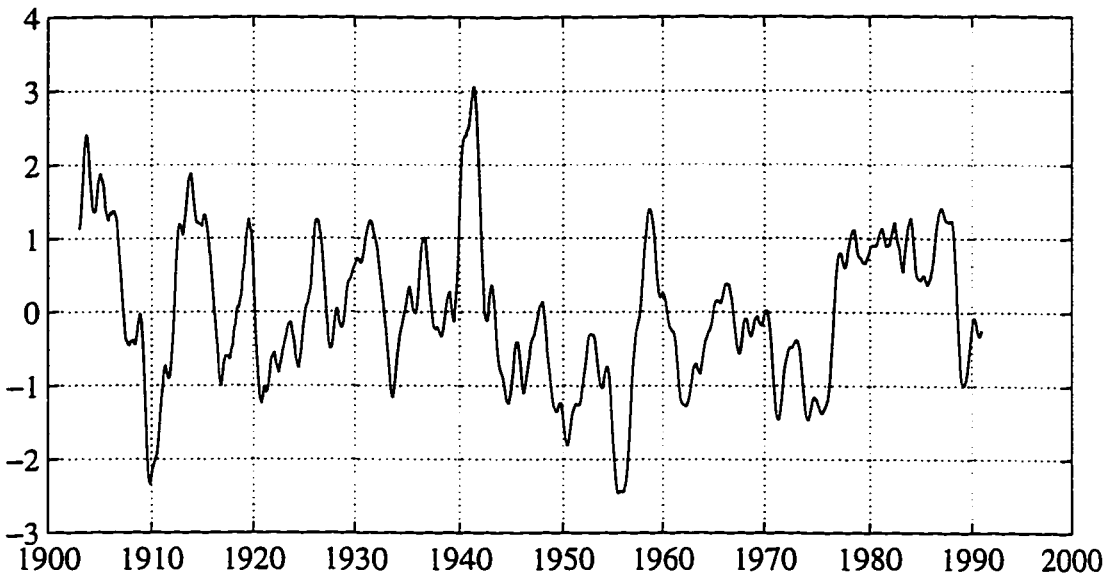

Figure 6.1 Global Residual time series 1903-1990 (data from Zhang *et al.* 1996). Units are in standard deviations.

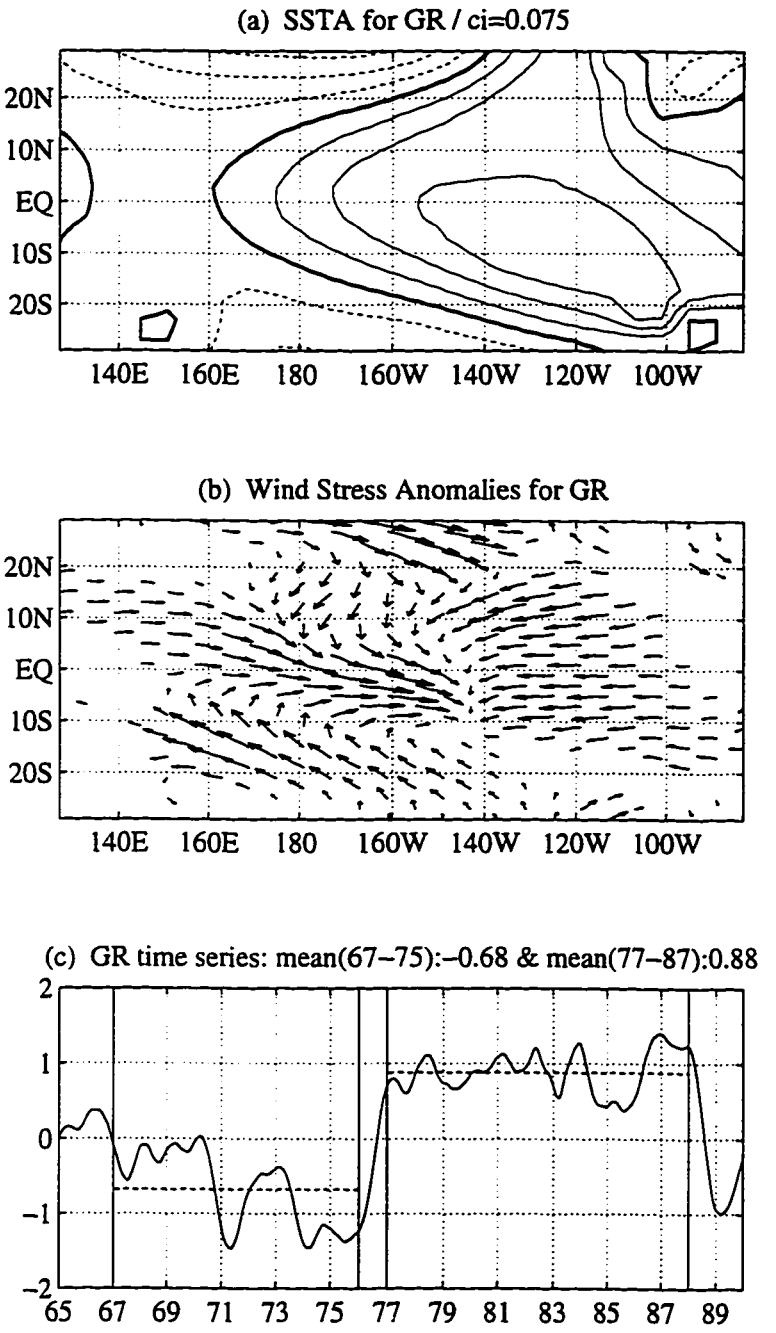

Figure 6.2 Tropical Pacific portion of the Global (a) SST anomalies and (b) the wind stress anomalies regressed upon the Global Residual time series over the period of 1903-1990 (data from Zhang *et al.* 1996). (c) is the section for the period from 1965-1990. The mean in the time series (in terms of standard deviations) for 1967-1975 (~-0.68) and 1977-1987 (~0.88) are plotted in dashed lines. The wind stress anomaly vectors are not plotted if amplitudes are less than 1/5 of the maximum value.

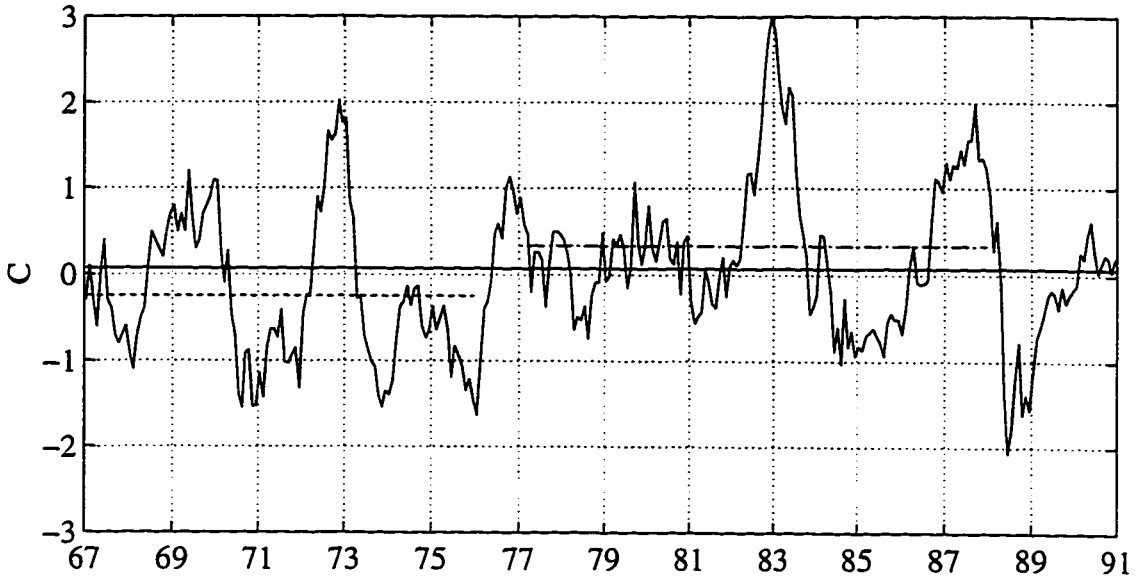

Figure 6.3 NINO3 reported by CAC. The mean values for the 1967–75 and the 1977–87 periods are –0.25°C and 0.33°C, respectively, and are indicated in horizontal dashed and dash-dot lines.

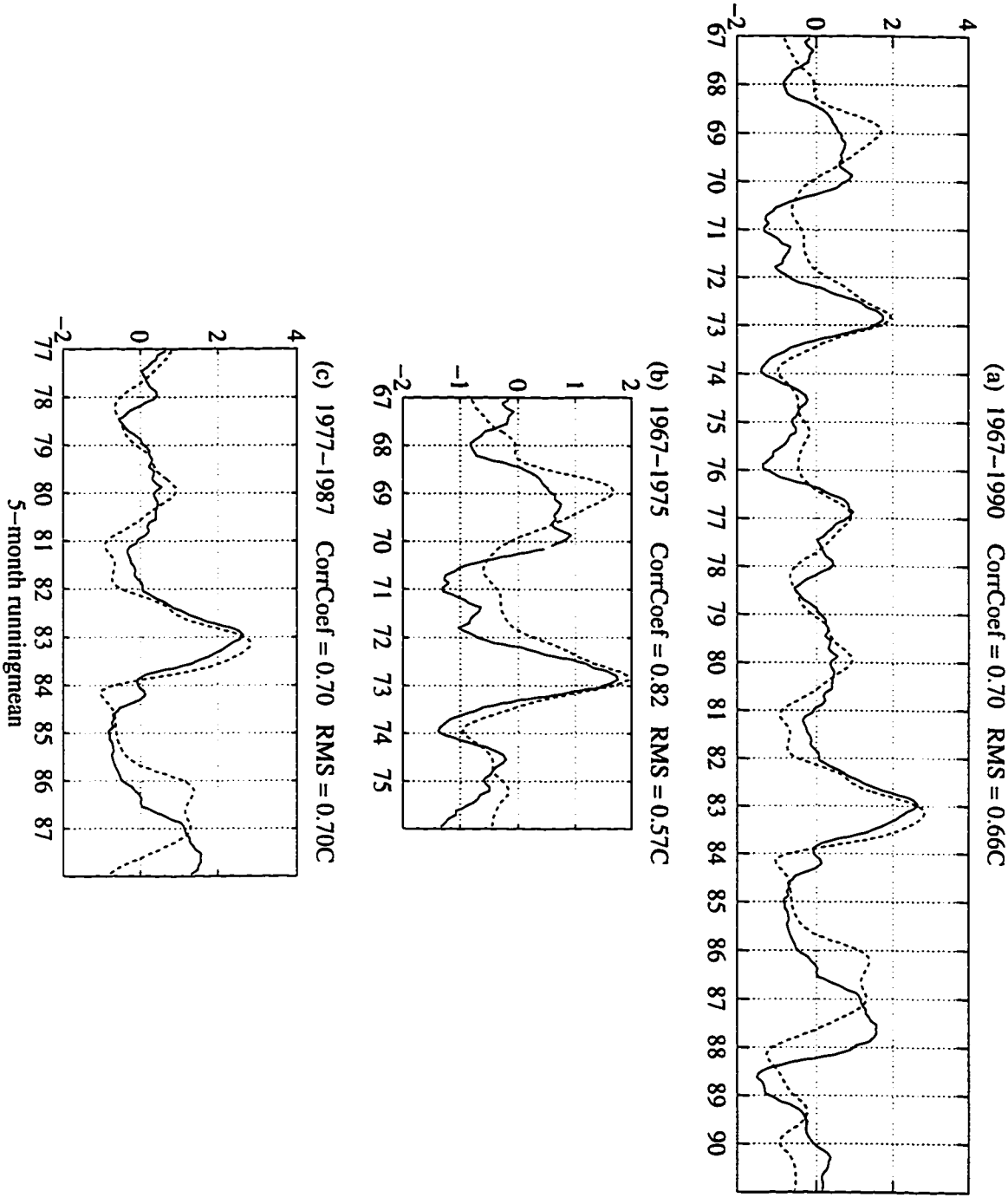

Figure 6.4 Model simulated (nowcast; zero-lead) and observed (CAC) NINO3 for the period of (a) 1967-90, (b) 1967-75 and (c) 1977-87 The correlation coefficient and rms error for the model nowcast and the observed are shown. A five-month running-mean is applied to all curves.

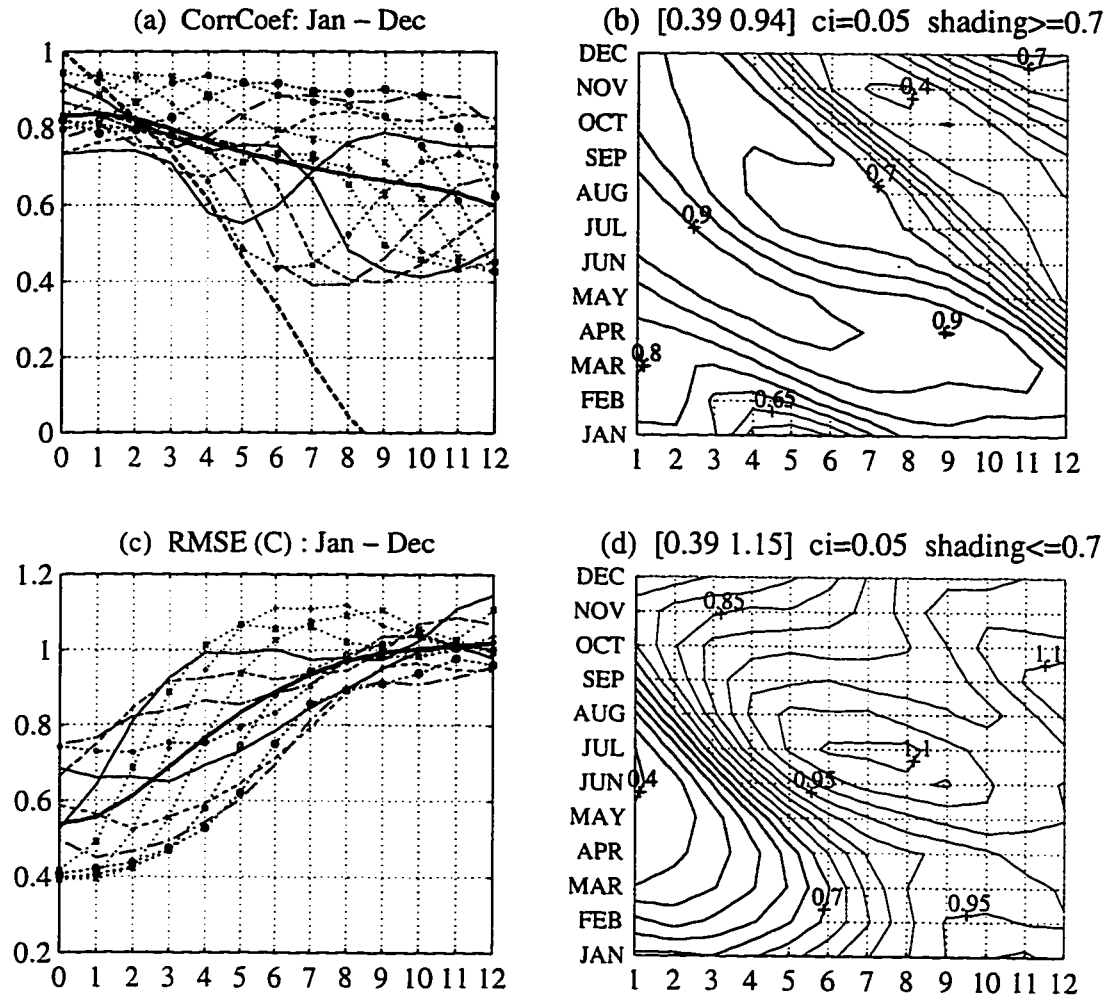

Figure 6.5 The seasonality of the model forecast skill in NINO3 for the period of 1967-75. (a–b) The temporal correlation coefficient, and (c–d) the rms error between time series of the model forecast and the observed SST anomalies (from CAC) averaged over the Niño3 region. The left column figures are line plots; each plot includes twelve curves representing averaged January start to averaged December start. The thick solid line is the grand mean of the correlation coefficient for lead times 0 up to 12–months. The right column figures are the equivalent contour plots, starting January to December for one–month forecast to twelve–month forecast lead times. The contour interval and the shading level are printed as reference. The corresponding NINO3 forecast skill for the entire record 1967-90 are found in Fig. 5.7.

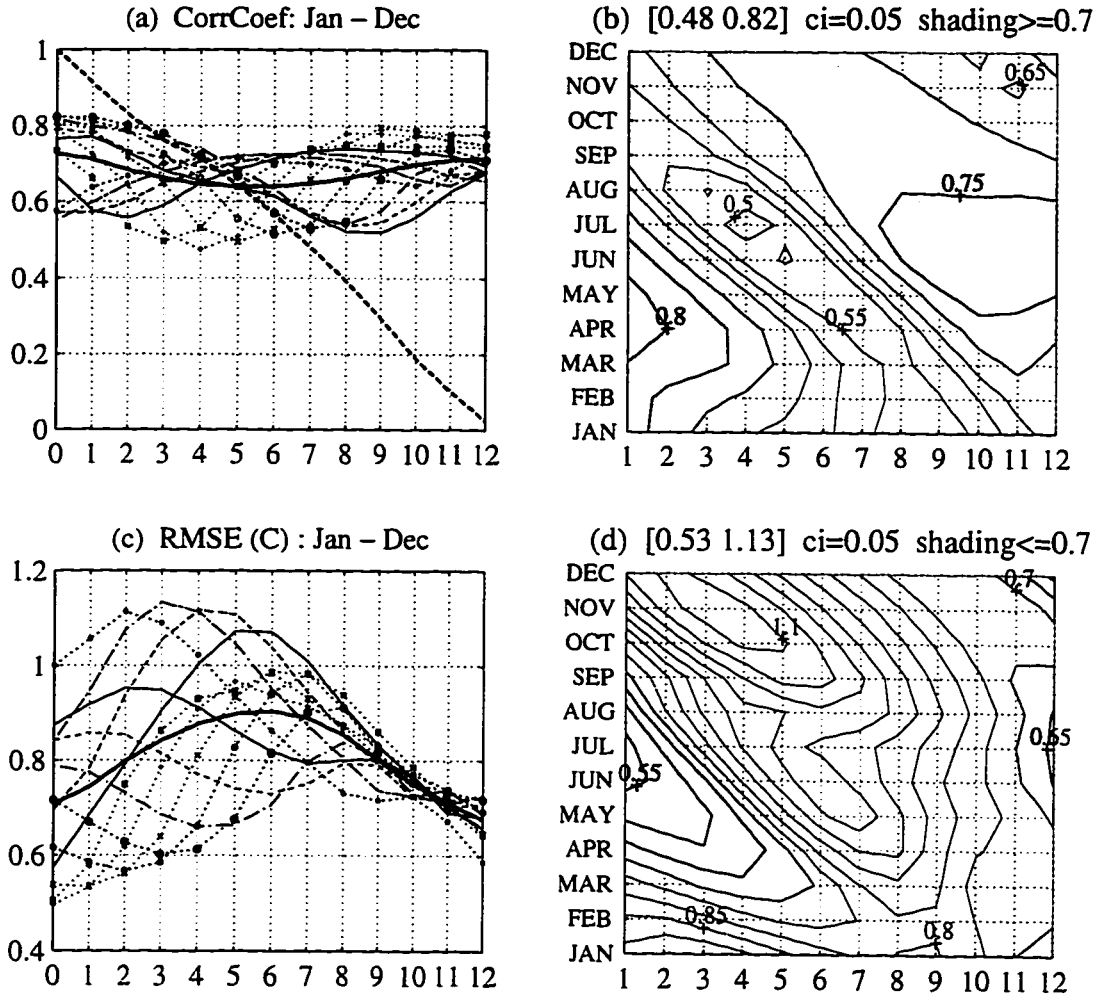

Figure 6.6 Same as in Fig. 6.5 but for the period 1977-87.

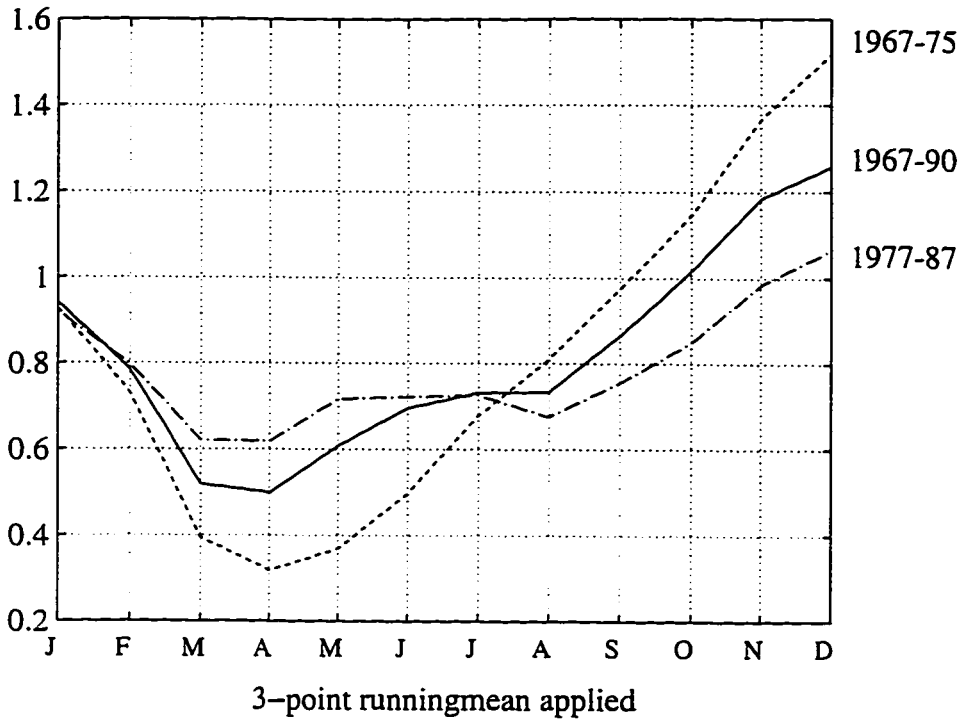

Figure 6.7 The temporal variance of NINO3 for the three periods: 1967-90 (solid line), 1967-75 (dashed line) and 1977-87 (dash-dot line). A three–month running-mean is applied to all curves. Unit in the vertical axis is $^{\circ}C^2$.

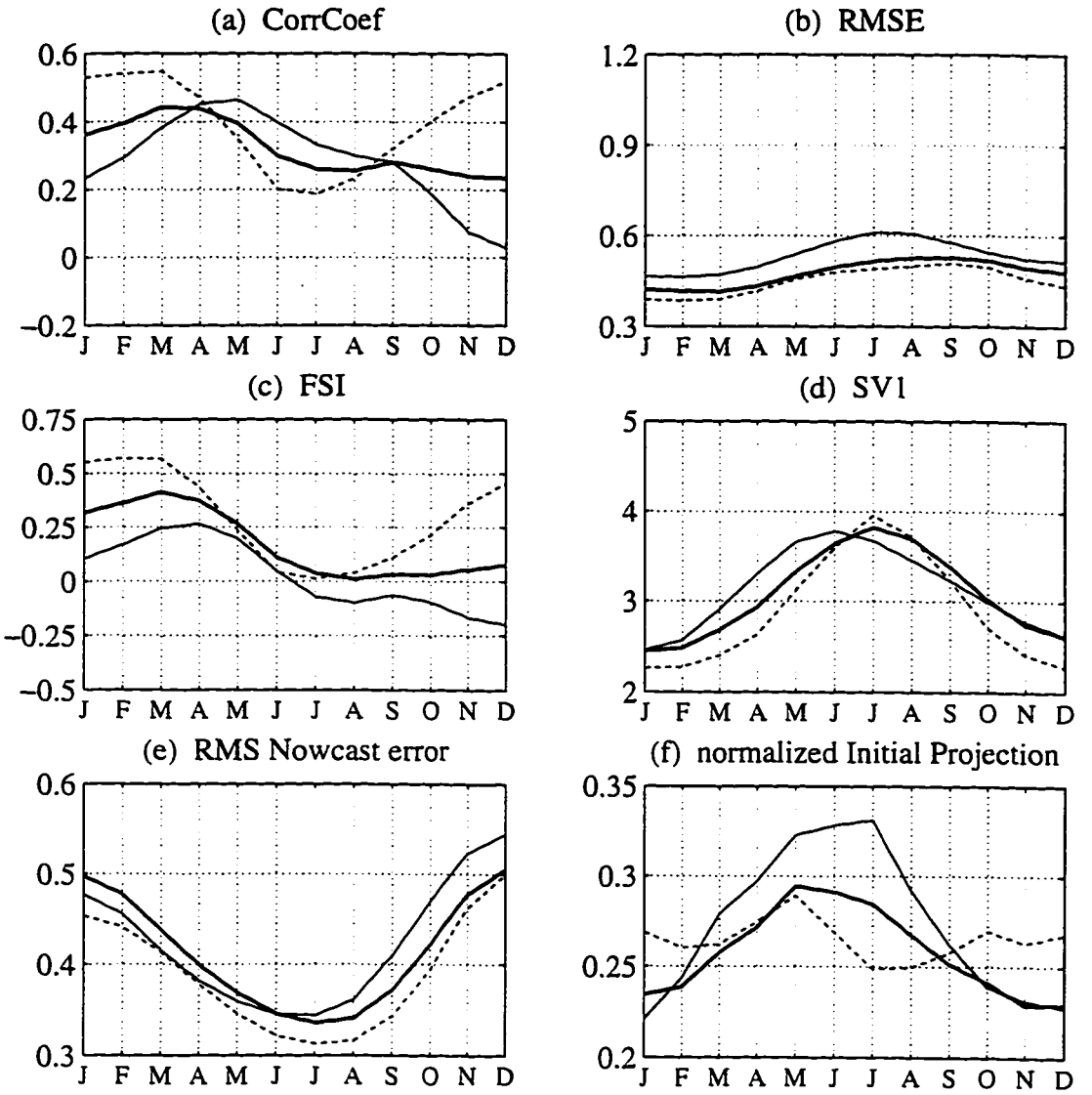

Figure 6.8 The annual–cycle composite: (a) the pattern correlation coefficient and (b) the rms error between the model forecast and the observed SST anomalies over the 11°S–11°N band along the equator; (c) is *FSI* and (d) is *SVI*; (e) is rms error in the nowcast over the 11°S–11°N domain and (f) is the projection of the nowcast error upon the optimal error in SST; the unit of projection is non-dimensional, i.e., the projection of the unit vector in the direction of the nowcast error upon a unit vector of the leading singular vector. The thin solid line indicates the composite over the period of 1967-75, the dashed line is for the period of 1977-87, and the thick solid line is for the period of 1967-90. The time axis indicates the 6–month forecast starting month. A three–month running-mean is applied to all curves.

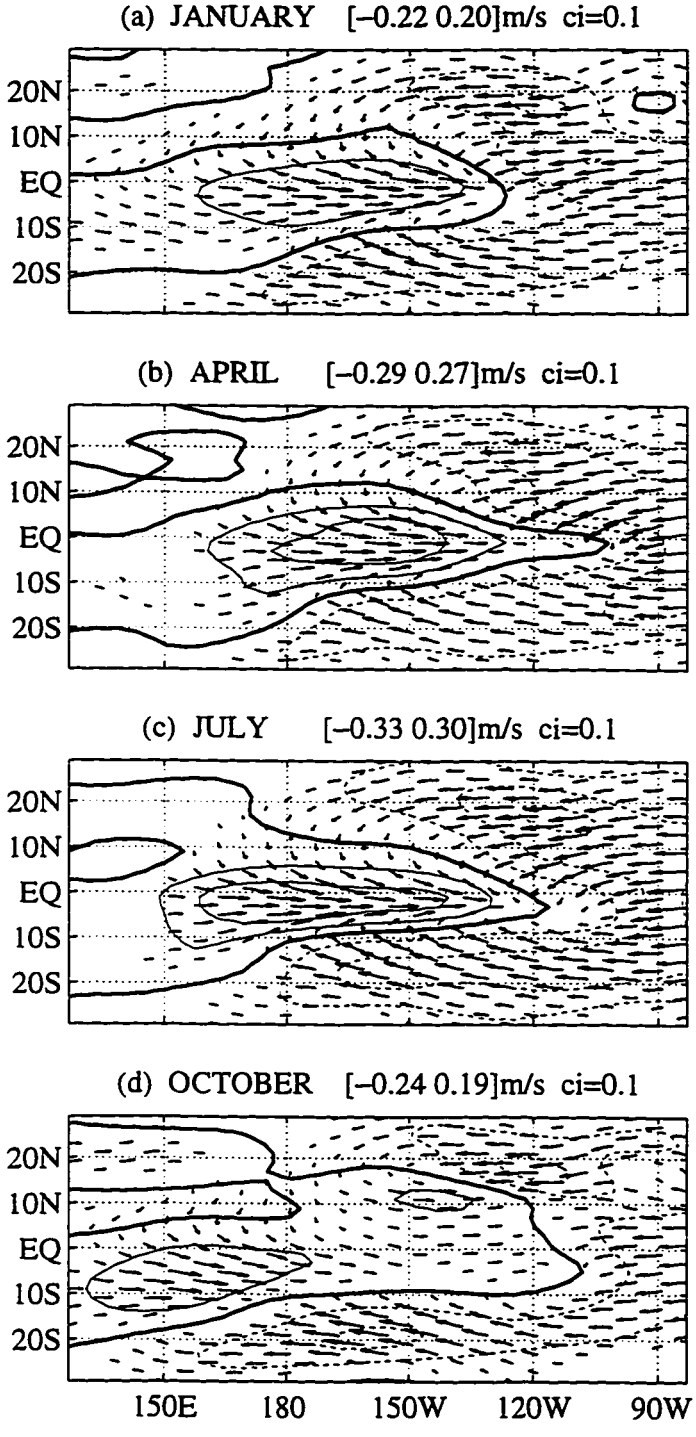

Figure 6.9 Difference between the cold and warm tropical climate states, i.e., *CLIM_II* (warm) minus *CLIM_I* (cold) (see section 6.3.1 for description): surface wind anomalies for January, April, July and October. The zonal component of the surface wind anomalies are contoured. Contour interval is 0.1 m/s.

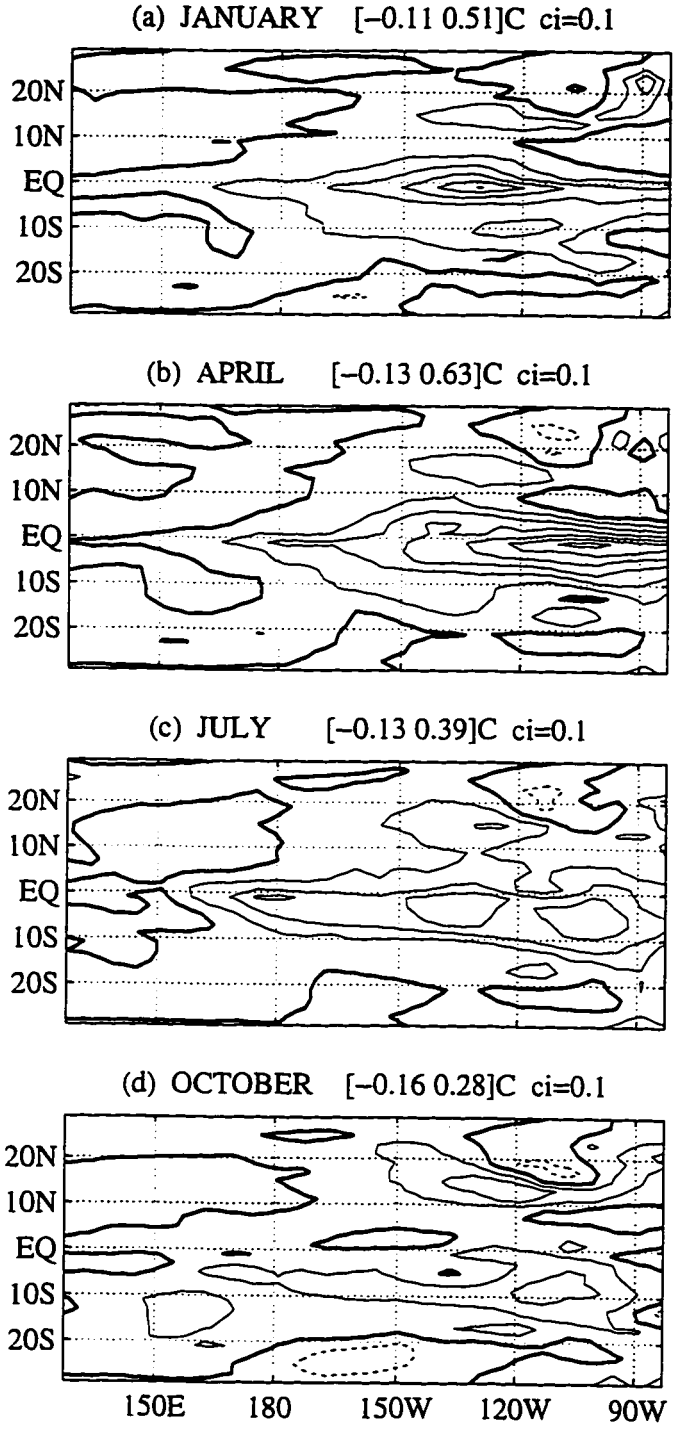

Figure 6.10 Same as in Fig. 6.9, but for SST anomalies. Contour interval is 0.1°C.

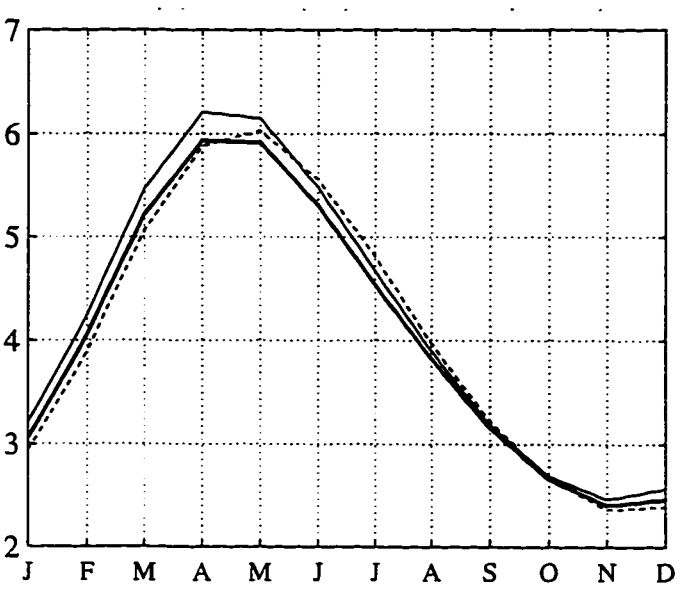

Figure 6.11 The optimal perturbation growth of SST as a function of the phase of the annual cycle for 6-month integrations about three different annual cycle climatological reference trajectories: the standard climatology (think solid curve), the standard climatology plus *CLIM_I* (thin solid curve), and the standard climatology plus *CLIM_II* (dashed curve).

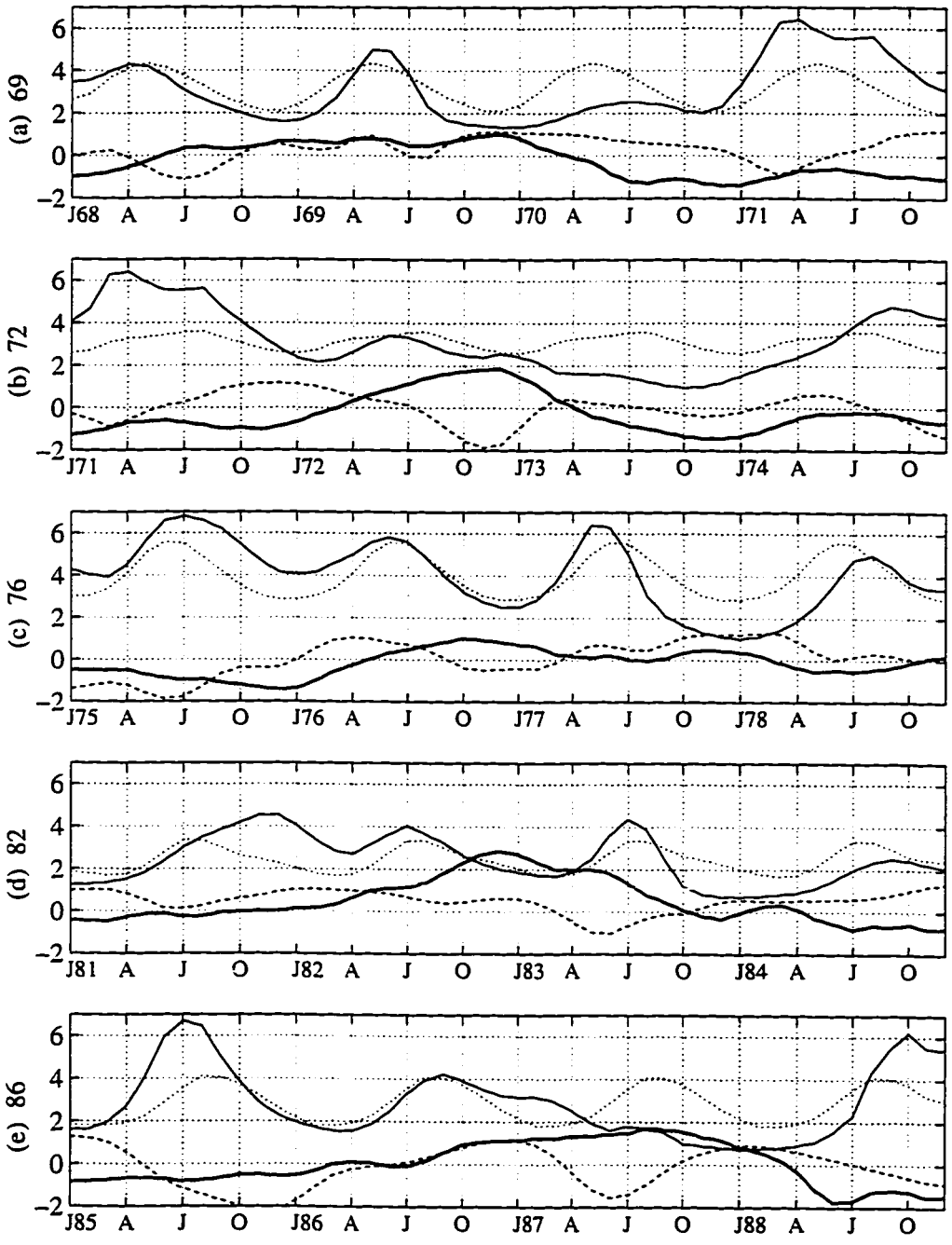

Figure 6.12 The *SVI* (thin solid), *FSI* (dashed), the observed NINO3 (in °C, the thick solid line), and the repeated annual–cycle *SVI* (dotted, see also Fig. 6.13) for the five individual El Niño events: (a) 69–70, (b) 72–73, (c) 76–77, (d) 82–83 and the (e) 86–87 episodes. A three–month running-mean is applied to all curves. See also Fig. 5.11 for comparison.

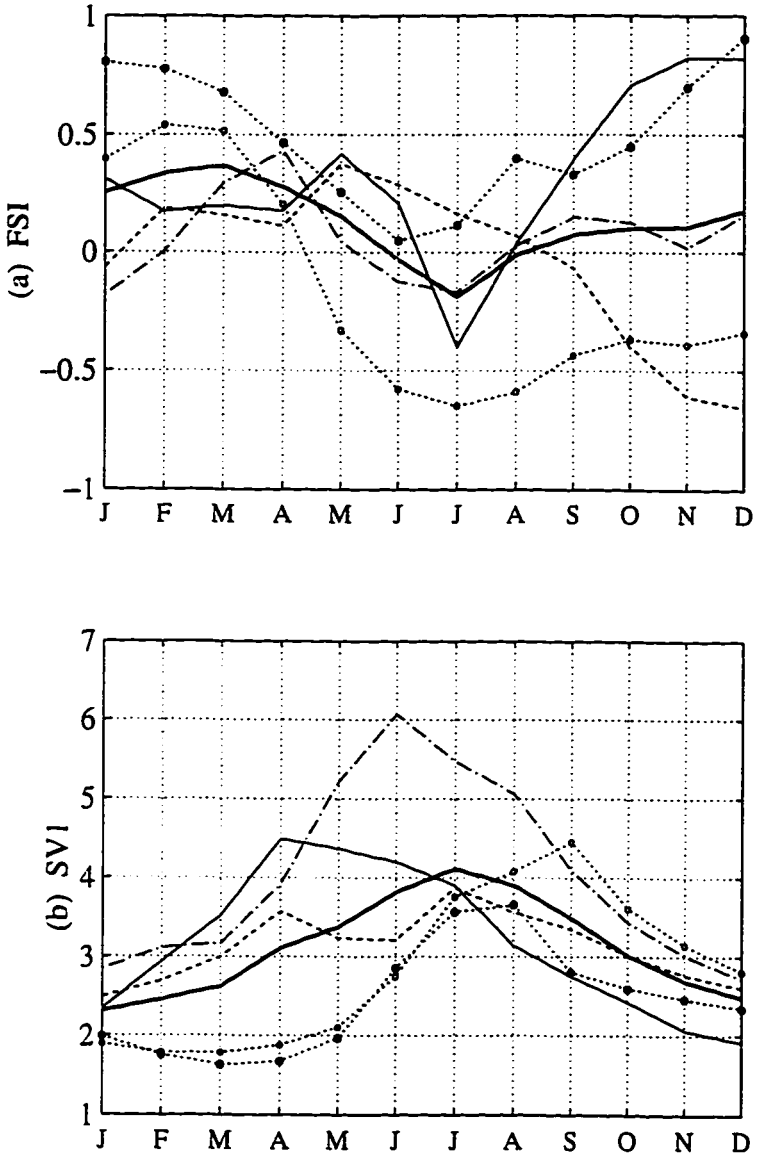

Figure 6.13 The annual cycle for (a) *FSI* and (b) *SVI*. Each curve is an annual cycle averaged over the four years of one of the five ENSO events: the 69–70 (thin solid line), 72–73 (dashed line), 76–77 (dash-dot line), 82–83 (solid circle) and the 86–87 (open circle) episodes. A three–month running-mean is applied to all curves.

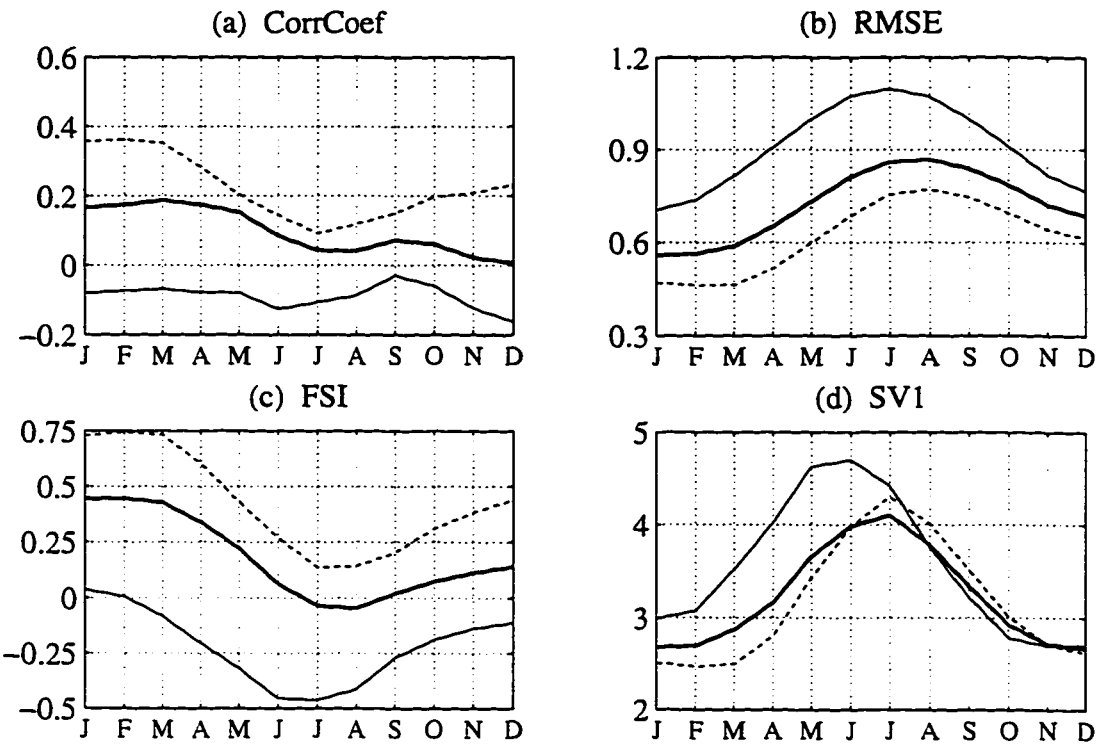

Figure 6.14 Same as in Fig. 6.8a-d, except for an experiment using the same model but with the *old* initialization scheme (Cane *et al.* 1986).

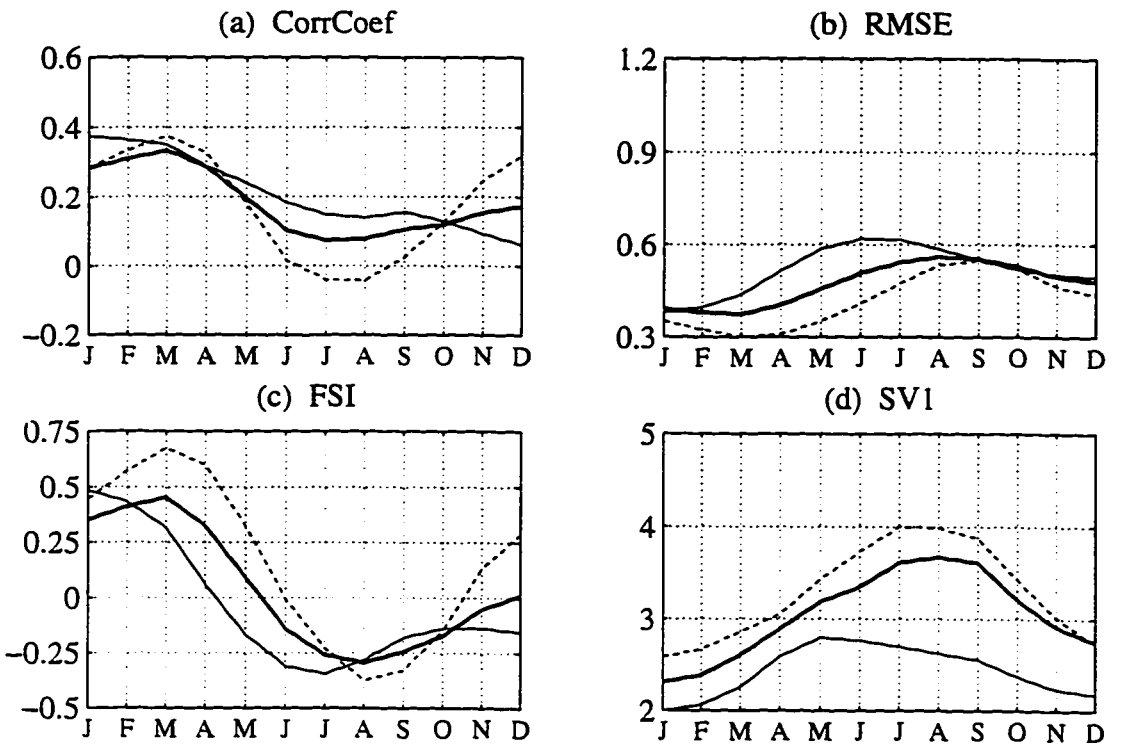

Figure 6.15 Same as in Fig. 6.8a-d, except for an experiment using the same model and with the same new initialization scheme, but using the *COADS* SST anomalies at the forecast starting time.

CHAPTER 7 DISCUSSION AND CONCLUSION

In this study, we examined the sensitivity of the Battisti (1988) coupled atmosphere-ocean model, considered as a forecast model for ENSO, to perturbations in SST applied at the beginning of a model integration. Since the climate system is non-normal, we use the singular vector analysis of an approximation to the propagator for the linearized system to determine the spatial structure and the growth of the fastest growing SST perturbation. In chapter 4, we consider perturbation growth, over periods of 3, 6 and 9 months, about four idealized reference trajectories: *(i)* the annual cycle climatology, *(ii)* a freely evolving model ENSO cycle with an annual cycle in the basic state, *(iii)* the annual mean basic state and *(iv)* a freely evolving model ENSO cycle with an annual mean basic state. In most cases investigated there is only one structure which exhibits growth.

The magnitude of the optimal perturbation growth (i.e., the leading singular value, *SVI*) is strongly dependent on both the phase of the seasonal cycle and the phase of the ENSO cycle at which the perturbation is applied and on the duration over which perturbations are allowed to evolve. However, the spatial structures of the optimal perturbation (i.e., the leading singular vector) at the initial and the final states are remarkably insensitive to these factors. The structure of the optimal perturbation consists of an east-west dipole spanning the entire tropical Pacific basin superimposed on a north-south dipole in the eastern tropical Pacific. A simple physical interpretation for the optimal pattern is provided in section 4.4.

Maximum optimal perturbation growth takes place for integrations which include the period June–August, and the minimum optimal growth occurs for integrations which include the period January–April. Maxima in the optimal growth also occur for forecasts

of ENSO onset and decay, while minima occur for forecasts initialized during the beginning of the peak phase of the warm event, after the transition from a warm to a cold event, and continuing through the cold event. The physical processes responsible for the large variation in the amplitude of the optimal perturbation growth are identified. Among the processes that determine the change in SST anomalies in this model, the thermocline displacement is shown to be the most important factor: excluding this process could not support any growing singular vectors for the three-month integrations. The most important horizontal advection term in the ocean for determining growth is the meridional advection by the mean flow, and the least important term is the zonal advection by the mean flow.

In chapter 5, we examined the error growth about the actual forecast trajectory extending from 1967-90. Model forecasts were carried out and analyzed for each month for the period from January 1967 to December 1990. We defined *FSI* as an index evaluating the skill of the model forecast; *FSI* takes into consideration the pattern correlation coefficient and the rms error between the model forecast and the observed SST anomalies over the domain of 11°S–11°N in the tropical Pacific.

For the Battisti model of ENSO, there is a strong inverse correlation between the optimal error growth about the actual forecast trajectories and the actual forecast skill of the model, suggesting that this optimal error growth is in practice an important indicator of forecast skill. For this 24–year period, we note that both the 6-month lead forecast skill and the 6-month optimal error growth are primarily dominated by the annual cycle: *FSI* for forecasts made in early Northern spring is high and *FSI* for forecasts made in Northern summer is low; *SVI* for integrations starting in late Northern winter or early Northern spring is small, and *SVI* for integrations starting late Northern spring or late Northern summer is large (see Fig. 5.10).

Three sets of calculations were performed in Chapter 6 to illustrate the role of the optimal error growth in SST in the forecast error for the six-month lead time. *First*, (regardless of the structure of the nowcast error,) in 68% of the cases investigated, the model forecast errors *can be* accounted for by the growth of errors in the SST anomalies at the initial conditions that are within the observational uncertainties, suggesting that a higher data accuracy of SST observations in the tropical Pacific region will help in the improvement of the model forecast. *Second*, (assuming the forecast error with a structure of the final state of the optimal error results exclusively from the optimal error of initial SST,) we demonstrated that up to 68% of the forecast error may be associated with the optimal transient growth of error in SST in the initial conditions, implying that a better initialization in SST can much improve the forecast. *Third*, (when we consider the structure of the nowcast error realized at the model forecast initialization time,) about 43% of the variance in the forecast error over the 1967-90 period *IS* from the realized error in the nowcast SST.

The seasonality of both the model forecast skill and the optimal error growth exhibit differences for the two periods: before and after 1976. Compared to the pre-1976 period, the 6-month optimal growth for errors about the forecast trajectory during the 1977-87 period is decreased except for integrations starting in June-August. This shift is shown to be related to the change in ENSO during the two epochs; it is not solely the result of the change in the mean climatological state for the two epochs. The forecast SST anomalies over the 11°S–11°N band along the equator are more skillful in the later period (1977–87) than the earlier period (1967–75). This increase in model forecast skill from the pre-1976 epoch to the post-1976 epoch is expected because of a combination of effects: a slight decrease in the mean value of the optimal error growth, a decrease in the nowcast error, and a decrease in the projection of the nowcast error upon the optimal leading singular vector.

In conclusion, we applied the singular vector analysis to investigate the predictability of ENSO using a simple coupled atmosphere-ocean model. The optimal error growth and the model ENSO forecast skill was shown to be intimately related on time scales from seasons to decades, implying that the optimal error growth, an index for the model sensitivity to small perturbations, is indeed a useful a priori indicator of the skill of the forecast.

LIST OF REFERENCES

Barnston, A.G., H.M. Van den Dool, S.E. Zebiak, T.P. Barnett, M. Ji, D.R. Rodenhuis, M.A. Cane, A. Leetmaa, N.E. Graham, C.F. Ropelewski, V. E. Kousky, E.A. O'Lenic, and R.E. Livezey, 1994: Long-lead seasonal forecasts - where do we stand?. *Bull. Amer. Met. Soc.*, **75**, 2097-2114.

Battisti, D.S., 1988: The dynamics and thermodynamics of a warming event in a coupled tropical atmosphere-ocean model. *J. Atmos. Sci.*, **45**, 2889-2919.

Battisti, D.S., and A.C. Hirst, 1989: Interannual variability in the tropical atmosphere-ocean system: influence of the basic state, ocean geometry and nonlinearity. *J. Atmos. Sci.*, **46**, 1687-1712.

Battisti, D.S., and E.S. Sarachik, 1995: Understanding and Predicting ENSO. IUGG Contributions in Oceanography. *Amer. Geophys. Union*, **33**, 1367-76.

Blumenthal, M.B., 1991: Predictability of a coupled atmosphere-ocean model. *J. Climate*, **4**, 766-784.

Branstator, G.W., 1985: Analysis of general circulation model sea-surface temperature anomaly simulations using a linear model. Part II: Eigenanalysis. *J. Atmos. Sci.*, **42**, 2242-2254.

Buizza, R., R. Gelaro F. Molteni, and T.N. Palmer, 1995: Predictability studies with high resolution singular vectors. *Quart. J. R. Meteor. Soc.*. To appear.

Buizza, R., and T.N. Palmer, 1995: The singular-vector structure of the atmospheric general circulation. *J. Atmos. Sci.*, **52**, 1434-1456.

Cane, M.A., S.E. Zebiak, and S.C. Dolan, 1986: Experimental forecasts of El Niño. *Nature*, **321**, 827-832.

Cane, M., and S.E. Zebiak, 1985: A theory for El Niño and the Southern Oscillation. *Science*, **228**, 1085-1087.

Cane, M., and S.E. Zebiak, 1987: Predictability of El Nino events using a physical model. In Atmospheric and Oceanic Variability, H. Cattle, ed., Royal Meteorological Society Press, 153-182.

_____, and R. J. Patton, 1984: A numerical model for low frequency equatorial dynamics. *J. Phys. Oceanogr.*, **14**, 1853-1863.

Chen, D., S. E. Zebiak, A. J. Busalacchi and M. A. Cane, 1995: An improved procedure for El Niño forecasting: implications for predictability. *Science*, **269**, 1699-1702.

Chen, Y.-Q., 1993: Optimal excitation of coupled atmosphere-ocean model SSTA. Proceedings from "Atmosphere-Ocean Dynamics and Interannual Climate Variability", a course held at Friday Harbor Laboratories at the University of Washington.

Chen, Ying-Quei, D.S. Battisti, and E.S. Sarachik, 1995: A New Ocean Model for Studying the Tropical Oceanic Aspects of ENSO. *J. Phys. Oceanogr.*, **25**, 2065-2089.

Chen, Ying-Quei, D.S. Battisti, T.N. Palmer, Joseph Barsugli, E.S. Sarachik, 1996: A Study of the Predictability of Tropical Pacific SST in a Coupled Atmosphere-Ocean Model Using Singular Vector Analysis: The Role of the Annual Cycle and the ENSO Cycle. *Mon. Weather Rev.*, to appear.

Clarke, A.J., 1982: Equatorial dynamics lecture notes. Unpublished.

Deser, Clara, and J.M. Wallace, 1990: Large-Scale Atmospheric Circulation Features of Warm and Cold Eposodes in the Tropical Pacific. *J. Climate*, **3**, 1254-1281.

Gill, A. E., 1980: Some simple solutions for heat-induced tropical circulation. *Quart. J. R. Met. Soc.*, **106**, 447-462.

Gill, A.E., and E.M. Rasmusson, 1984: The 1982-83 climate anomaly in the equatorial eastern Pacific. *Nature*, **306**, 229-234.

Farrell, B.F., 1989: Optimal excitation of baroclinic waves. *J. Atmos. Sci.*, **46**, 1193-1206.

Farrell, B.F., 1990: Small error dynamics and the predictability of atmospheric flows. *J. Atmos. Sci.*, **47**, 2409-2416.

Graham, N.E., J. Michaelsen, and T.P. Barnett, 1987: An investigation of the El Niño-Southern Oscillation cycle with statistical models. Part I. Predictor field characteristics. *J. Geophys. Res.*, **92**, 14251-14270.

Hirst, A.C., 1986: Unstable and damped equatorial modes in simple coupled ocean-atmosphere models. *J. atmos. Sci.*, **43**, 606-630.

Hirst, A.C., 1988: Slow instabilities in tropical ocean basin-global atmosphere models. *J. Atmos. Sci.*, **45**, 830-852.

Latif, M., T.P. Barnett, M.A. Cane, M. Flugel, N.E. Graham, H. von Storch, J.-S. Xu, and S.E. Zebiak, 1994: A review of ENSO prediction studies. *Climate Dynamics*, **9**, 167-179.

Levezey, R.E., and K.C. Mo, 1987: Tropical-extratropical teleconnections during the Northern Hemisphere winter. Part II. Relationships between monthly mean Northern Hemisphere circulation patterns and proxies for tropical convection. *Mon. Weather Rev.*, **115**, 3115-32.

Lorenz, 1965: A study of the predictability of a 28-variable atmospheric model. *Tellus*, **17**, 321-333.

Mantua, N.J. and D.S. Battisti, 1994: Evidence for the delayed oscillator mechanism for ENSO: The "observed" oceanic Kelvin mode in the far western Pacific. *J. Phys. Oceanogr.*, **24**, 691-699.

Mantua, N.J. and D.S. Battisti, 1995: Aperiodic variability in the Zebiak-Cane coupled ocean-atmosphere model: ocean- atmosphere interactions in the western equatorial Pacific. *J. Climate*, **8**, 2897-2927.

Molteni, F., R. Buizza, T.N. Palmer and T. Petroliagis, 1995: The ECMWF ensemble prediction system: methodology and validation. *Quart. J. Roy. Meteor. Soc.*. **122**. To appear.

Moore, A.M. and R. Kleeman, 1996: The dynamics of error growth and predictability in a coupled model of ENSO. *Quart. J. R. Meteor. Soc.*, **122**, 1405-1446.

Moura, A.D, 1994: Prospects for seasonal-to-interannual climate prediction and applications for sustainable development. *World Meteorological Society Bulletin*, **43**, 207-215.

Palmer, T.N.,R. Buizza, F. Molteni, Ying-Quei Chen, and S. Corti, 1994: Singular vectors and the predictability of weather and climate. *Phil. Trans. R. Soc. Lond.*, **348**, 459-475.

Penland, C. and P.D. Sardeshmukh, 1995: The optimal growth of tropical sea surface temperature anomalies. *J. Climate*, **8**, 1999-2024.

Philander, S.G.H., and R.C. Pacanowski, 1981: The ocean response to cross-equatorial winds (with application to coastal upwelling in low latitudes). *Tellus*, **33**, 201-210.

Rasmusson, E.M., and T.H. Carpenter, 1982: Variations in tropical sea surface temperature and surface wind fields associated with the Southern Oscillation/El Niño. *Mon. Weather Rev.*, **110**, 354-384.

Reynolds, R.W., and T.M. Smith, 1993: Improved global sea surface temperature analysis using optimum interpolation. National Meteorological Center, U.S. Department of Commerce, 59pp. Submitted to *J. Climate*.

Rosati, A., K. Miyakoda, and R. Gudgel, 1995: The impact of ocean initial conditions on ENSO forecasting with a coupled model, in press, *Mon. Weather Rev.*

Ropelewski, C.F. and M.S. Halpert, 1987: Global and regional scale precipitation patterns associated with El Niño/Southern Oscillation. *Mon. Wea. Rev.*, **115**, 1606-1626.

Schopf, P. S., and M. A. Cane, 1983: On equatorial dynamics, mixed layer physics and sea surface temperature. *J. Phys. Oceanogr.*, **13**, 917-935.

Seager, R., S. E. Zebiak, and M. A. Cane, 1988: A model of the tropical Pacific sea surface temperature climatology. *J. Geophys. Res.*, **93**, 1265-1280.

Strang, G., 1988: *Linear algebra and its applications.* 3rd Ed. Academic Press, 442-452.

Trenberth, K.E., 1991: General Characteristics of El Niño - Southern Oscillation. In Teleconnections linking worldwide climate anomalies. Ed. M.H. Glantz, R.W. Katz and N. Nicholls. Cambridge University Press, Cambridge. pp 13-42.

Xue, Y., M.A. Cane, S.E. Zebiak and M.B. Blumenthal, 1994: On the prediction of ENSO: A study with a low-order Markov model. *Tellus*, **46**, 512-528.

Xue, Y., M.A. Cane, S.E. Zebiak, 1997: Predictability of a coupled model of ENSO using singular vector analysis. Part I and Part II. Submitted to MWR.

Zebiak, S.E., 1986: Atmospheric convergence feedback in a simple model for El Niño. *J. Atmos. Sci.*, **114**, 1263-1271.

Zebiak, S.E. and M.A. Cane, 1987: A model El Niño/Southern Oscillation. *Mon. Weather Rev.*, **115**, 2262-2278.

Zhang, Yuan, J.M. Wallace, and D.S. Battiti, 1996: ENSO-like decade-to-century scale variability: 1900-93, submitted to *J. Climate.*

APPENDIX A PARAMETERIZATION OF THE SUBSURFACE TEMPERATURE ANOMALY

Perturbations of the model thermocline depth h about the mean state $\bar{h}(x, y)$ give rise to subsurface (at the bottom of the surface mixed layer) temperature anomalies (T_s). In the presence of upwelling (w), these anomalies will cause a change in sea surface temperature anomalies (T) through:

$$w \cdot \frac{(T - T_s)}{H_1}, \qquad \text{(EQ A.1)}$$

where H_1 is the depth of the mixed layer.

The parameterization of the subsurface temperature anomaly in the B88 model is a modified version of that used by ZC:

$$T_s = \Theta(h) \cdot [\tanh(\lambda(\bar{h} + 1.5|h|)) - \tanh(\lambda h)], \qquad \text{(EQ A.2)}$$

where Θ and λ are constants, whose values depend only on the sign of the thermocline depth perturbation h (See B88, Appendix A). The parameterization (Eq. A.2) is developed in ZC and is based on an empirical fit of the temperature at the base of the mixed layer (H_1 is taken to be 50 m) and the position of the thermocline (see also Seager *et al.* 1988).

The greatest sensitivity in the heating tendency (Eq. A.1) will result where thermocline perturbations (h) yield greatest perturbations to T_s in Eq. A.2, which is where the thermocline is at its climatological annual mean position ($h = 0$).

In the equatorial Pacific, observations indicate that there is a lower limit to the subsurface temperature: it rarely drops below 15°C. A physical justification for the parameterization (A2) of the temperature of the water that is being entrained into the mixed layer is as follows. When the thermocline is very close to the sea surface, the stratification at

the base of the mixed layer is large. Hence, the subsurface temperature T_s becomes non-linearly saturated as it becomes more difficult to change the temperature of the water that is entrained into the mixed layer.

APPENDIX B A LINEARITY-CHECK FOR CHAPTER 5

To examine the linearity, we choose one example in each group defined in section 5.5. We apply the optimal error of unit norm, i.e., the leading singular vector, as an initial perturbation in the coupled model, and monitor the evolution of the model response. A control integration (without the initial perturbation) is also carried out. Figs. B.1–B.4 display the differences in the SST anomalies between the perturbed integration and the control integration, for integrations starting November 1981 (Day 7515; a member of Group I), April 1975 (Day 5145; a member of Group II), October 1977 (Day 6045; a member of Group III), and May 1987 (Day 9495; a member of Group IV), respectively. Comparing the six–month response (h) with the final pattern of the optimal error (b) suggests that linearity holds reasonably well most of the time: the SST pattern correlation coefficients between panels (b) and (h) averaged over the four cases is as high as 0.995; the average error in the growth is only 7% of the growth estimated by the singular vector analysis. As a reference, Fig. B.5 and Fig. B.6 plot the difference in thermocline anomalies and the wind stress anomalies between the perturbed and the control integrations. It is shown that all fields with an initial optimal perturbation in SST develop into ENSO–like perturbation patterns. Thus, bases on these cases, we do not believe that the breakdown in the inverse relationship between *FSI* and *SVI* is due to contributions to maximum error growth due to nonlinear processes.

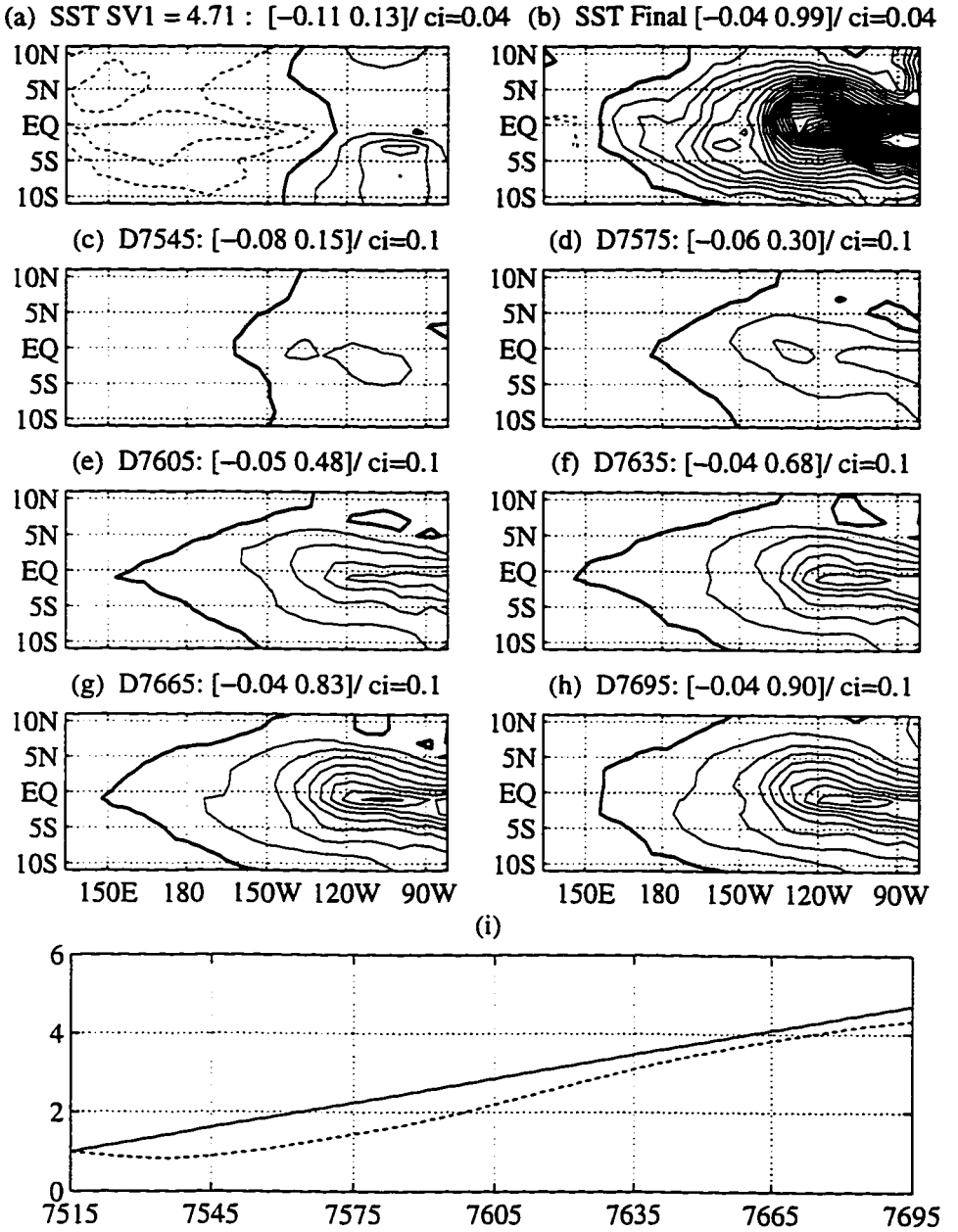

Figure B.1 A perturbed integration starting November 1981 (Day 7515; a member of Group I) with an initial perturbation of the leading singular vector (of unit norm). (a) and (b) are the initial and the final pattern of the leading singular vector for a six–month integration starting November 1981. (c-h) are the differences of the SST anomalies between the perturbed and the control integration after one month to six months of integration time, taken one month apart. The range and the contour interval are printed. The norm for the difference of the SST anomalies between the perturbed and the control integrations are displayed in (i). Unit in the time axis is in days.

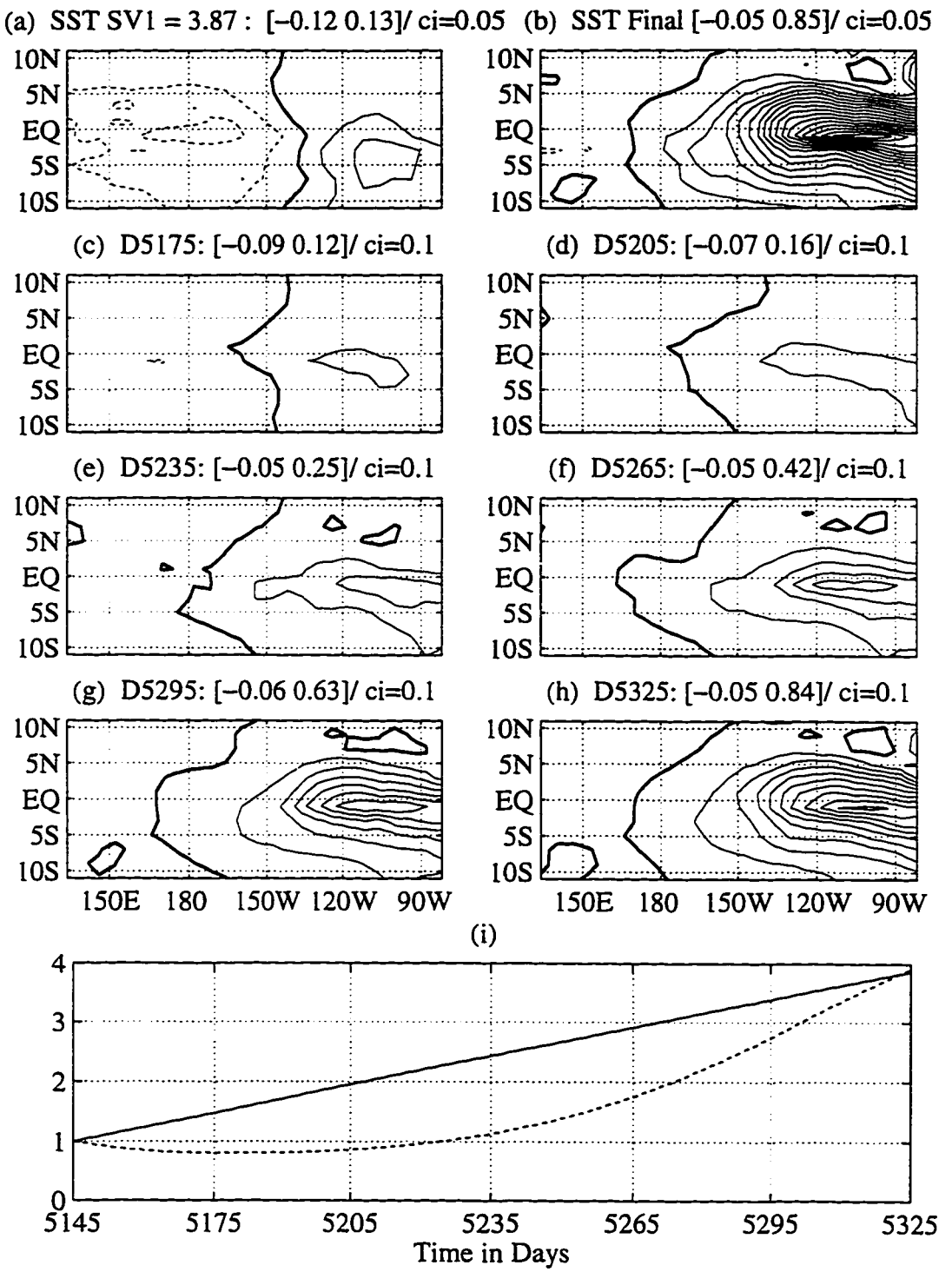

Figure B.2 Same as in B.1 but for integration starting April 1975 start (Day 5145): a member of Group II.

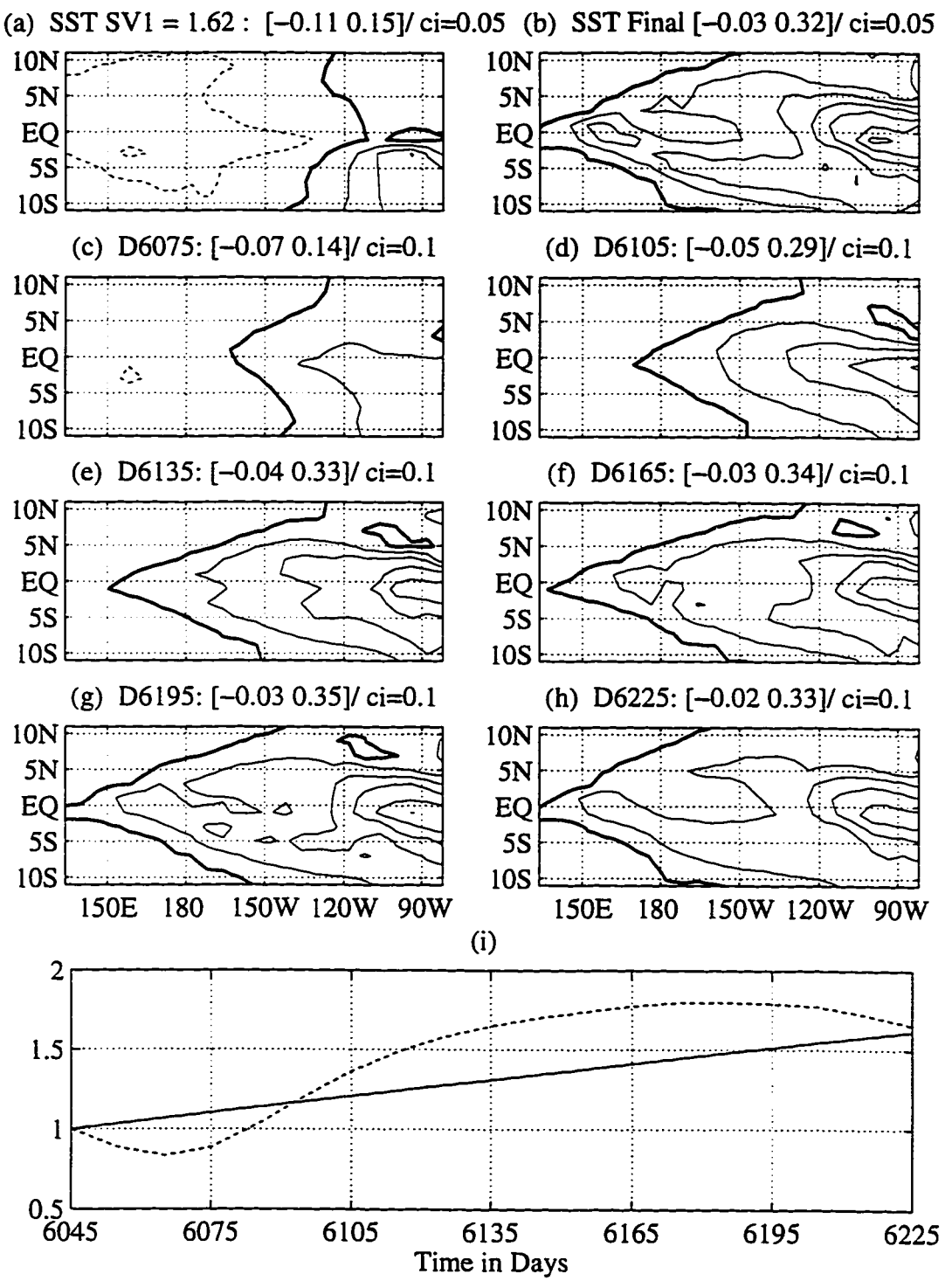

Figure B.3 Same as in B.1 but for integration starting October 1977 (Day 6045): a member of Group III.

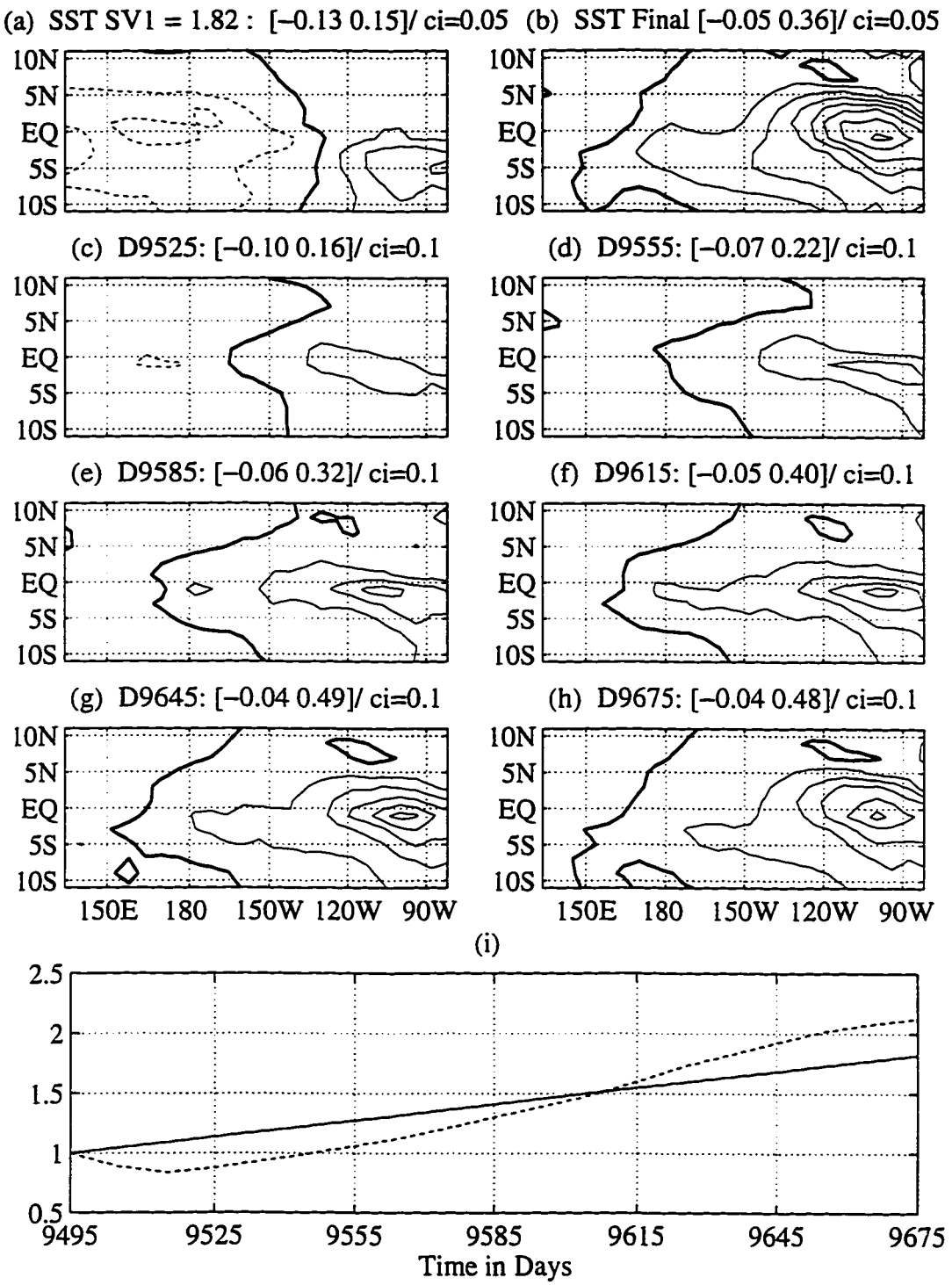

Figure B.4 Same as in B.1 but for integration starting May 1987 (Day 9495): a member of Group IV.

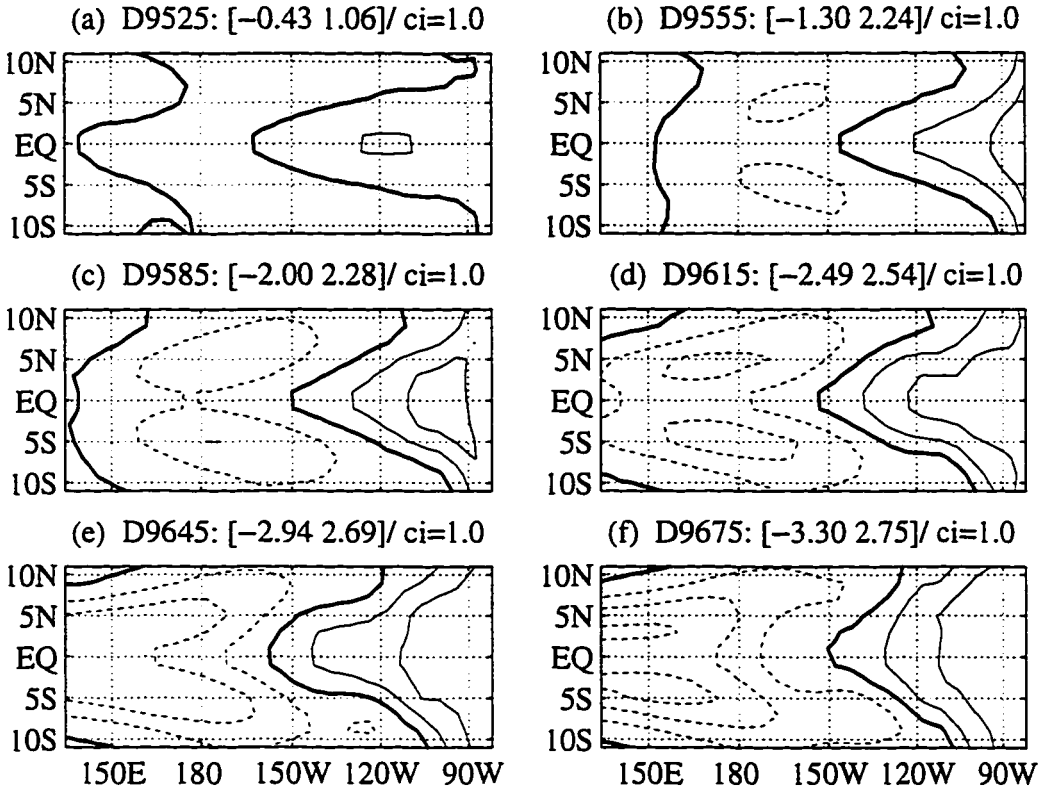

Figure B.5 Same as in B.4 but for thermocline depth anomalies (m). The 1-month through 6-month evolution are displayed in (a-f).

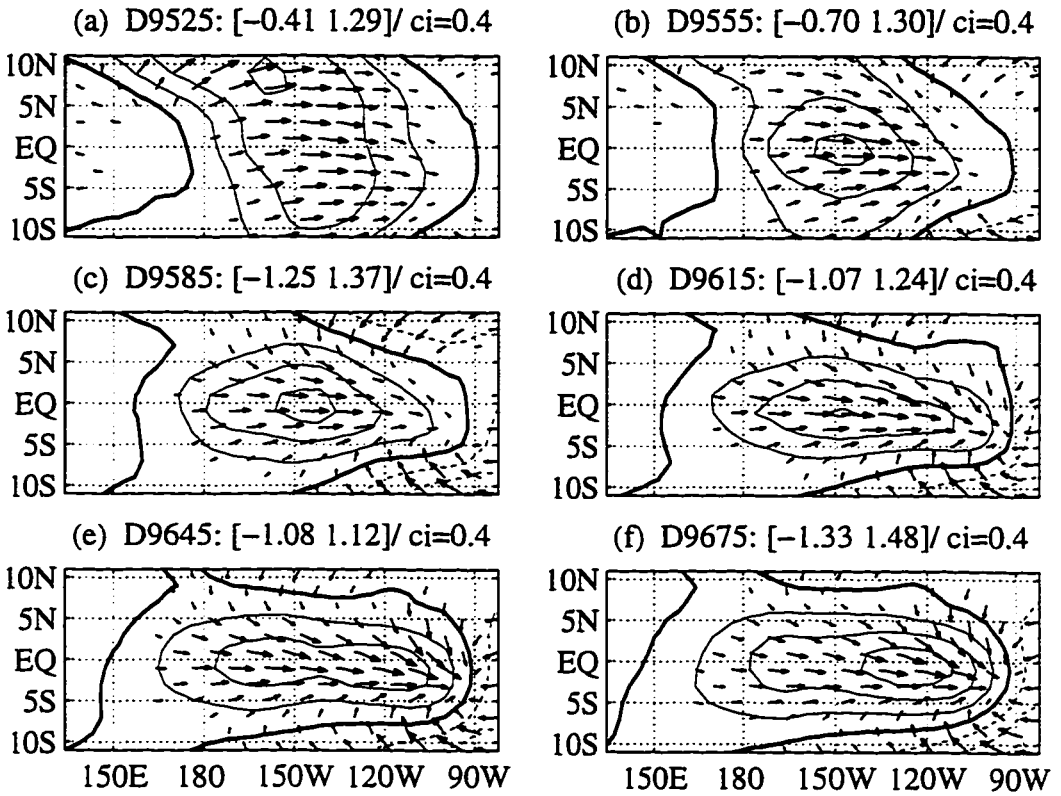

Figure B.6 Same as in B.4 but for wind stress anomalies ($m^2\ s^{-2}$). The 1-month through 6-month evolution are displayed in (a-f).

VITA

Ying-Quei Chen was born on 18 November 1967 in Yuanlin, Taiwan. She attended the National Taiwan University in 1985 and graduated first in class with a B.S. in Atmospheric Sciences in 1989. Since the third year as an undergraduate, she has been involved with some research projects as a part-time student research assistant working with professor C.S. Lee, on 'Striking Probability of Typhoons' and 'Q1/Q2 Analysis During TAMEX'. After she graduated, she was a teaching assistant at the Department of Atmospheric Sciences, National Taiwan University for one year. In 1990, she entered the graduate program at the Department of Atmospheric Sciences, University of Washington, working with professors E.S. Sarachik and D.S. Battisti. Her research during the graduate study mainly focus on coupled modeling on tropical Pacific sea surface temperature and ENSO predictability and optimal error growth in the short-term climate system. After accomplishing her Ph.D. in the fall of 1996, she will devote herself in studying Buddhism with Rev. Miou-King at the Fa-Yun Monastery Buddhist Institution.

Publications:

Chen, Ying-Quei, 1993: A modeling study of the tropical oceanic aspects of ENSO. Master Thesis, University of Washington, 168pp.

Chen, Ying-Quei, 1993: Optimal excitation of coupled atmosphere-ocean model SSTA. Proceedings from "Atmosphere-Ocean Dynamics and Interannual Climate Variability", a course held at Friday Harbor Laboratories at the University of Washington.

Palmer, T.N.,R. Buizza, F. Molteni, Ying-Quei Chen, and S. Corti, 1994: Singular vectors and the predictability of weather and climate. *Phil. Trans. R. Soc. Lond.*, **348**, 459-475. (Also appears in Chapter 12 of *Chaos and Forecastings*, Would Scientific Publishing Co. Pte Ltd.)

Chen, Ying-Quei, D.S. Battisti, and E.S. Sarachik, 1995: A New Ocean Model for Studying the Tropical Oceanic Aspects of ENSO. *J. Phys. Oceanogr.*, **25**, 2065-2089.

Chen, Ying-Quei, D.S. Battisti, T.N. Palmer, Joseph Barsugli, E.S. Sarachik, 1995: Examination of the relationship between the forecast skill of tropical Pacific SST and optimal perturbation growth for the period of 1961-90. Abstract. *1995 AGU Fall Meeting*, **76**, F323.

Chen, Ying-Quei, D.S. Battisti, T.N. Palmer, Joseph Barsugli, E.S. Sarachik, 1996: A study of the predictability of tropical Pacific SST in a coupled atmosphere-Ocean model using singular vector analysis: the role of the annual cycle and the ENSO cycle. *Mon. Weather Rev.*, to appear.

David S. Battisti, Joseph J. Barsugli and Ying-Quei Chen, 1997: Decadal variability in singular values and forecast error in a model of ENSO. AMS 7th Conference on Climate Variations. Abstract accepted.